Normal Radiological Anatomy and Anatomical Variants of the Kidney

Emilio Quaia, Paola Martingano, Marco Cavallaro, Michael Premm, and Roberta Angileri

Contents

1	**Anatomy and Physiology of the Kidney**	17
1.1	Normal Renal Anatomy	17
1.2	Normal Renal Physiology	23
1.3	Calculation of Glomerular Filtration Rate (GFR)	25
1.4	Calculation of Glomerular Filtration Rate (GFR) in Acute Renal Failure	27
2	**Normal Radiological Anatomy of the Renal Parenchyma, Intrarenal Vasculature, and Anatomical Variants**	28
2.1	Conventional Radiography	28
2.2	Grayscale and Doppler Ultrasound	28
2.3	Computed Tomography	30
2.4	Magnetic Resonance Imaging	31
2.5	Anatomical Variants of Renal Morphology	34
2.6	Congenital Anomalies of the Renal Parenchyma	36
3	**Normal Radiological Anatomy of Renal Vessels and Anatomical Variants**	43
3.1	Grayscale and Doppler Ultrasound	44
3.2	CT Angiography	45
3.3	MR Angiography	46
3.4	Anatomical Variants of Renal Vessels	47
4	**Normal Radiological Anatomy of the Urinary Tract and Anatomical Variants**	52
4.1	Excretory Urography and Anterograde and Retrograde Pyelography	52
4.2	CT Urography	53
4.3	Magnetic Resonance Imaging and MR Urography	53
4.4	Anatomical Variants of the Urinary Tract	57
5	**Appendix: Basic Morphological Changes of the Intrarenal Urinary Tract Visible on Intravenous Excretory Urography and Multidetector CT Urography**	60
	References	73

E. Quaia (✉) • P. Martingano • M. Cavallaro • R. Angileri
Department of Radiology, Cattinara Hospital, University of Trieste, Strada di Fiume 447, Trieste, 34149, Italy
e-mail: quaia@units.it

M. Premm
Erasmus Program, Medical University of Graz, Auenbruggerplatz 2, A-8036 Graz, Austria

Abstract

The kidneys are highly vascularized organs. Each kidney receives the highest blood flow per gram of organ weight in the body (1.2 L/min corresponding to 20 % of the cardiac output and a perfusion value of 400 mL/min/100 g). The most employed indicator of the renal function is the glomerular filtration rate (GFR), which can be estimated according to different formulas. The calculation of the GFR is essential for a correct employment of iodinated and gadolinium-based contrast agents. The most widely used equations for estimating GFR are the Cockcroft–Gault and the Modification of Diet in Renal Disease Study Group (MDRD) formulas.

The modern radiological imaging techniques allow a detailed depiction of the renal anatomy and of the anatomical variants. Ultrasound, computed tomography, and magnetic resonance imaging define accurately the anatomy and anatomical variants of the renal parenchyma, arteries, and intrarenal urinary tract.

1 Anatomy and Physiology of the Kidney

1.1 Normal Renal Anatomy

1.1.1 Macroscopic Renal Anatomy

The kidneys are retroperitoneal organs that are located in the perirenal space (with adrenals) and present a longitudinal diameter of 9–12 cm and a latero-lateral diameter of 3–5 cm and a weight of 250–270 g. The kidney initially develops opposite to the future S2 vertebra, but eventually comes to rest opposite the L1 or L2 vertebra (Federle 2006). In the supine position, the medial border of the normal kidney is much more anterior than the lateral border, so that the kidneys lie at an angle of about 30° from the horizontal (Nino-Murcia et al. 2000). The upper pole of each kidney is situated more posteriorly than the lower pole.

E. Quaia (ed.), *Radiological Imaging of the Kidney*, Med Radiol Diagn Imaging,
DOI 10.1007/978-3-642-54047-9_2, © Springer-Verlag Berlin Heidelberg 2014

The right kidney, anteriorly, has a relation with the inferior surface of the liver with peritoneal interposition and with the second portion of the duodenum without any peritoneal interposition since the second portion of the duodenum is retroperitoneal (Fig. 1a). The left kidney, anteriorly, has a relation with the pancreatic tail, the spleen, the stomach, the ligament of Treitz and small bowel, and the left colic flexure and left colon (Fig. 1a). Over the left kidney, there are two important peritoneal reflections, one vertical corresponding to the splenorenal ligament (connected to the gastrodiaphragmatic and gastrosplenic ligaments) and one horizontal corresponding to the transverse mesocolon. Posteriorly, both kidneys present a relationship with the diaphragm, with the lateral margin of the psoas muscle, with the aponeurosis of the transverse abdominis muscle, and with the lumbar muscle (Fig. 1b). Superiorly, both kidneys have a relation with the adrenal glands, while the right kidney is separated from the inferior surface of the liver by the interposition of a double peritoneal sheet which derives from the reflection of the peritoneum to the inferior limit of the coronary liver ligament that delimitates the hepatorenal space or Morrison pouch.

The renal parenchyma is composed of different components (Fig. 1c). The *renal capsule* is a tough fibrous layer surrounding the kidney (fibrous renal capsule) and covered by a thick layer of perinephric adipose tissue (fat renal capsule). The kidney is covered by the renal capsule formed by the fibrous and adipose renal capsule. The fibrous capsule

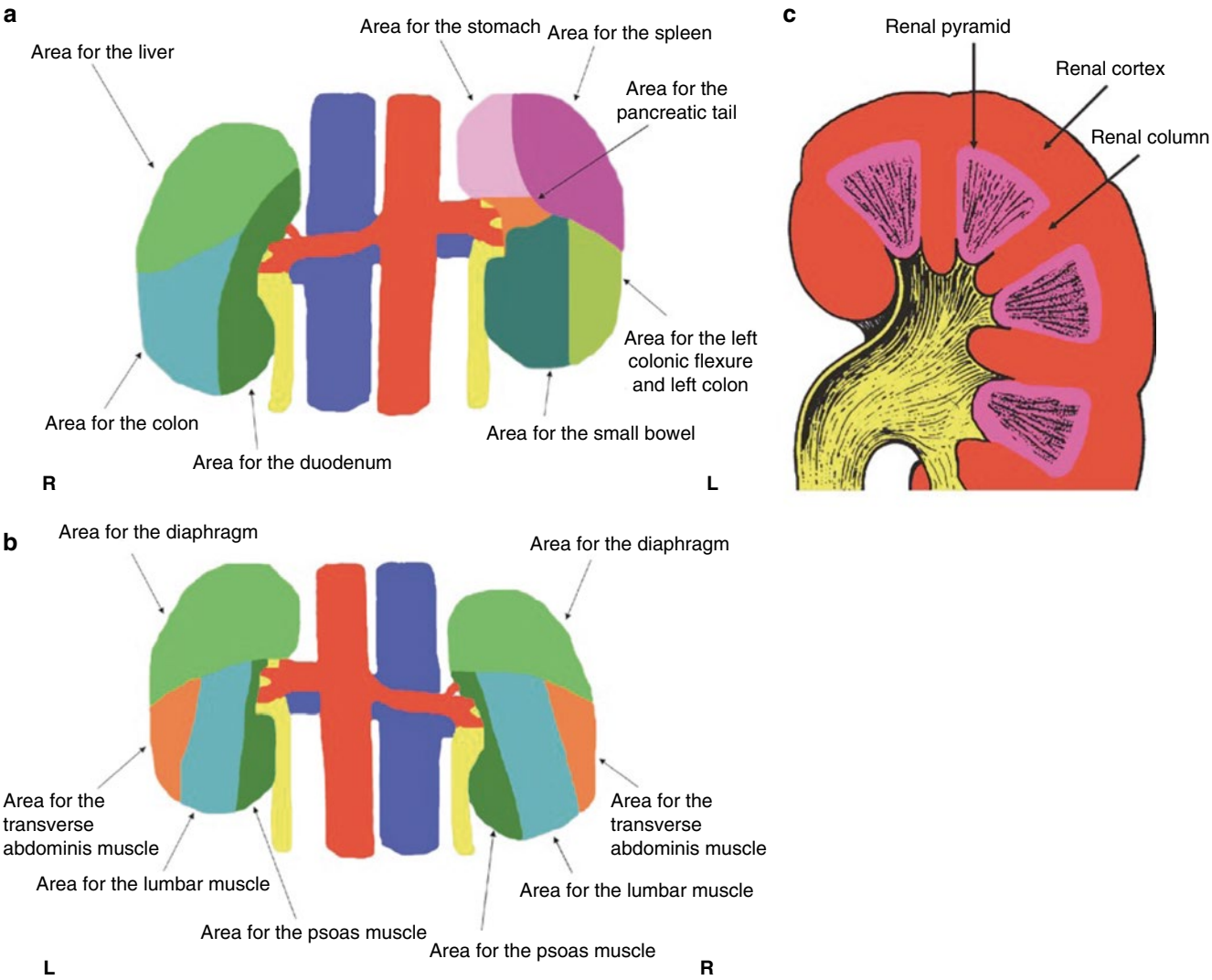

Fig. 1 (**a**) Scheme of the anterior anatomical relations of the kidneys: *R* right, *L* left. (**b**) Scheme of the posterior anatomical relations of the kidneys: *R* right, *L* left. (**c**) Scheme of the main components of the renal parenchyma (renal cortex, renal columns, and renal medulla divided in multiple renal pyramids) overlied by the renal capsule (*black color*)

represents the connective tissue investment of the kidney, continuous through the hilum to line the renal sinus. The adipose renal capsule represents the investment of fat surrounding the fibrous capsule of the kidney, continuous at the hilum with the fat in the renal sinus. The *renal cortex* is the outer portion of the kidney between the fibrous renal capsule and the renal medulla. In the adult, it forms a continuous smooth outer zone with a number of projections (cortical columns) that extend down between the pyramids. The renal cortex is the part of the kidney where ultrafiltration occurs. It contains the renal corpuscles and the renal tubules except for parts of the loop of Henle, which descend into the renal medulla. It also contains blood vessels and cortical collecting ducts. The renal column (or Bertin column or column of Bertin) is an extension of the renal cortex between the renal pyramids, and it allows the cortex to be better anchored. Each column consists of lines of blood vessels and urinary tubes and a fibrous material.

The *renal medulla* is the innermost part of the kidney. The renal medulla is split up into a number of sections, known as the *renal pyramids* (Fig. 1c) about 8–18 in number. The broad *base* of each pyramid faces the renal cortex (outer medulla), and its apex, or papilla (inner medulla), points internally. The pyramids appear striped because they are formed by straight parallel segments of nephrons. Renal pyramids (or malpighian pyramids) are cone-shaped tissues of the kidney, and the *renal papilla* is the location where the medullary pyramids empty urine into the renal pelvis. Histologically, it is marked by medullary collecting ducts converging to channel the fluid.

Segmentation and duplications of the renal pelvis and/or ureters are secondary to segmentation of the wolffian duct, which forms the collecting system. The renal pelvis is generally triangular, and it tapers smoothly to its junction with the ureter defined as ureteropelvic junction. The pelvis exits from the kidney anteromedially. The right renal pelvis is usually located opposite to the L2 vertebra, and the left renal pelvis is usually 0.5–1 cm higher (Friedenberg and Dunbar 1990). The *renal calyx* is a concave structure receiving the tip of the papilla of the renal medulla, and the fornices represent the side projections of the calyx surrounding the papilla. Two wide cup-shaped major renal calices are subdivided into 7–14 minor calices. Each single calyx or multiple minor calyces drain by means of an infundibulum into the renal pelvis. The renal sinus is the compartment that surrounds the pelvocalyceal system of the kidney, is filled by peripelvic fat, and communicates medially with the perinephric space. It contains the vascular and nervous structures that enter within the renal sinus, the lymphatics, the renal pelvis, and the surrounding fat. Cysts and sinus lipomatosis are the most common abnormalities in this space. The ureter also presents a restriction where it crosses the iliac vessels and enters the anatomical pelvis at the ureterovesical junction.

In each kidney, the *main renal artery* divides into the posterior and anterior branches that run posteriorly and anteriorly to the renal pelvis (Fig. 2). The superior, anterior superior, anterior inferior, and inferior vascular areas of each kindey are vascularized by the segmental arteries originating from the larger anterior branch. The posterior vascular area is vascularized by the smaller posterior branch of the main renal artery (Fig. 2a). The junction of the anterior and posterior branches of the main renal artery in the renal parenchyma creates a relatively avascular plane (Brodel's line), which is the preferred track of placing percutaneous nephrostomies and should be considered when performing biopsies of a native or transplanted kidney.

The superior, anterior superior, anterior inferior, inferior and posterior vascular areas of the kidney are vascularized by the segmental arteries of the same name (Fig. 2a), which subdivide into interlobar arteries (Fig. 2b). Each interlobar artery penetrates the kidney through a column of Bertin and divides at the corticomedullary junction into arcuate arteries, which eventually run parallel to the surface (Fig. 2b). The arcuate arteries, in turn, supply interlobular arteries that penetrate the cortex perpendicularly to the renal surface (Fig. 2c). Branching from each interlobular artery are numerous small arterioles, the afferent arteries. The fibers of the nervous renal plexus, including sympathetic nervous fibers triggering vasoconstriction, course along the renal artery to reach each kidney. The renal branches of the vagus nerve are small branches providing parasympathetic innervation to the kidney. Sensory input from the kidney travels to T10–11 levels of the spinal cord.

The renal lymphatics have not been fully documented in humans (Ischikawa et al. 2006). The distribution of the normal renal lymphatic system has been investigated in various animals using light microscopy by the ureteric occlusion technique, electron microscopy, and microradiography (Hogg et al. 1982). In humans, microradiography has been performed to detect the renal lymphatics at autopsy (Cuttino et al. 1989). Lymphatic vessels are abundant around the intrarenal arteries/veins, while they are scarce in the interstitium around the glomeruli or between the tubules (Ischikawa et al. 2006), since the lymphatic system begins in the cortical interstitium around the glomeruli or between the tubules. Lymph nodes for the kidneys include the renal hilar nodes and the abdominal para-aortic (periaortic) nodes including the interaortocaval, paracaval, precaval, retrocaval, preaortic, and retroaortic lymph nodes. The ureters are drained prevalently by the renal hilar and paracaval lymph node groups (Fig. 3).

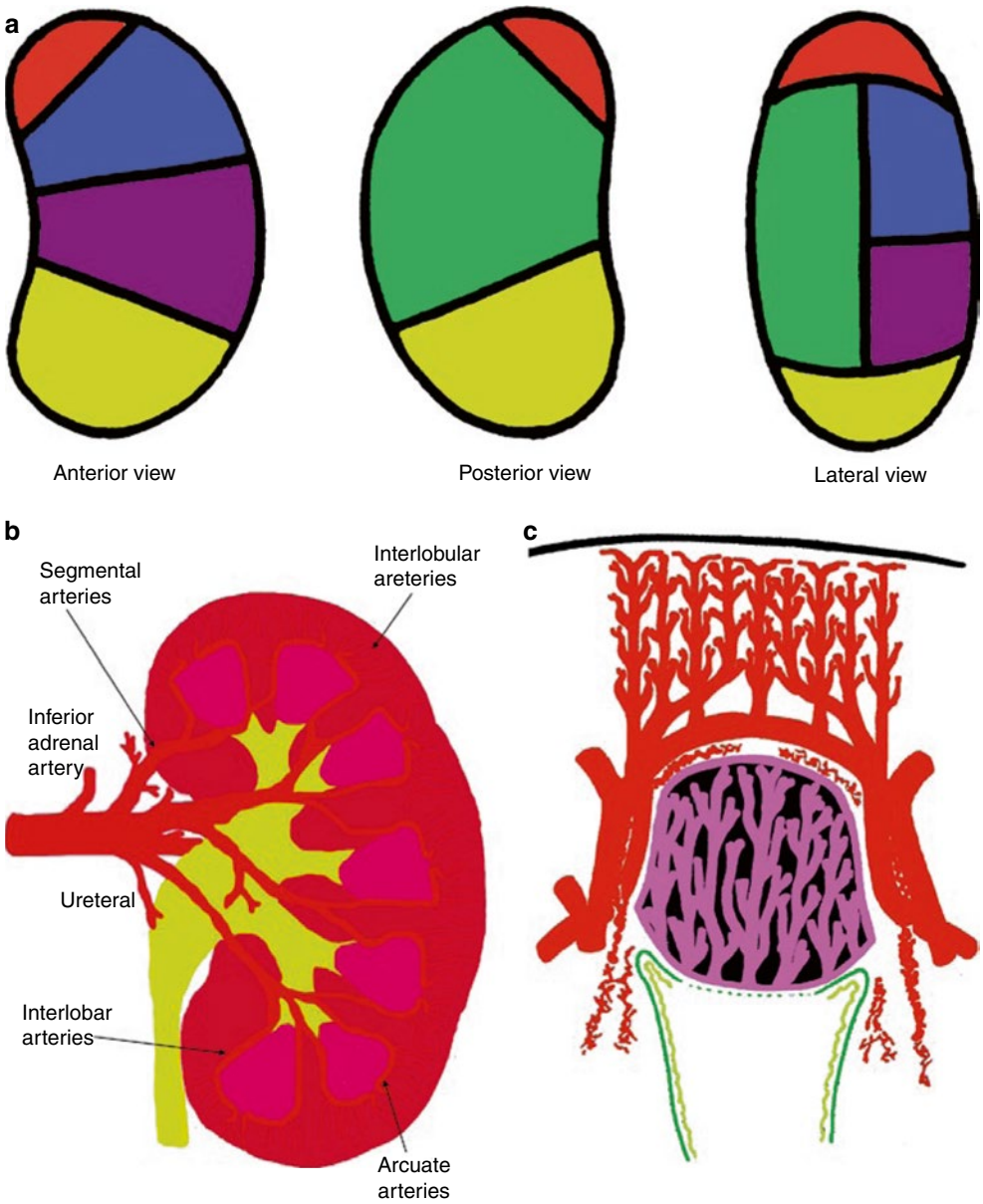

Fig. 2 (**a**–**c**) Normal intrarenal arterial vessels. (**a**) Vascular areas of the renal parenchyma vascularized by the different segmental arteries and represented according to the anterior posterior and lateral views. The vascular areas are described as superior (*red*), anterior superior (*blue*), posterior (*green*), anterior inferior (*violet*), and inferior (*yellow*). (**b**) Segmental, interlobar, interlobular, and arcuate arteries represent the different branches of the renal arteries. (**c**) The renal medulla presents a relationship with the interlobar and arcuate arteries while the interlobular arteries reach the renal cortical surface

1.1.2 Microscopic Renal Anatomy and Nephron Physiology

The cortex of each human kidney contains the glomeruli of 1–1.5 million nephrons. The afferent artery intimately interacts with the glomerular portion of the nephron, where the afferent artery breaks into a capillary network named the glomerular capillary tuft from which originates the efferent artery. The glomerular vessels are contained within Bowman's capsule forming the Malpighian corpuscle (Fig. 4a). The Malpighian corpuscles represent small, round, deep red bodies in the cortex of the kidney, each communicating with a renal tubule. They average about 0.2 mm in diameter, with each capsule composed of two parts: a central glomerulus and a glomerular capsule, also called Bowman's capsule. Bowman's capsule represents the glomerular portion of the nephron and is a double-walled, cup-shaped structure around the glomerulus of each nephron and at the beginning of the tubular component of a nephron. The filtration barrier is composed of three layers corresponding to capillary endothelium; the basement membrane composed of glycoproteins, collagens, and mucopolysaccharides; and the epithelium of Bowman's capsule. The basement membrane presents an average thickness in adults of 3,200 Å and contains three distinct areas: a central electron dense lamina densa and, on either side, a lamina rara externa and lamina rara interna (Fig. 4a). Thickening of the basement membrane is seen in a number of glomerular diseases.

The epithelial cells that surround the capillary tuft differ from those forming the rest of Bowman's capsule, because they present numerous foot processes or pedicles which

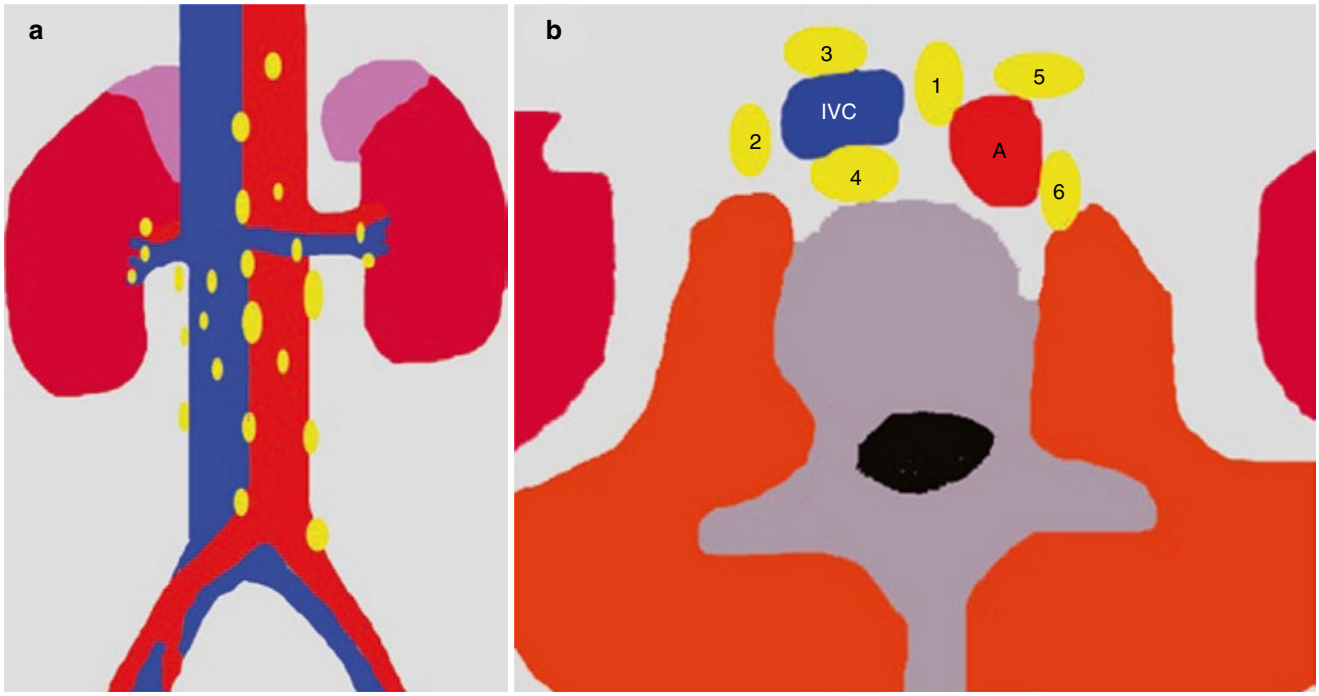

Fig. 3 (**a**) Regional lymph nodes of the kidneys; (**b**) abdominal para-aortic (periaortic) lymph nodes including the interaortocaval (*group 1*), paracaval (*group 2*), precaval (*group 3*), retrocaval (*group 4*), preaortic (*group 5*), and retroaortic lymph nodes (*group 6*). *IVC* inferior vena cava, *A* aorta

come into contact with the lamina rara externa of the basement membrane and are called podocytes (Fig. 4a). Between the foot processes is a space, named filtration split or split pore, 250–400 Å wide which is covered by a thin membrane, named the filtration slit diaphragm and located approximately 600 Å from the basement membrane. Interspread between the adjacent capillaries, the mesangium, containing mesangial cells and mesangial matrix, appears to provide support for the glomerular capillaries. Usually, the term glomerulus includes both the nephron and capillary components. At the glomerulus, the blood reaches a highly disfavorable pressure gradient and a large exchange surface area, which forces the serum portion of the blood out of the vessel into the renal tubules. About 20 % of the water in plasma entering the afferent artery filters out the glomerular capillary into the Bowman's space.

Fluids from blood in the glomerulus are collected in the Bowman's capsule forming the glomerular filtrate and further processed along the nephron to form urine. This process is known as ultrafiltration, which is performed by the glomerulus and then by the nephron (Fig. 4b). Flow continues through the renal tubules, including the proximal convoluted tubule, to the loop of Henle with the thick ascending and thin descending limb and finally leaves the kidney by means of the collecting duct, leading to the renal ureter. The proximal tubule has traditionally been divided into the proximal convoluted tubule, which contorts itself in an apparently random fashion in the renal cortex, and the proximal straight tubule (or pars recta). The epithelial cells of the proximal tubule have a cuboidal shape (Laiken and Fanestil 1985). A layer of closely packed microvilli covers the luminal surface forming a brush border. The proximal tubule is responsible for the initial processing of the glomerular filtrate, and it both reabsorbs approximately two thirds of the filtered water and sodium (with bicarbonate instead of chloride) and almost all the filtered glucose and amino acids from the tubular fluid and secretes organic acids (e.g., uric acid) and bases such as drugs (including diuretics) and drug metabolites into the tubular fluid. Sodium reabsorption in the proximal tubule occurs in cells and intercellular spaces. Entry of sodium across luminal membranes is passive and occurs by diffusion, coupled to the transport of other solutes (e.g., glucose, amino acids, phosphate), and in exchange with protons secreted from cell to lumen and reabsorption of bicarbonate. Sodium extrusion from cells into the intercellular spaces and across the basolateral membrane is an active process, which is accomplished by the sodium–potassium pump (Na^+–K^+-ATPase). Chloride is reabsorbed due to the diffusion gradient from the tubular lumen to the peritubular capillary.

The loop of Henle consists of a descending limb and an ascending limb. Most renal physiologists consider the loop of Henle to begin at the end of the proximal straight tubule (Laiken and Fanestil 1985) (Fig. 4b). Here the cuboidal epithelial cells of the proximal tubule are replaced by flat, squamous epithelial cells with a small number of short microvilli. This segment of the tubule is called the thin descending limb

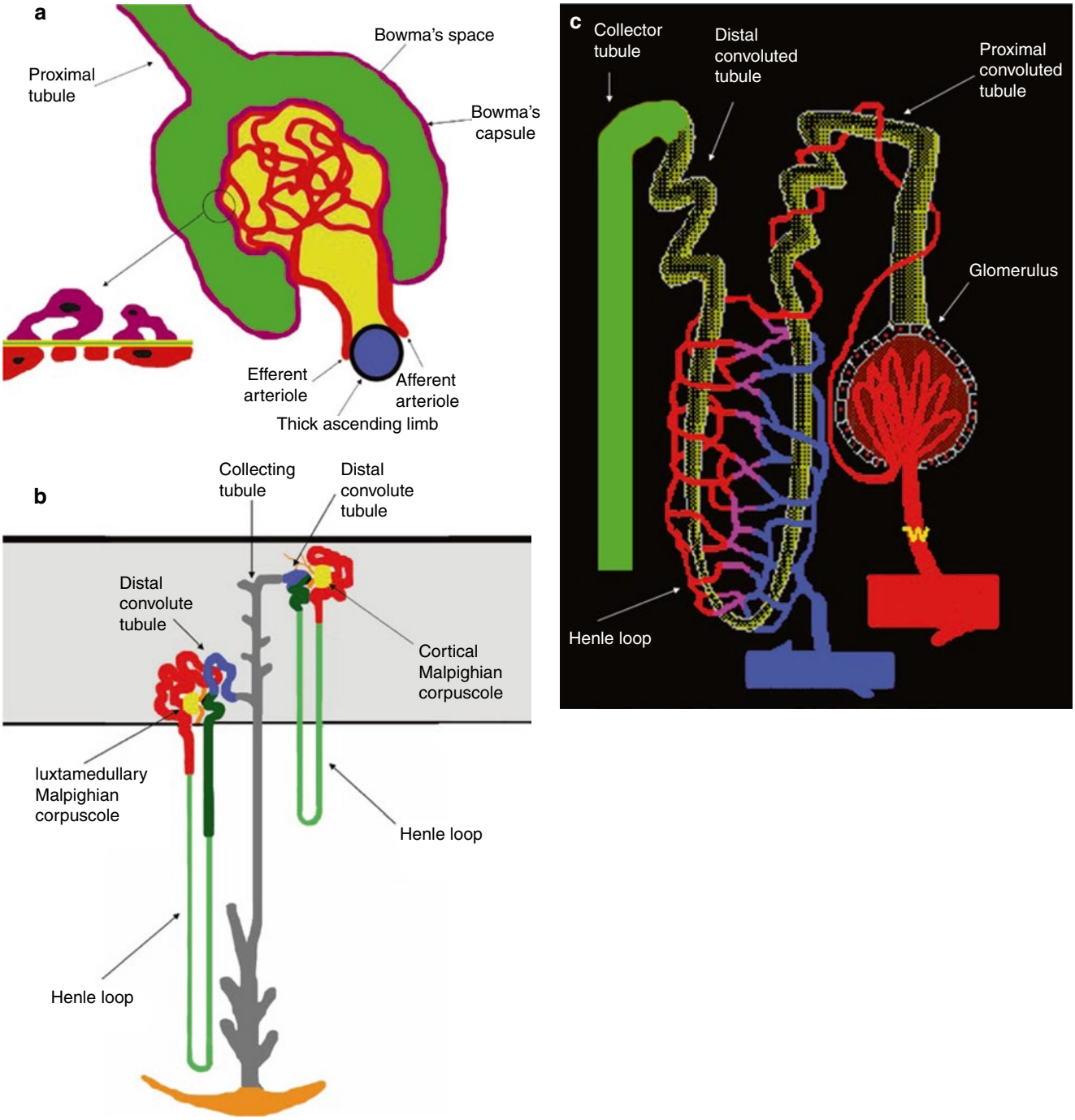

Fig. 4 (**a**) Scheme of the Malpighian corpuscle. Mesangium with mesangial cells is represented in *dark yellow*. The filtration barrier is composed of three layers corresponding to the capillary endothelium (*red*), the basement membrane, and the epithelium of Bowman's capsule (*violet*). The basement contains three distinct areas, a central electron dense lamina densa (*green*) and a lamina rara externa and lamina rara interna (*light yellow*). The epithelial cells that surround the capillary tuft differ from those forming the rest of Bowman's capsule, because they present numerous foot processes or pedicles which come into contact with the lamina rara externa of the basement membrane and are called podocytes. (**b**) Scheme of cortical and juxtamedullary nephrons within the renal cortex (*gray color*), the proximal tubule (*red*), the loop of Henle (thin descending limb, *light green*; thick ascending limb, *dark green*), the distal convoluted tubule (*blue*), and the connecting and collecting tubule (*gray*). The juxtaglomerular apparatus is represented in *black*. The loop of Henle begins at the end of the proximal straight tubule. In cortical nephrons the hairpin turn that forms the tip of the loop of Henle occurs not deeper than the junction between the outer and inner zones of the medulla, whereas in the juxtamedullary nephrons the hairpin turn may occur as deeply as the tip of papilla. (**c**) Scheme of the branches of the efferent arteries vascularizing the different regions of the nephrons forming the peritubular capillaries

since the epithelial cell layer is very flat. The thin descending limb of the juxtamedullary nephrons is substantially longer than that of cortical nephrons (Fig. 4b). In cortical nephrons the hairpin turn that forms the tip of the loop of Henle occurs not deeper than the junction between the outer and inner zones of the medulla, whereas in the juxtamedullary nephrons the hairpin turn may occur as deeply as the tip of the papilla. In juxtamedullary nephrons the ascending limb begins with a segment of flat, squamous epithelial cells, termed the thin ascending limb. At the junction between the inner and outer zones of the renal medulla, the thick ascending limb begins (Laiken and Fanestil 1985). In this segment, the epithelial cells are cuboidal and contain numerous mitochondria like the epithelial cells of the proximal tubule, even though these cells lack a luminal brush border. The thick ascending limb transverses the outer zone of the medulla (the medullary portion of the thick ascending limb) and then ascends through the renal cortex to the level of its nephron's glomerulus. In cortical nephrons, the ascending limb consists entirely of cuboidal epithelial cells, and cortical nephrons lack a thin ascending limb (Laiken and Fanestil 1985). The loop of Henle dissociates the absorption of sodium and water. The descending limb of Henle passively abstracts water into the hypertonic medullary interstitium, concentrating the tubular fluid, while the essentially water-impermeable thick ascending limb of Henle actively absorbs approximately 25 % of filtered sodium chloride but little water (Andreoli 1992). In the thick ascending limb of the loop of Henle, sodium and potassium cross the luminal cell membrane together with two chlorides by a carrier-mediated uptake ($Na^+/K^+/2Cl^-$) under the energy of sodium–potassium ATPase on the basolateral membrane. The loop diuretics inhibit the apical cotransport system, thereby enhancing the sodium and chloride secretion.

In each nephron the thick ascending limb returns to the glomerulus of its own origin and contacts its originating glomerulus at the vascular pole, the region where the afferent and efferent arterioles, respectively, enter and leave the glomerulus (Fig. 4a, b). A specialized structure, the juxtaglomerular apparatus, is found at this contact point consisting of three components: the macula densa, the extraglomerular mesangial cells, and the granular cells secreting renin. The juxtaglomerular apparatus is made up of specialized cells in the wall of the afferent arteriole and granular cells in the wall of the distal tubule (the macula densa). This area is innervated by adrenergic fibers and the granular cells carry renin in intracellular granules.

The distal nephron includes the distal convoluted tubule, the connecting tubule, and the collecting tubule (or duct) which can be subdivided into cortical collecting tubule, medullary collecting duct, and papillary collecting duct. The distal convoluted tubule primarily absorbs sodium by the sodium–potassium pump (Na^+–K^+-ATPase) under the influence of aldosterone and secretes protons, ammonia, and potassium in the tubular lumen. Aldosterone and other mineralocorticoids stimulate the rate of sodium absorption in the distal nephron. Aldosterone also increases the rate of net potassium secretion and net proton secretion (and consequently the rate of bicarbonate regeneration) by the distal nephron. The collecting tubule/duct develops from the ureteral bud, and the connecting tubule represents the connection between the embryonic nephron and the ureteral bud. The collecting duct system regulates the osmolality of the urine by absorbing water under the influence of the antidiuretic hormone (ADH), and tubular fluid equilibrates osmotically with the hypertonic medullary interstitium. ADH promotes the formation of a hypertonic urine both by increasing the rate of salt absorption in the thick ascending limb of Henle and by increasing the water permeability of the collecting duct system (Andreoli 1992).

The efferent artery disperses into a second capillary network that surrounds the tubular portion of the nephron (Fig. 4c), delivering substances for tubules to secrete into the tubular fluid and taking up water and solutes reabsorbed by the tubule. Most of the capillaries in this second network surround the tubules in the cortex and are termed peritubular capillaries. Some of these capillaries in the juxtamedullary nephrons, called vasa recta, descend to varying depths in the medulla before forming a capillary network and reunite while turning around and ascend back to the renal cortex. From the peritubular capillaries and vasa recta, blood flows into the peritubular veins and is drained by the renal veins.

1.2 Normal Renal Physiology

The principal function of the mammalian kidney is to maintain homeostasis or equilibrium between our internal volume and electrolyte status and that of the environment's influences, diet, and intake. It functions to maintain our intra- and extracellular fluid status at a constant, despite the wide variety of daily fluid and electrolyte intake. In man, the kidneys consist of two to three million nephrons (Fig. 4) and weigh only 250–300 g. The kidneys' extraordinary excretory and regulatory objectives are achieved through the processes of glomerular ultrafiltration, tubular reabsorption, and tubular secretion. To a large extent, these excretory and regulatory processes depend on the blood supply to the kidneys.

The kidneys receive the highest blood flow per gram of organ weight in the body at 1 L/min. The renal blood flow is to consider the renal fraction, which corresponds to the fraction of the total cardiac output that flows through the kidneys.

The kidneys are highly vascularized parenchymas, and a 70-kg man with a cardiac output of 6 L/min has a normal renal blood flow of about 1.2 L/min corresponding to 20 % of the cardiac output. Considering the fact that each kidney in a normal 70-kg man weighs about 130–170 g, for a total weight of about 300 g of kidney, the average flow per gram of kidney weight (perfusion value) is about 400 mL/min/100 g. This is several times greater per unit weight of organ than the blood flow through most other organs. During various stress conditions or diseases, this renal fraction can vary considerably and be markedly affected. Blood flow to the kidneys will be dependent on a number of important systemic factors. Clearly, if there is a problem with volume (dehydration, hemorrhage) or cardiac output (congestive heart failure, myocardial infarct), blood flow is diminished. In less obvious ways, hypoalbuminemia (cirrhosis, nephrotic syndrome, and starvation) affects the intravascular volume so that the effective blood (volume) flow is diminished, despite many of these patients appearing with total body fluid overloaded. Finally, hypotension from severe vasodilatation (anaphylactic shock, sepsis) would also diminish blood flow to the kidneys.

Oxygen consumption by the kidneys is quite high and amounts to about 8 % of the total oxygen consumption of the body. Oxygen delivery to any organ is directly dependent on hemoglobin content (blood) and cardiac output (blood flow). As in other tissues, an important function of blood flow is to provide adequate oxygenation and nutrition. Therefore, the relatively high blood flow to the kidneys exists to feed its metabolic demands as well as to allow ultrafiltration. In fact, the renal blood flow is so high that only a small percent of the available oxygen is extracted from the blood perfusing the kidneys.

The fundamental parameter to indicate the renal function is glomerular filtration rate (GFR) corresponding to the volume of water filtered out of the plasma through glomerular capillary walls into Bowman's capsules per unit of time. The normal value of the GFR is above 90 mL/min/1.73 m^2. The initial step in urine formation (ultrafiltration) occurs across the glomerular wall (Klahr 1992). The difference in hydrostatic pressure between the glomerular capillary pressure (P_{GC}) and Bowman's space (P_{BS}) favors filtration, whereas the colloid osmotic pressure inside the glomerular capillaries (Π_{GC}) opposes it:

$$\mathrm{GFR} = K_{uf}\left[\left(P_{GC} - P_{BS}\right) - \Pi_{GC}\right] \qquad (1)$$

K_{uf} corresponds to the ultrafiltration coefficient and is a function of both the total capillary surface and the permeability per unit of surface area. Bowman's space (P_{BS}) pressure and the hydrostatic pressure (P_{GC}) remain relatively constant along the glomerular capillaries, while the colloid osmotic pressure (Π_{GC}) undergoes a large progressive increase because the filtration of protein-free fluid results in an increase of protein concentration along the capillary lumen. Hence, the mean effective pressure for ultrafiltration decreases along the glomerular capillaries and becomes zero before the end of the capillary (Klahr 1992) with consequent end of filtration. Thus, the GFR is highly dependent on the glomerular plasma flow rate because, at high flow rates, a slower rise in the colloid osmotic pressure occurs and glomerular filtration increases since it takes place across a greater length of the capillary (Klahr 1992).

The autoregulatory system accomplishes this by maintaining the glomerular capillary pressure around 60–70 mmHg. Renal blood flow and GFR are autoregulated within a wide range of renal arterial pressure. This ability to maintain renal perfusion pressure and P_{GC} is impaired when mean arterial pressure drops below 70 mmHg. Unless cardiac output is severely reduced, however, GFR usually remains near normal. GFR is protected from reduced cardiac output and arterial pressure by autoregulation (Cohen 1991), which involves the local activation of the renin–angiotensin system in the juxtaglomerular apparatus via myogenic receptors in the wall of the afferent arteriole, and granular cells carry renin in intracellular granules in the wall of the distal tubule (the macula densa). These sense blood pressure changes through stretch receptors and respond accordingly through relaxation or constriction. Renin, a glycoprotein of 340 amino acids, is produced in the granular cells as a precursor protein (prorenin) that is cleaved to yield active renin (Baxter 1992). The granular cells of the juxtaglomerular apparatus release renin into the circulation where it has a half-life of around 15 min. The release of renin can be induced by altered sodium concentration at the macula densa of the distal tubule (tubuloglomerular feedback loop), by changes in the blood flow patterns of the afferent arteriole or by adrenergic stimulation. Renin acts in the plasma and cleaves the renin substrate angiotensinogen, secreted by the liver, to yield the decapeptide angiotensin I. Angiotensin I is not known to have a physiologically important action, while it serves as a substrate for the production of angiotensin II. The conversion of angiotensin I to the octapeptide angiotensin II is catalyzed by angiotensin converting enzyme that is present in a number of tissues and in high concentration in the lung. Angiotensin II is a potent vasoconstrictor and appears to constrict the efferent glomerular arteriole selectively (Cohen 1991). Angiotensin II is also a potent stimulator of aldosterone release from the adrenal glands. The afferent arteriole will respond to changes in renal perfusion pressure by either vasoconstriction or vasodilatation as a result of a direct myogenic response. The resultant increase in efferent arteriolar resistance maintains hydrostatic pressure within the glomerular capillaries and GFR (Cohen 1991).

As further endocrine functions of the kidney, besides the renin–angiotensin axis, the prostaglandin production, the operation of the kallikrein–kinin system, and the degradation of low molecular weight proteins should be mentioned. The kidney is also the major site for the synthesis of erythropoietin, which is a glycoprotein produced by renal enzymatic action on a circulating precursor of hepatic origin (Andreoli 1992). The principal action of erythropoietin is to stimulate the rate of red blood cell production by the bone marrow.

1.3 Calculation of Glomerular Filtration Rate (GFR)

Unfortunately, blood urea nitrogen (BUN) and serum creatinine will not be raised above the normal range until 60 % of total kidney function is lost. In particular, serum creatinine is known to be an unreliable indicator of GFR. Approximately 30 % of elderly patients with normal serum creatinine (1.4 mg/dL or less) have chronic kidney disease based on an estimated GFR of less than 60 mL/min/1.73 m^2 (Lane et al. 2009). Thus the serum creatinine concentration may remain within the normal range, despite a substantial decrease in the GFR. Moreover, the creatinine concentration in the blood is affected by a number of factors other than creatinine filtration, including diet, muscle mass, and sex (Lameire et al. 2006). Older patients and women tend to have a lower muscle mass than younger men, and hence, the renal function, namely, the GFR, may be lower than that expected from the serum creatinine.

GFR and creatinine clearance are the two indices that are usually employed to quantify the renal function. Recommendations for evaluating people at increased risk for chronic renal failure are to measure urine albumin to assess kidney damage and to estimate the GFR with an equation based on the level of serum creatinine (Stevens et al. 2006). Many studies support the similarity of creatinine clearance to GFR and its reciprocal relationship with the serum creatinine level. Creatinine clearance rate (C_{Cr}) is the volume of blood plasma that is cleared of creatinine per unit time and is a useful measure for approximating the GFR. Both GFR and C_{Cr} may be accurately calculated by comparative measurements of substances in the blood and urine or estimated by formulas using just a blood test result. The results of these tests are important in assessing the excretory function of the kidneys, and the grading of chronic renal failure and dosage of drugs that are primarily excreted via urine are based on GFR (or C_{Cr}). GFR or its approximation of the creatinine clearance is measured whenever renal disease is suspected or careful dosing of nephrotoxic drugs is required. Creatinine is produced naturally by the body (creatinine is a metabolite of creatine in the muscle).

Creatinine is an amino acid derivative with a molecular mass of 113 Da that is freely filtered by the glomerulus and secreted by the proximal tubule cells. Consequently, the creatinine clearance exceeds the GFR (Stevens et al. 2006). Tubular secretion of creatinine varies among and within individual persons and is influenced by some drugs, including trimethoprim and cimetidine, which inhibit creatinine secretion, thereby reducing creatinine clearance and elevating the serum creatinine level without affecting the GFR. The generation of creatinine is determined primarily by muscle mass and dietary intake, which probably accounts for the variations in the level of serum creatinine observed among different age, geographic, ethnic, and racial groups. Extrarenal elimination of creatinine may be increased at low levels of GFR; this increase is mainly related to the degradation of creatinine by intestinal bacteria and can be affected by the use of antibiotics.

GFR can be calculated by measuring any chemical that has a steady level in the blood and is freely filtered, but neither reabsorbed nor secreted by the kidneys. The rate measured, therefore, is the quantity of the substance in the urine that originated from a calculable volume of blood:

$$\text{GFR} = \frac{\text{urine concentration} \times \text{urine flow}}{\text{plasma concentration}} \qquad (2)$$

The GFR can be determined by injecting inulin into the plasma. Since inulin is neither reabsorbed nor secreted by the kidney after glomerular filtration, its rate of excretion is directly proportional to the rate of filtration of water and solutes across the glomerular filter. Cystatin C, a nonglycosylated basic protein with a low molecular mass (13 kD) that is freely filtered by the glomerulus, is currently under investigation as a replacement for serum creatinine in estimating the GFR since its concentration is independent of muscle mass and does not seem to be correlated with age and sex. After filtration, cystatin C is reabsorbed and catabolized by the tubular epithelial cells; only small amounts are excreted in the urine. Consequently, although cystatin C is cleared by the kidneys, its urinary clearance cannot be measured, which makes the study of the factors affecting its clearance and generation difficult.

In practice, the GFR is often estimated from the serum creatinine level (estimated GFR, eGFR). Creatinine clearance (C_{Cr}) can be calculated if values for creatinine's urine concentration (U_{Cr}), urine flow rate (V), and creatinine's plasma concentration (P_{Cr}) are known. Since the product of urine concentration and urine flow rate yields creatinine's excretion rate, creatinine clearance is also said to be its excretion rate ($U_{Cr} \times V$) divided by its plasma concentration. This is commonly represented mathematically as

$$\mathrm{GFR} = \frac{U_{\mathrm{Cr}} \times V}{P_{\mathrm{Cr}}}. \quad (3)$$

Commonly a 24-h urine collection is undertaken, from empty bladder one morning to the contents of the bladder the following morning, with a comparative blood test then taken. The urinary flow rate is still calculated per minute; hence,

$$\mathrm{GFR} = \frac{U_{\mathrm{Cr}} \times 24-\mathrm{h\ urine\ volume}}{P_{\mathrm{Cr}} \times 24 \times 60\ \mathrm{min}} \quad (4)$$

To allow comparison of results between people of different sizes, C_{Cr} is often corrected for the body surface area (BSA) and expressed compared to the average-sized man as mL/min/1.73 m^2. While most adults have a BSA that approaches 1.7 m^2 (1.6–1.9 m^2), extremely obese or slim patients should have their C_{Cr} corrected for their *actual* BSA, which can be calculated on the basis of the weight and height:

$$C_{\mathrm{Cr\text{-}corrected}} = \frac{C_{\mathrm{Cr}} \times 1.73}{\mathrm{BSA}} \quad (5)$$

The National Kidney Foundation (2002) Kidney Disease Outcome Quality Initiative (K/DOQI; 2002) recommends that clinicians should use an estimated creatinine clearance rate (eC_{Cr}) calculated from the serum creatinine as an index of renal function, rather than serum creatinine alone. A number of formulas have been devised to estimate GFR or C_{Cr} values on the basis of serum creatinine levels. The most widely used equations for estimating GFR are the *Cockcroft–Gault* (1976) and the *Modification of Diet in Renal Disease Study Group* (MDRD) (Levey et al. 1999) formulas.

Cockcroft–Gault (1976) formula may be used to calculate eC_{Cr}, which in turn estimates GFR:

$$\begin{aligned} &e C_{\mathrm{Cr}}\ (\mathrm{mL/min}) = (140 - \mathrm{age\ [years]}) \\ &\times \mathrm{weight\ (kg)}/72 \times S_{\mathrm{Cr}}\ (\mathrm{mg/dL}) \end{aligned} \quad (6)$$

where eC_{Cr} is the estimated creatinine clearance rate and S_{Cr} is the serum creatinine. Resulting value must be multiplicated by 0.85 for women.

$$\begin{aligned} &e C_{\mathrm{Cr}}\ (\mathrm{mL/min}) = (140 - \mathrm{age\ [years]}) \\ &\times \mathrm{weight\ (kg)} \times k/S_{\mathrm{Cr}}\ (\mu\mathrm{mol/L}) \end{aligned} \quad (7)$$

where eC_{Cr} is the estimated creatinine clearance rate, S_{Cr} is the serum creatinine, and k is 1.23 for men and 1.04 for women.

The most recently advocated formula for calculating the GFR is the one that was developed by the MDRD study. The most commonly used formula is the "four-variable MDRD," which estimates GFR using four variables: serum creatinine, age, race, and gender. According to this formula, for creatinine in mg/dL:

$$\begin{aligned} &\mathrm{eGFR\ (mL/min/1.73\ m^2)} = 186 \times S_{\mathrm{Cr}}{}^{-1.154} \\ &\times \mathrm{Age\ (years)}{}^{-0.203} \times [1.210\ \mathrm{if\ black}] \\ &\times [0.742\ \mathrm{if\ female}] \end{aligned} \quad (8)$$

For creatinine in µmol/L:

$$\begin{aligned} &\mathrm{eGFR\ (mL/min/1.73\ m^2)} = 32788 \times S_{\mathrm{Cr}}{}^{-1.154} \\ &\times \mathrm{Age\ (years)}{}^{-0.203} \times [1.210\ \mathrm{if\ black}] \\ &\times [0.742\ \mathrm{if\ female}] \end{aligned} \quad (9)$$

Considering also the serum albumin and blood urea nitrogen (BUN) levels,

$$\begin{aligned} &\mathrm{eGFR\ (mL/min/1.73\ m^2)} = 170 \times S_{\mathrm{Cr}}{}^{-0.999} \\ &\times \mathrm{Age\ (years)}{}^{-0.176} \times [1.180\ \mathrm{if\ black}] \\ &\times [0.762\ \mathrm{if\ female}] \times \mathrm{BUN}{}^{-0.170} \times \mathrm{Albumin}{}^{+0.318} \end{aligned} \quad (10)$$

where the creatinine and BUN concentrations are both in mg/dL. The albumin concentration is in g/dL.

These MDRD equations are to be used only if the laboratory has not calibrated its serum creatinine measurements to isotope dilution mass spectrometry. When isotope dilution mass spectrometry-calibrated serum creatinine is used (which is about 6 % lower), the above equations should be multiplied by 0.94086.

Creatinine levels in µmol/L can be converted to mg/dL by dividing them by 88.4. The equations have been validated in patients with chronic kidney disease. MDRD equation versions underestimate the GFR in healthy patients with GFRs over 60 mL/min and in heavy patients and overestimate it for underweight people, while the equations have not been validated in acute renal failure.

In the equation used in MDRD, the factors of age, sex, and race are surrogates for muscle mass (Stevens and Levey 2005). Many chronic illnesses, including cardiovascular disease, affect muscle mass through malnutrition, inflammation, and deconditioning. Thus people with chronic illness are more likely to have lower levels of serum creatinine than are healthy people, even for the same level of GFR and the same age, sex, and race. In such persons, estimating equations based on serum creatinine may overestimate GFR. It must be emphasized that both the *Cockcroft–Gault* and *MDRD* equations can only provide estimates of GFR, and where there is doubt about renal function, direct GFR measurement is preferable (Lameire et al. 2006).

The Chronic Kidney Disease Epidemiology Collaboration (CKD-EPI) formula (Levey et al. 2009) was developed in an effort to create a formula more accurate than the MDRD formula, especially when actual GFR is greater than 60 mL/min per 1.73 m^2:

$$\mathrm{eGFR}\left(\mathrm{mL/min/1.73\,m^2}\right) = 141 \times \min\left(S_{\mathrm{Cr}}/k, 1\right)^{a} \times \max\left(S_{\mathrm{Cr}}/k, 1\right)^{-1,209}\ x\, 0.933^{\mathrm{Age}} \times \left[1.159\,\mathrm{if\ black}\right] \times \left[1.018\,\mathrm{if\ female}\right] \quad (11)$$

where S_{Cr} is the serum creatinine (mg/dL), k is 0.7 for females and 0.9 for males, a is −0.329 for females and −0.411 for males, min indicates the minimum of S_{Cr}/k or 1, and max indicates the maximum of S_{Cr}/k or 1.

Another estimation tool to calculate GFR is the Mayo Quadratic formula (Rule et al. (2004) to improve the estimation of the GFR in patients with preserved kidney function due to the underestimation of the GFR in patients with preserved kidney function:

$$\mathrm{eGFR}\left(\mathrm{mL}/\mathrm{min}/1.73\ \mathrm{m}^2\right)=\exp\left(1.911+5.249/S_{\mathrm{Cr}}-2.114/S_{\mathrm{Cr}}{}^2-0.00686\times\mathrm{Age}-\left[0.205\ \text{if female}\right]\right) \quad (12)$$

In children, the *Schwartz formula* (1984) is used (Schwartz et al. 1984). This employs the serum creatinine (mg/dL), the child's height (cm), and a constant to estimate the GFR:

$$\mathrm{eGFR}=k\times\mathrm{height}\left(\mathrm{cm}\right)/S_{\mathrm{Cr}}\left(\mathrm{mg}/\mathrm{dL}\right) \quad (13)$$

where k is a constant that depends on muscle mass, which itself varies with a child's age. In the first year of life, for preterm babies $k=0.33$, and for full-term infants $k=0.45$. For infants between 1 and 12 years of age, $k=0.55$. The method of selection of the k-constant value has been questioned as being dependent upon the gold standard of renal function used (i.e., creatinine clearance, inulin clearance, etc.) and also may be dependent upon the urinary flow rate at the time of measurement.

For most patients, a GFR over 60 mL/min is adequate. But, if the GFR has significantly declined from a previous test result, this can be an early indicator of kidney disease requiring medical intervention. The sooner the kidney dysfunction is diagnosed and treated, the greater the odds of preserving remaining nephrons and preventing the need for dialysis. The normal ranges of GFR, adjusted for BSA, are 70 ± 14 mL/min/m^2 for males and 60 ± 10 mL/min/m^2 for females.

1.4 Calculation of Glomerular Filtration Rate (GFR) in Acute Renal Failure

Measurement and estimation of GFR in acute renal failure present numerous challenges (Dagher et al. 2003). Serum creatinine concentration alone will provide inaccurate information of eGFR when the GFR is rapidly changing or before it is reaching an equilibrium value. Thus equations to estimate creatinine clearance from serum creatinine cannot be used. In addition, clearance also inaccurately estimates true GFR because of tubular secretion of creatinine.

Oral cimetidine, a blocker of tubular creatinine secretion, improves the accuracy of measuring creatinine clearance, but requires a pretreatment period (Dagher et al. 2003). In addition, the GFR measurements after cimetidine administration have not been validated in patients with acute renal failure. Urinary clearance of GFR markers may provide better information. Thus, if a bolus of a marker such as inulin was administered intravenously and its urinary clearance measured, an estimate of GFR can be obtained (Dagher et al. 2003).

The choice of the GFR marker such as inulin, 125-I iothalamate, and others has been validated in patients with stable renal function. These measurements presume the marker is filtered, not metabolized, neither reabsorbed nor secreted by the tubule, and can be reliably measured in the blood and urine. However, with tubular obstruction and backleak, these assumptions may not hold true. Leakage of substances filtered at the glomerulus, but which leak back across the tubular epithelium, may underestimate GFR in ARF. The permeability to those substances most commonly used for filtration rate determination, such as inulin, may be the principal cause of this phenomenon. Distal recovery of inulin is reduced by only 15 % in kidneys showing severely restricted renal function in animal models (Olbricht et al. 1977). Thus the reduction in whole kidney inulin clearance reflects primarily a reduction in GFR.

GFR can be measured by various methods in patients with acute renal failure, including the continuous infusion method, the standard clearance method, or the plasma clearance method. The infusion method consists in the infusion at a constant rate, usually following a bolus-loading dose, of a known concentration of GFR marker. Since the GFR is often unstable in patients with ARF, a steady state may not be achieved, a major assumption underlying this method. Therefore, this method is not suitable for use in patients with ARF.

In calculating GFR by the standard clearance method, bolus and infusion of a GFR marker is carried out in a manner identical to the above. In addition, urine is collected at three to six timed intervals of 20–30 min each in a water-loaded state (Dagher et al. 2003). The urine flow rate (V) and urinary iothalamate concentration (U) are recorded. Peripheral venous blood is drawn immediately before and after the urine collection period for measurement of plasma maker concentration (P). P represents the logarithmic

average of the marker concentration before and after the collection period. The renal clearance is calculated by the formula:

$$\mathrm{GFR} = \frac{U \times V}{P}$$

This method lends itself well to the estimation of GFR in ARF when hemodynamic changes can be rapid. By collecting urine and plasma at timed intervals, rapid changes in GFR can be detected.

2 Normal Radiological Anatomy of the Renal Parenchyma, Intrarenal Vasculature, and Anatomical Variants

2.1 Conventional Radiography

The longitudinal (Fig. 5a) and transverse (Fig. 5b) represent the two fundamental planes employed for renal imaging. The conventional plain radiography of the abdomen, or kidney–ureter–bladder (KUB) radiograph, is a first-line imaging technique in the assessment of the kidney. It is performed in the anteroposterior projection with the patient in the upright or supine position. It is indicated to evaluate the renal shape, margins, dimensions, and location and to identify renal calcifications, stones, or transparencies due to fat or gas.

On the abdomen plain radiography, both kidneys are clearly visible due to the natural contrast provided by the perirenal fat (Fig. 6) and can be assessed regarding their position, morphology, margins, and dimensions. In normal adults both kidneys present a longitudinal diameter of 9–12 cm, and a latero-lateral diameter of 3–5 cm, and should not have a difference in the largest longitudinal diameter higher than 1.5 cm. In the long body habitus subjects, the longitudinal diameter may exceed the highest range, while in the short body habitus subjects, the normal 15–20° inclination of the renal longitudinal diameter on the frontal plane may be much higher with an apparent reduction of the longitudinal diameter on the anteroposterior projection. The psoas muscle profile is another important parameter to evaluate since it is canceled by the intestinal meteorism or by retroperitoneal effusions.

The fundamental radiopacities that should be detected at the conventional plain radiograph of the abdomen (Fig. 7) correspond to renal stones or calcifications due to vascular structures, chronic inflammations (e.g., tuberculosis), traumatic lesions (e.g., hematoma), or solid or cystic neoplasms.

The fundamental radiolucencies visible on plain radiography are determined by gas (e.g., emphysematous pyelonephritis, Fig. 8) or fat (e.g., angiomyolipomas, liposarcomas, renal sinus lipomatosis).

2.2 Grayscale and Doppler Ultrasound

Grayscale US is a reliable technique for renal dimension assessment, even though renal volume is influenced by patient age and hydration. In a newborn's kidneys (Fig. 9), the renal cortex is iso- or hyperechoic to liver and spleen parenchyma (Kasap et al. 2006), whereas pyramids are more prominent than in adults. The renal cortex hyperechogenicity compared to the liver is more evident in premature infants. This is because in a newborn, during the first 2 months of

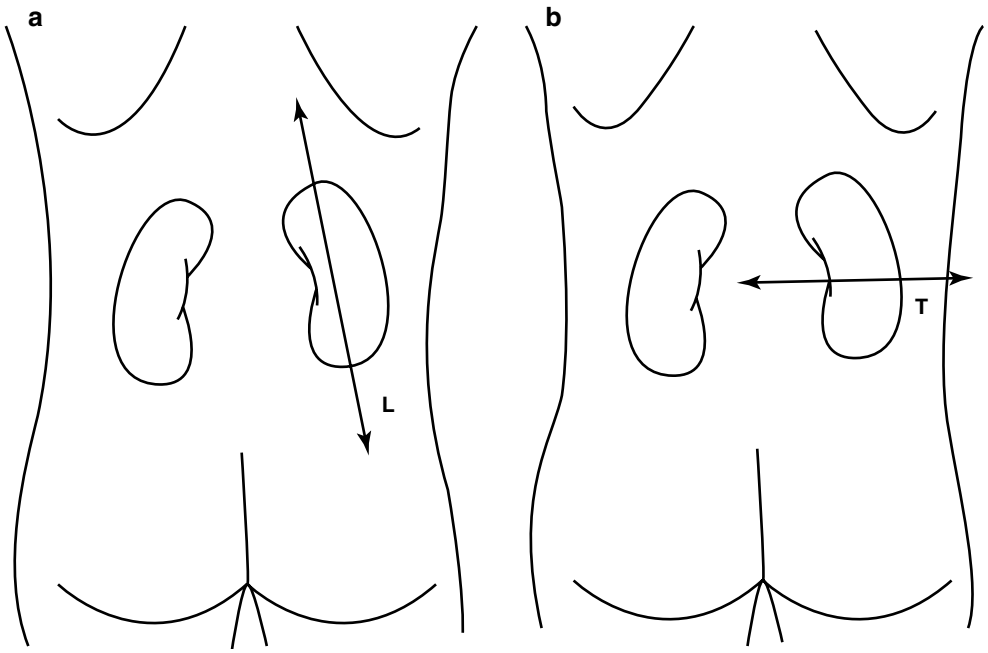

Fig. 5 (**a**, **b**) Fundamental planes employed for renal imaging. The longitudinal axis (**a**) is parallel to the major diameter of each kidney. The transverse axis (**b**) is perpendicular to the major diameter of each kidney

life, the kidney loops of Henle are still within the cortex in large percentage, while the glomeruli occupy proportionately a greater volume of the renal cortex than in adults and an increased number of acoustical interfaces results (Hricak et al. 1983). However, an unusually increased renal echogenicity in newborns may be observed in infantile polycystic kidney disease, hemolytic uremic syndrome, and renal vein thrombosis (Chiara et al. 1990). Compound calyces and associated compound pyramids are present in the upper and lower renal poles in newborns and may appear as large irregular hypoechoic areas, mimicking an obstructed pole of a duplex collecting system, focal caliectasis, hydrocalyx, a cyst, or a hypoechoic mass. Neonatal kidneys also show a paucity of renal sinus echoes due to a minimal renal sinus fat. Within 2–6 months, the kidneys become progressively less echogenic than the liver and assume the features of the adult kidney between 6 and 24 months of life.

In a normal adult, the length of both kidneys is considered normal when it is comprised between 9 and 12 cm. Normally, renal margins are smooth, except in some normal anatomical variants such as functional parenchymal defects and renal fetal lobations. In normal adults, the mean normal value of renal cortical thickness (distance between the renal capsule and the outer margin of the pyramid) is 1–1.5 cm, while the normal value of renal parenchyma thickness (distance between the renal capsule and the margin of the sinus echo avoiding renal columns) is 1.4–2.2 cm and decreases with age (Gourtsoyiannis et al. 1990). Renal cortical echogenicity is normally lower than the echogenicity of the liver, spleen, and renal sinus (Fig. 10). When liver parenchyma appears hyperechoic on US, spleen echogenicity is used as a standard reference; however, kidneys may be isoechoic to the liver even when no clinical or laboratory evidence of renal disease is documented. Renal cortical echogenicity is correlated to severity of histological changes in renal parenchymal diseases such as global sclerosis, focal tubular atrophy, and hyaline casts per glomerulus. On US, renal pyramids appear triangular and hypoechoic and may be differentiated from the renal cortex in approximately 50 % of adult patients (Fig. 10), being more conspicuous in slim patients and children and with hydration and diuresis. Renal sinus appears hyperechoic if compared with renal parenchyma, for the presence of hilar adipose tissue with fibrous septa, blood vessels, and lymphatics. Renal sinus may appear inhomogeneous, less echogenic, and poorly differentiated from renal parenchyma when edema, fibrosis, or cellular infiltration are present. With increasing age, amount of renal parenchyma decreases and renal sinus fat increases with the evidence of renal contour irregularities due to vascular scars or nephrosclerosis (Fig. 11). Renal sinus fat tissue may also be increased in renal sinus lipomatosis, which can be determined by obesity, parenchymal atrophy, and normal variants.

Fig. 6 Conventional plain radiograph of the abdomen. The kidneys (*arrows*) are easily identified due to the natural contrast provided by the perirenal fat which allows the differentiation between the kidneys and the psoas muscle

Color and power Doppler US accurately depict renal vessels (Fig. 12) with possible assessment of single vessel flows by pulsed Doppler interrogation (Fig. 13). Renal parenchymal arterial and venous vessels have to be evaluated by color and power Doppler by using low wall filter, flow optimization for slow flows with low-pulse repetition frequency, and by appropriate gain setting with the lowest possible level of noise.

The assessment of renal vascular resistances is obtained by Doppler waveform analysis (Fig. 13), obtaining resistive indices (RIs) which correspond to peak systolic velocity minus end-diastolic velocity divided by peak systolic velocity. Increased sensitivity of color Doppler and power Doppler provided by the latest digital US equipment allows depiction and Doppler interrogation of the renal parenchymal vessels up to the interlobular arteries. The RIs measured on segmental, interlobar, and arcuate renal parenchymal arteries are normally below 0.70 and decrease progressively from segmental to interlobular vessels. RIs are significantly higher in elderly subjects. Studies that correlate RIs values with biopsy findings in various renal parenchymal diseases have revealed that kidneys with active disease in tubulointerstitial or vascular compartment present elevated RIs (>0.80), whereas kidneys with glomerular diseases present more often normal RIs values.

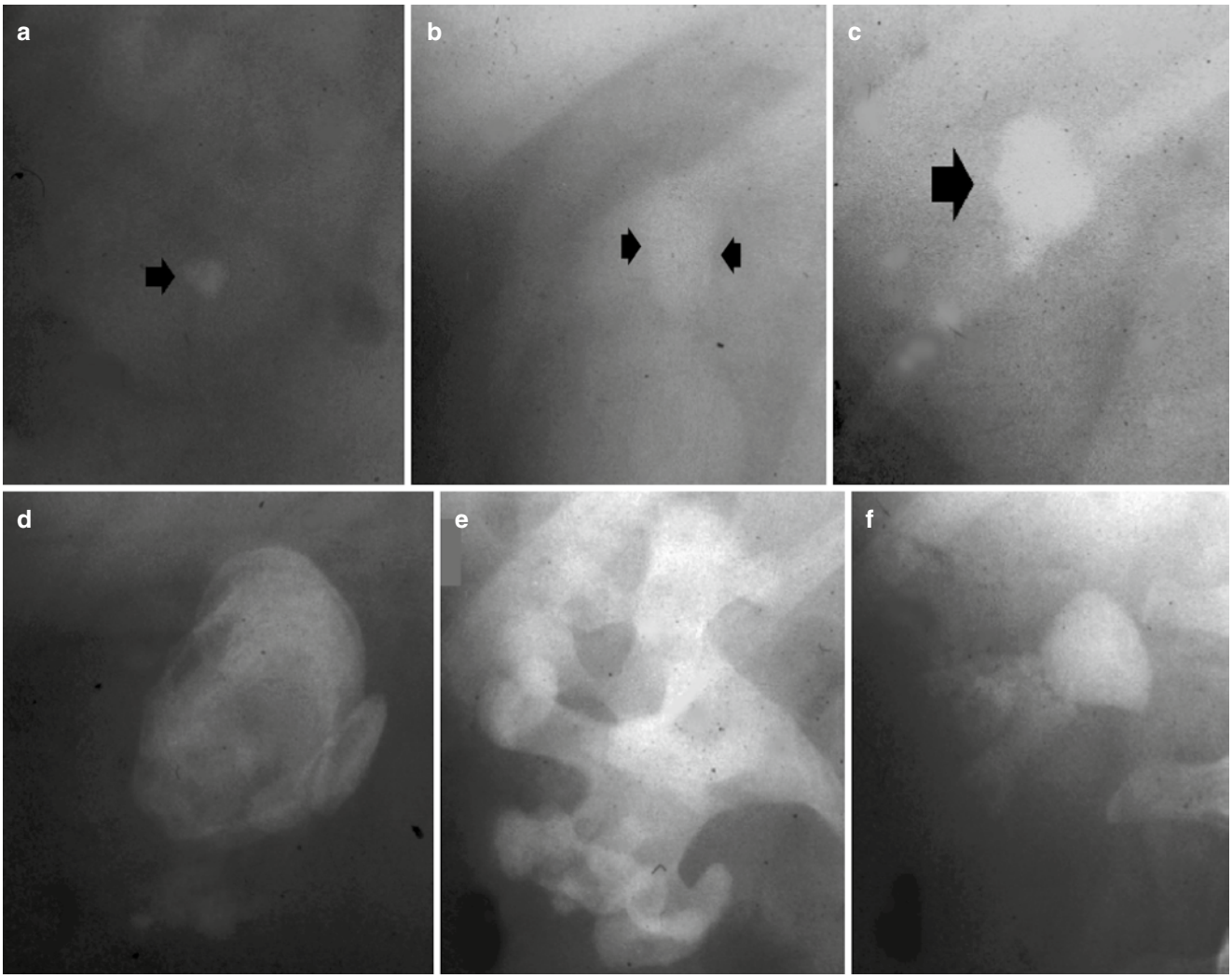

Fig. 7 (**a**–**f**) Plain radiograph. Different type of high-density opacities (*arrows*) projecting on the renal anatomical site. (**a**) Stone; (**b**–**e**) different type of staghorn stone; (**f**) putty kidney

2.3 Computed Tomography

Current generation multidetector computed tomography (CT) scanners allow the acquisition of volumetric data. Such data can be used to generate both submillimetric transverse images and thicker reconstructed transverse sections with increased signal-to-noise ratio (SNR). CT is the ideal technique to scan the retroperitoneal organs. Both kidneys are placed in the perirenal retroperitoneal space, which is delimited by the anterior pararenal fascia (Gerota's fascia) and posterior pararenal fascia (Zuckerkandl's fascia) (see chapter "Normal radiological anatomy of the retroperitoneum"). The kidneys are connected to the pararenal fasciae by the renofascial fibrotic septa, which rely on the perirenal fat.

The renal parenchyma is homogeneous on unenhanced CT with a density ranging from 30 to 60 HU, which increases up to 80–120 HU after iodinated contrast agent administration (Davidson et al. 2006). Renal sinus and perinephric fat provide intrinsic contrast for the renal parenchyma appearing hypodense in comparison to the renal parenchyma. The different phases of contrast uptake (Fig. 14) can be differentiated (arterial, corticomedullary, nephrographic, and excretory phase) after iodinated contrast agent administration. The arterial CT phase is reached about 20–30 s after the commencement of intravenous contrast media injection (for renal arteriography, a contrast bolus of 3.5 mL/s is desirable). The corticomedullary CT phase begins about 30–35 s, and it lasts up to 70 s after intravenous contrast agent injection (according to the patient time of circulation) with evidence of high contrast enhancement in the renal cortex. Early opacification of renal veins is also detectable. The renal medulla demonstrates with low contrast. The corticomedullary phase

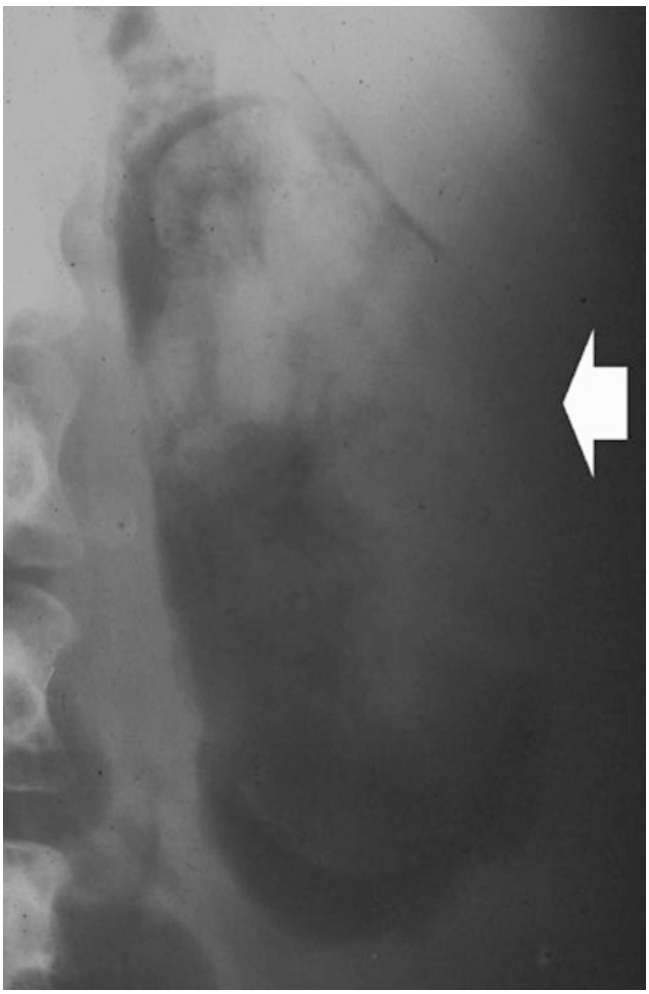

Fig. 8 Plain radiograph. Radiolucency (*arrow*) in the kidney region due to emphysematous pyelonephritis

is suitable for depiction of the normal vascular renal anatomy and alterations of vascular anatomy (aneurysms, arteriovenous malformations, fistulas, etc.). The nephrographic CT phase (80–120 s) shows the renal cortex and medulla with equal enhancement, and it is considered the optimal phase for renal tumor detection (see chapter. "Computed tomography"). The excretory CT phase (more than 180s after intravenous contrast media administration) shows the opacified renal pelvis, ureter, and urinary bladder (complete filling of the urinary bladder with contrast media usually takes about 20 min).

2.4 Magnetic Resonance Imaging

Nowadays, magnetic resonance (MR) imaging produces a image quality of the kidney, which is comparable to CT. MR sequences provide information about tissues, including T1 and T2 relaxation times, lipid or fat content, and enhancement characteristics of tissues. MR imaging provides versatile and unique soft tissue contrast and allows the evaluation of a wide range of urinary tract disorders. This result can be obtained by the intensity of the static magnetic field, gradient quality and intensity, multichannel phased array coils, parallel imaging, fast sequences, and gadolinium-based contrast agents. Currently, 1- to 1.5-T systems are generally used for abdominal imaging, but the advent of 3-T MRI systems brings a twofold increase in the SNR. The increase in SNR can be spent on higher resolution or on even faster imaging. When combined with parallel imaging techniques such as sensitivity encoding (SENSE), the speed of any sequence can be increased by up to a factor of 4 or higher.

Kidneys are optimally represented in the different acquisition planes, transverse, coronal, and sagittal. The coronal

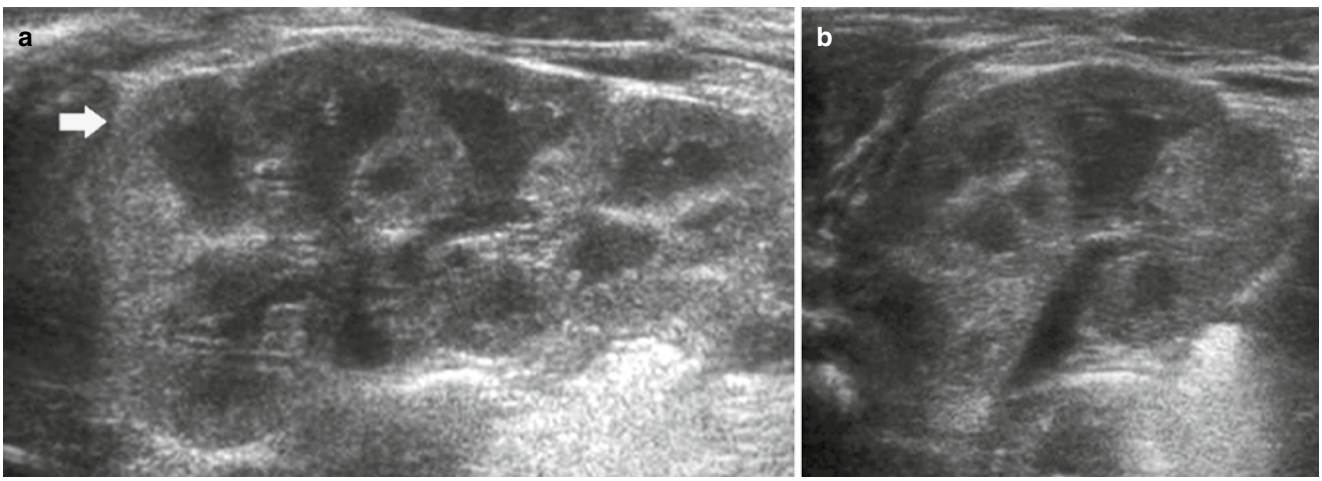

Fig. 9 (**a**, **b**) Ultrasound. Longitudinal (**a**) and transverse scan (**b**). Normal neonatal kidney. The renal cortex (*arrow*) appears hyperechoic with evident hypoechoic medulla. On the upper renal pole, the adrenal gland (**a**) is evident

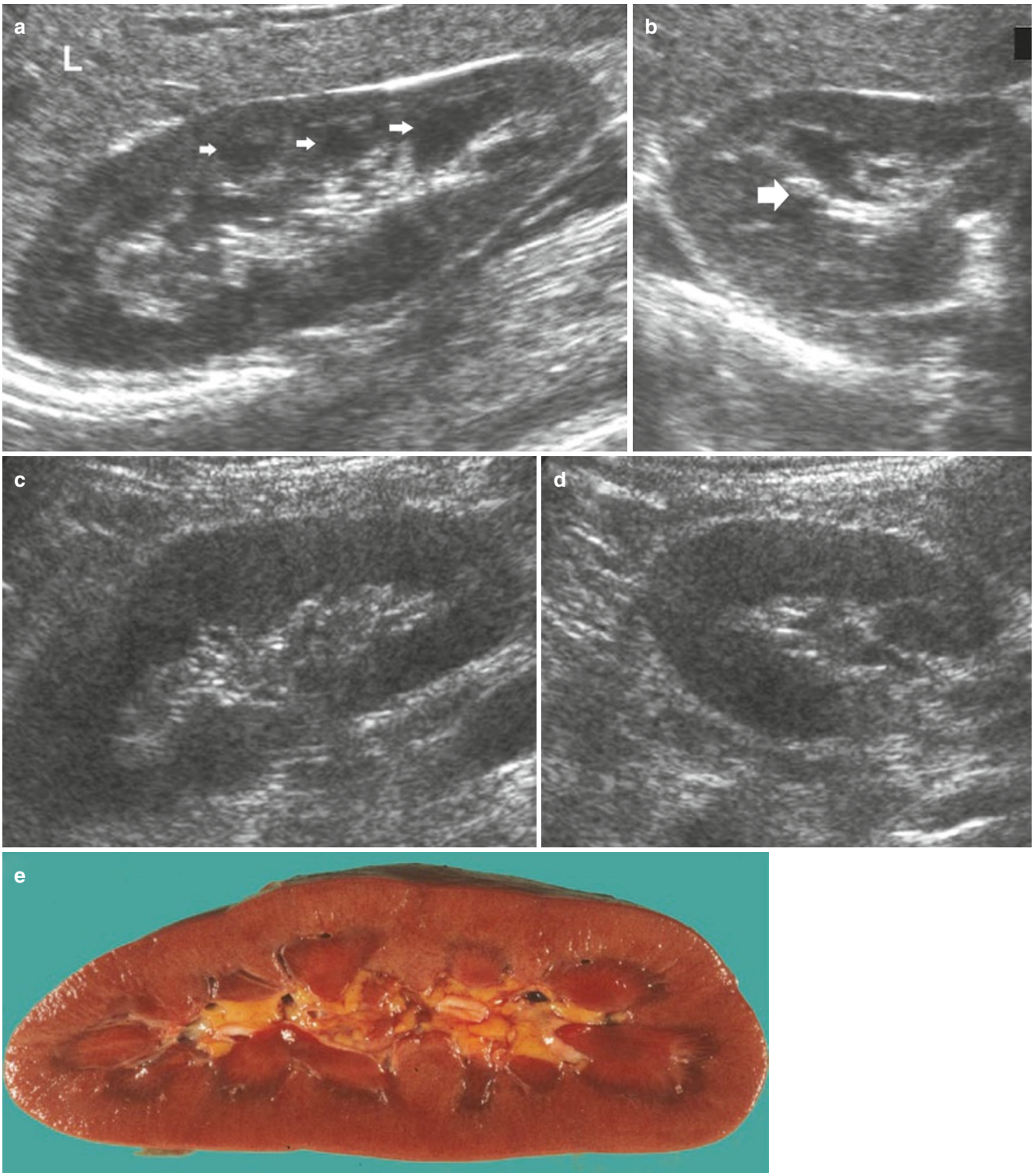

Fig. 10 (**a**–**e**) Normal anatomy of the adult kidney at ultrasound (**a**) Longitudinal scan. On US renal pyramids (*small arrows*) appear hypoechoic in comparison with renal cortex, which appears normally hypoechoic or isoechoic to the adjacent liver parenchyma (L), whereas renal sinus is hyperechoic. (**b**) Transverse scan. The renal pelvis (*large arrow*) appears hyperechoic due to sinusal fat. (**c**, **d**) Longitudinal and transverse scan of a normal kidney with a lower corticomedullary differentiation if compared with the previous example. (**e**) Gross specimen of a cadaveric kidney from a young adult

plane allows the good visualization of both kidneys and of their spatial relation with the adjacent anatomical structures. Usually, the MRI scanning of the kidneys is obtained on the axial and coronal planes with breath-hold sequences including T2-weighted half-Fourier single-shot fast (or turbo) spin echo sequence (SSFSE, GE Healthcare; HASTE, Siemens Medical Solutions), T2-weighted turbo spin echo sequence with fat suppression including spectral presaturation with inversion

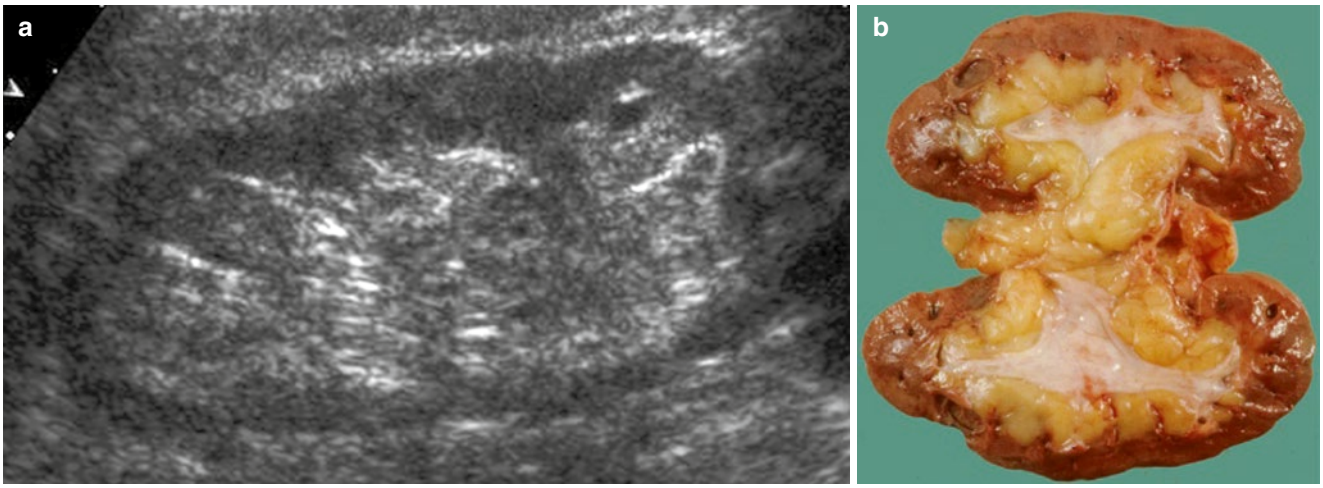

Fig. 11 (**a**) Grayscale ultrasound. Longitudinal scan of a kidney of an 80-year-old patient. Reduction of the renal parenchyma thickness and increase in the renal sinus fat with the evidence of renal contour irregularities due to vascular scars or nephrosclerosis. (**b**) Gross specimen of a cadaveric kidney from an elderly patient

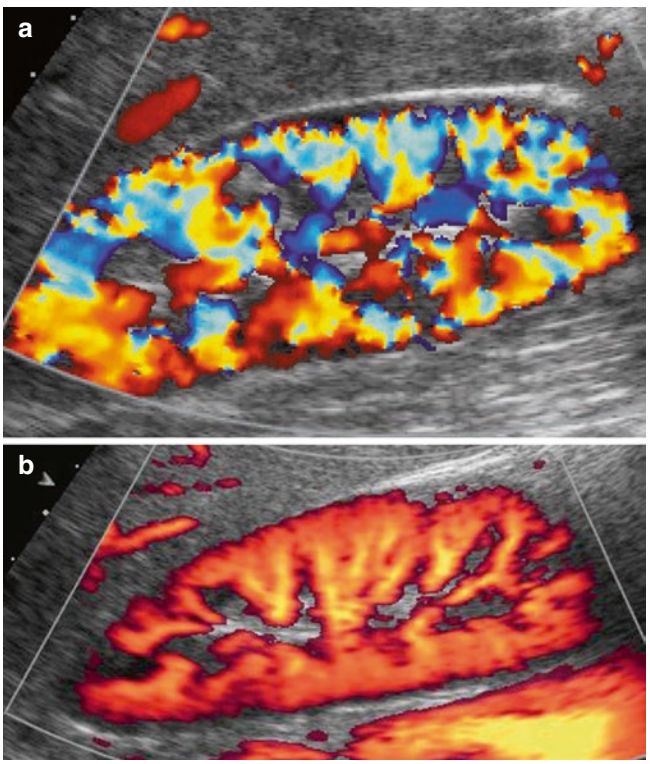

Fig. 12 (**a**, **b**) Normal renal parenchymal vascularization may be effectively revealed by color Doppler (**a**) and power Doppler (**b**), by setting correctly color gain and by using a low-pulse repetition frequency (slow flows setting optimization). Power Doppler is superior to color Doppler in delineating renal parenchymal blood flows, particularly at the renal poles and superficial cortex

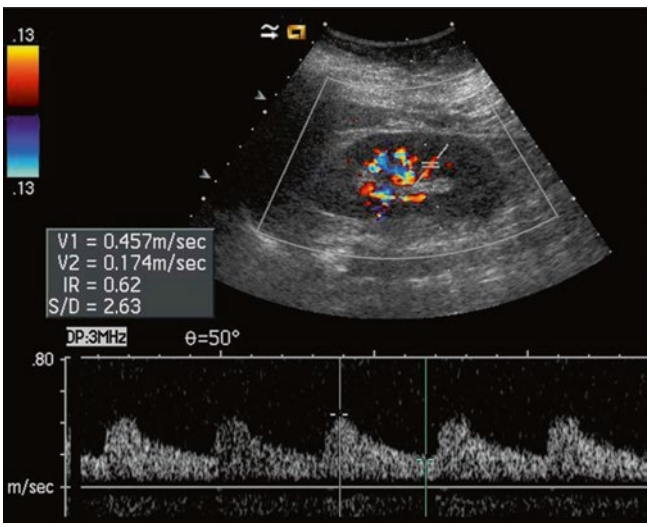

Fig. 13 Intrarenal arteries may be interrogated by pulsed Doppler. In particular, segmental arteries are well suitable for this task. The resistive index may be calculated by measuring the peak systolic and the end-diastolic velocity

recovery (SPIR), or spectral adiabatic inversion recevoery (SPAIR), or short-tau inversion recovery (STIR) sequences, axial dual-echo in-phase and opposed phase gradient echo T1-weighted sequence, and axial or coronal three-dimensional (3D) frequency-selective fat-suppressed fast spoiled gradient echo (SPGR) T1-weighted sequence obtained before and after the intravenous administration of gadolinium-based contrast agents (0.1 mmol/kg of body weight) at a rate of 2 mL/s by using a power injector followed by a 20-mL saline flush. Gadopentetate dimeglumine (Gd-DTPA, Magnevist), gadobenate dimeglumine (Gd-BOPTA, Multihance), gadoxetate disodium (Gd-EOB- DTPA, Primovist), and gadofosveset trisodium (Vasovist) are linear ionic agents, while gadoterate meglumine (Gd-DOTA, Dotarem) is a macrocyclic ionic agent. Gadodiamide (Gd-DTPA-BMA, Omniscan) and gadoversetamide (Gd-DTPA-BMEA, Optimark) are linear nonionic agents, while gadobutrol (Gd-DO3A-butrol, Gadovist) and gadoteridol (Gd-HP-DO3A, Prohance) are macrocyclic nonionic agents. Their effect in T1 and T2 is similar, but since tissue T1 is much higher than T2, the predominant effect at low doses is that of T1 shortening.

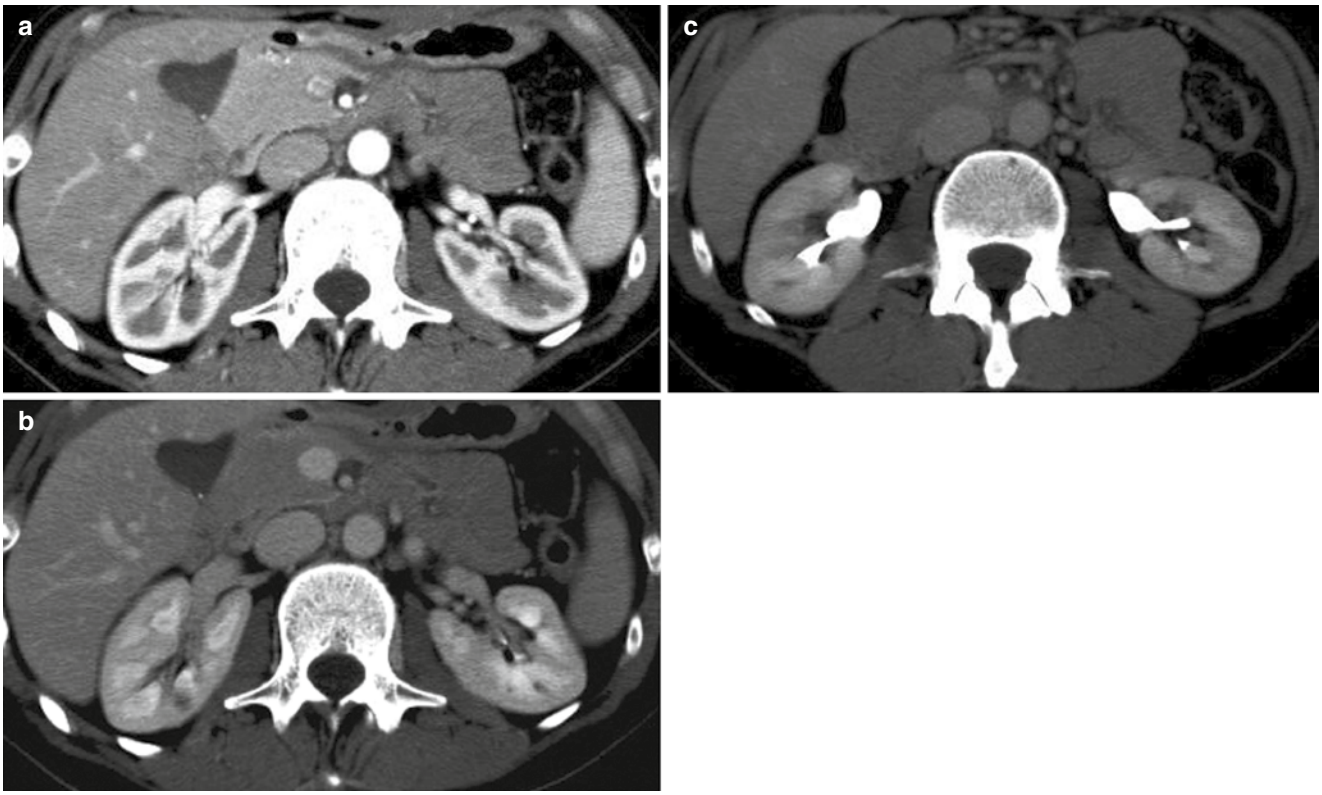

Fig. 14 (**a**–**c**) Normal computed tomography (CT) dynamic phases evident on renal parenchyma after iodinated contrast agent injection. (**a**) The corticomedullary phase begins about 30–35 s after intravenous iodinated contrast agent injection *and shows* high contrast enhancement in the renal cortex. (**b**) The nephrographic CT phase (80–120 s after contrast agent injection) shows renal cortex and medulla with equal enhancement. (**c**) The excretory CT phase (more than 180 s after intravenous contrast media administration) shows the opacified renal pelvis, ureter, and urinary bladder

Respiratory triggering technique is employed in MR imaging to reduce motion artifacts. This technique allows one to use shorter echo train length, more signal averaging, and higher spatial resolution, without being restricted by breath-hold time. This approach can result in a higher SNR in comparison with breath-hold approaches.

The renal parenchyma is composed of two distinct zones, the cortex and medulla. Since the renal cortex presents lower T1 and T2 relaxation times in comparison to the renal medulla, the two zones can be easily distinguished. Anyway, renal corticomedullary image contrast is usually more conspicuous on T1-weighted images. On T1-weighted sequences, the renal cortex appears much brighter than the renal medulla, while on T2-weighted sequences, the renal cortex appears slightly less intense than the renal medulla (Fig. 15). The renal pelvis containing fat appears hyperintense on T1- and T2-weighted sequences. When fat-suppressed MRI sequences are employed, the fat appears hypointense. After the intravenous administration of gadolinium-based contrast agents, the vascular corticomedullary phase begins immediately after the contrast medium reaches the kidneys (Fig. 16). The nephrographic phase begins 60–90 s after contrast administration (Fig. 16). The excretory phase begins 2 min after contrast administration with evidence of contrast excretion in the collecting system.

2.5 Anatomical Variants of Renal Morphology

Renal cortical defects, hypertrophied column of Bertin, dromedary or splenic hump, and persistence of fetal lobation represent frequent anatomical variations of the renal parenchyma which can simulate renal tumors. For this reason, they are also included in the renal pseudotumor category.

- Junctional parenchymal defects. Junctional parenchymal defect results from the incomplete fusion of the two embryonic parenchymatous masses with normal renal sinus fat extending into a groove of renal cortical surface. On US, it appears as a peripheral triangular or round echogenic area located in the anterior surface of upper renal pole or, less frequently, in the posterior surface of the lower renal pole and must be differentiated by renal scars for its continuity with renal sinus. The connection between the intrarenal sinusal fat and the perirenal fat determines a cortical defect, presenting variable evidence between patients, corresponding to a hyperechoic triangular fat on grayscale US (Fig. 17a). Some cortical defects containing fat may mimic a small subcapsular hyperechoic tumor on US. Differential criteria include the evidence of a

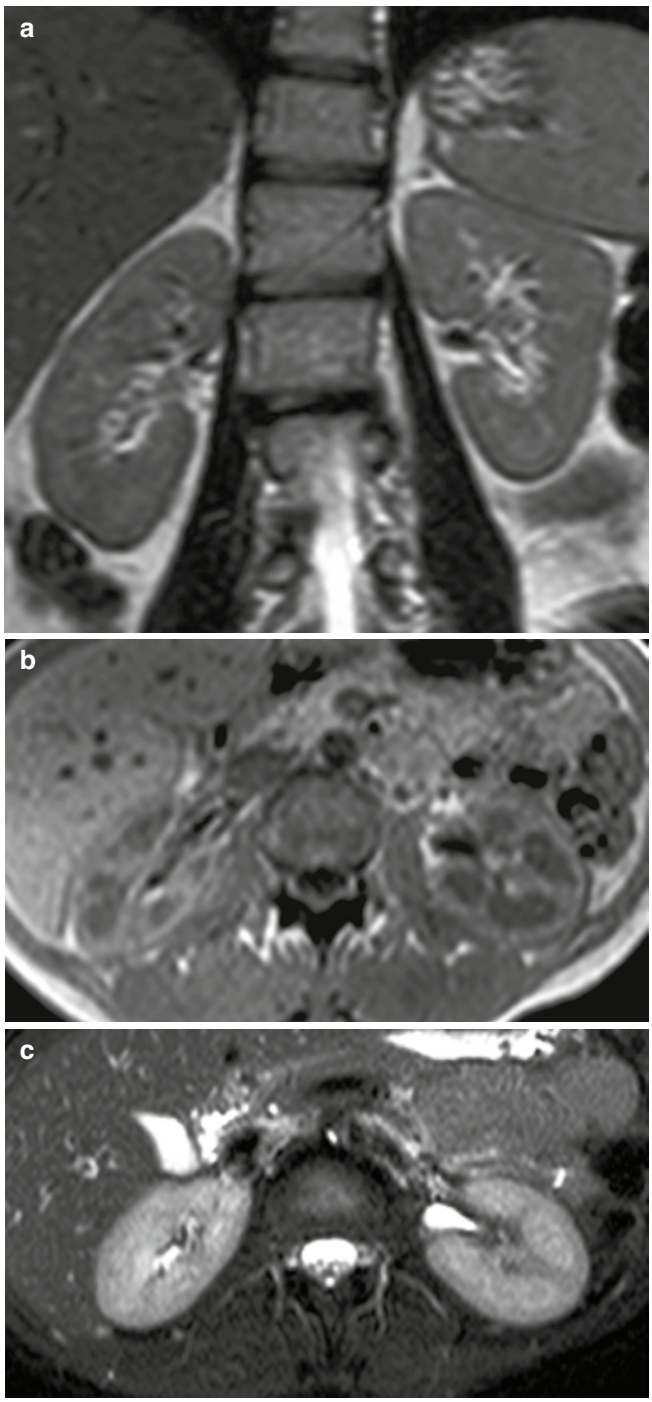

Fig. 15 (**a**–**c**) Normal kidney on magnetic resonance (MR) imaging. On T1-weighted sequences (**a**, **b**) the renal cortex appears much brighter than renal medulla, while on T2-weighted sequences (**c**) the renal cortex appears slightly less intense than renal medulla

junctional hyperechoic line associated with the parenchymal notch (Fig. 17b). The same findings, adjacent to the renal hilus or also posteriorly, may be observed also on contrast-enhanced CT (Fig. 17c) and should be differentiated from traumatic renal fracture based on the absence of perirenal fluid collection (Fanney et al. 1990). Some fatty tissue arising from the renal sinus fat may branch inside the renal parenchyma up to the corticomedullary junction and can mimic a hyperechoic renal tumor within the renal cortex. On the other hand, the intrasinusal growth of a hyperechoic solid tumor may prevent tumor identification while mimicking renal sinus lipomatosis.

- Column of Bertin (focal cortical hyperplasia). Column of Bertin corresponds to normal renal cortex projecting into renal sinus, more frequently at the junction of the upper and middle third of the left kidney. It is visible in 47 % of healthy subjects, and in 18 %, it is bilateral, whereas in 4 % two columns are visible in one kidney (Fig. 18). The US appearance of two or more pyelocalyceal elements is often similar to that of a column of Bertin and consists of a portion of normal renal parenchyma extending from the renal cortex to divide the renal sinus (Fig. 19).
- The hypertrophied column of Bertin represents an invagination of the renal cortex toward the renal sinus. Hypertrophied column of Bertin is considered as renal pseudomass, which can be differentiated from renal tumors by power Doppler US revealing normal parenchymal vessels in the pseudomass (Fig. 20). Hypertrophied column of Bertin is bilateral in 60 % of patients with this variant, which can be identified also on CT (Fig. 21). Differently from the hypertrophied column of Bertin, lobar dysmorphism (Fig. 22) corresponds to a well-defined hypertrophic deep renal parenchyma region appearing isoechoic to the renal cortex and with the evidence of a hypoechoic Malpighi's pyramid (Yeh et al. 1992).
- Dromedary or splenic hump. The dromedary or splenic hump corresponds to a prominent bulge on the superolateral border of the left kidney. The abnormality is best appreciated as an alteration in the left renal contour at the US renal contour at Fig. 23. It is believed to arise secondary to molding of the upper pole of the left kidney by the spleen during development. The normal nature of this finding is confirmed by the uniform thickness of the bulging renal parenchyma over the underlying renal calyces.
- Persistent fetal lobations. The fetal lobation represents a vestige of the lobar development of the kidney, and lobar anatomy is usually lost by the age of 4–5 years. Renal fetal lobations represent single or multiple notches of renal profile. Persistent fetal lobations can be identified in approximately 5 % of adult patients undergoing renal imaging. A key finding in fetal lobation is a normal thickness of the renal parenchyma (≥14 mm) with the indentation occurring so that calyces are centered between indentations and normal vascularization of the renal cortex at color Doppler ultrasound (Fig. 24), which differentiates fetal lobations from renal scars, reflux nephropathy, and papillary necrosis where the renal cortex indentations overlie, respectively, the claviform, calyx, and necrotic renal papilla.

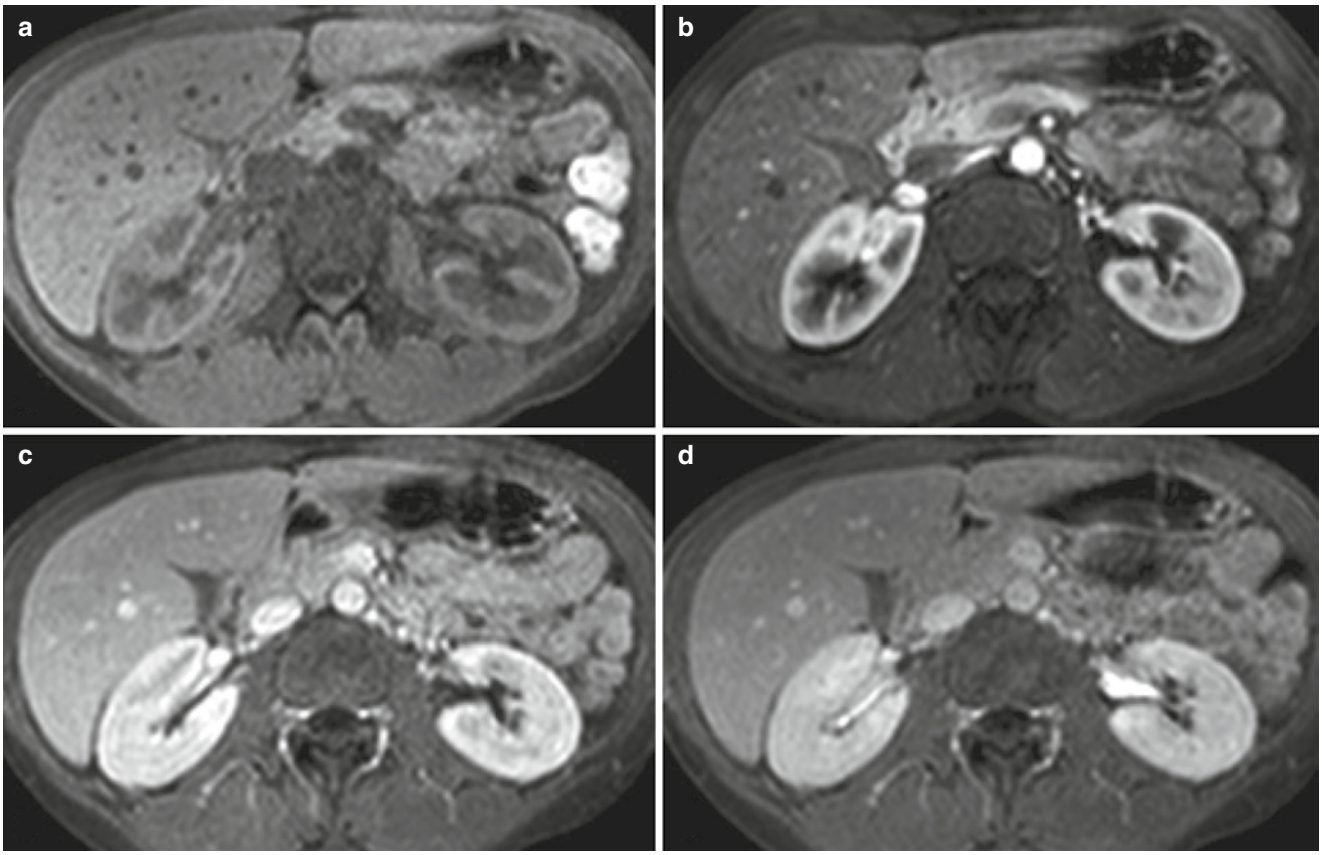

Fig. 16 (**a**–**d**) Normal MR dynamic phases evident on renal parenchyma before (**a**) and after gadolinium-based contrast agent injection (**b**–**d**). (**b**) The corticomedullary phase begins immediately after the contrast medium reaches the kidneys (25–30 s after injection). The nephrographic phase (**c**) begins 60–90 s after contrast administration, which progresses toward the medullary papillae. The excretory phase (**d**) begins 2 min after contrast administration with evidence of contrast excretion in the collecting system

2.6 Congenital Anomalies of the Renal Parenchyma

Congenital anomalies of renal number (congenital absence), location (ectopic, rotational), and fusion are relatively common; 20–30 % of all congenital anomalies are represented by kidney and ureter malformations; and about 1:500 of all newborn infants presents these anomalies (Schedl 2007). These abnormalities may be identified also in utero through prenatal US examination.

- Anomalies of number. Unilateral renal agenesis (Fig. 25) occurs about once in every 5,000 subjects and results from the failure of the ureteric bud to reach the metanephric blastema since it fails to form or degenerates prematurely. This phenomenon appears more frequently in males then in females, and the absence usually regards the left kidney. The infants with this pathology have the following morphological features: an increased distance between the eyes and the presence of epicanthic folds, a low position of the ears, a broad and flat nose, a receding chin, and defects of the limb. Fetal electrolyte balance is kept by exchange through the placental membrane. Renal unilateral or bilateral agenesis probably has multifactorial etiology.
- Unilateral absence of a kidney usually causes no symptoms and is not discovered during infancy because the other kidney undergoes compensatory hypertrophy and performs the function of the absent kidney. Unilateral agenesis is often identified during investigations in other congenital anomalies, or because some urinary tract symptoms appear (Twining 1994). In 20 % of the male individuals with renal agenesis, there is an absence of the ipsilateral epididymis, vas deferens, or seminal vesicle or presence of an associated ipsilateral seminal vesicle cyst. In 70 % of women with unilateral renal agenesis, associated genital anomalies are present.
- Bilateral renal agenesis is rare (1/3,000–4,000 deliveries live births) and is incompatible with life. Most infants with bilateral renal agenesis die after birth if the death has not occurred in the fetal life. Associated ureteral abnormalities are universally present including absence of the ipsilateral ureter or presence of a blind-ending ureteral stump. Bilateral agenesis is often associated with oligohydramnios because urine is not excreted into the amniotic fluid (Peipert and Donnenfeld 1991). If the amniotic fluid volume is abnormally decreased, in the absence of other causes, such as rupture of fetal

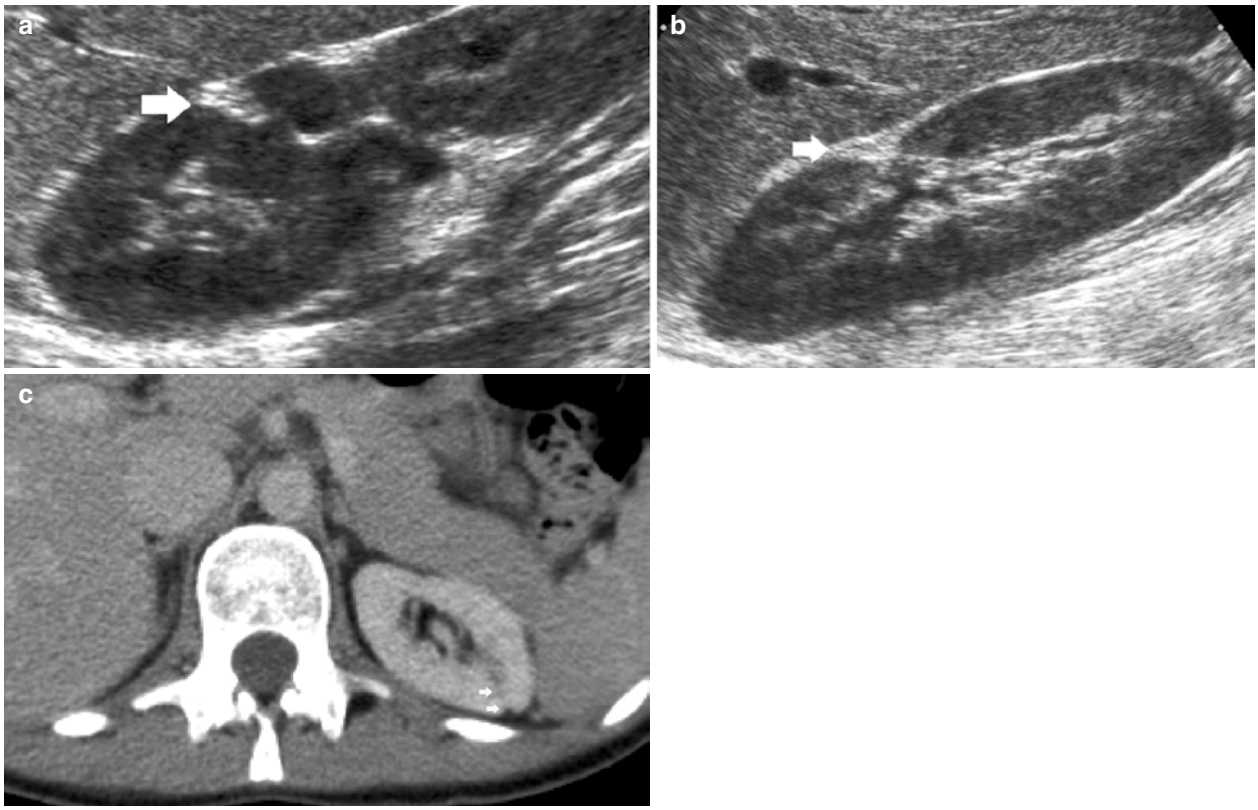

Fig. 17 (**a**, **b**) Renal cortical defect. Ultrasound. Longitudinal scan. (**a**) The hyperechoic triangular fat (*arrow*) corresponding to a cortical defect through which there is a connection between the intrarenal sinusal and perirenal fat. (**b**) Evidence of a junctional parenchymal hyperechoic line associated with the parenchymal notch. (**c**) Contrast-enhanced CT, nephrographic phase. Evidence of a posterior parenchymal defect (*arrows*) associated with the parenchymal notch

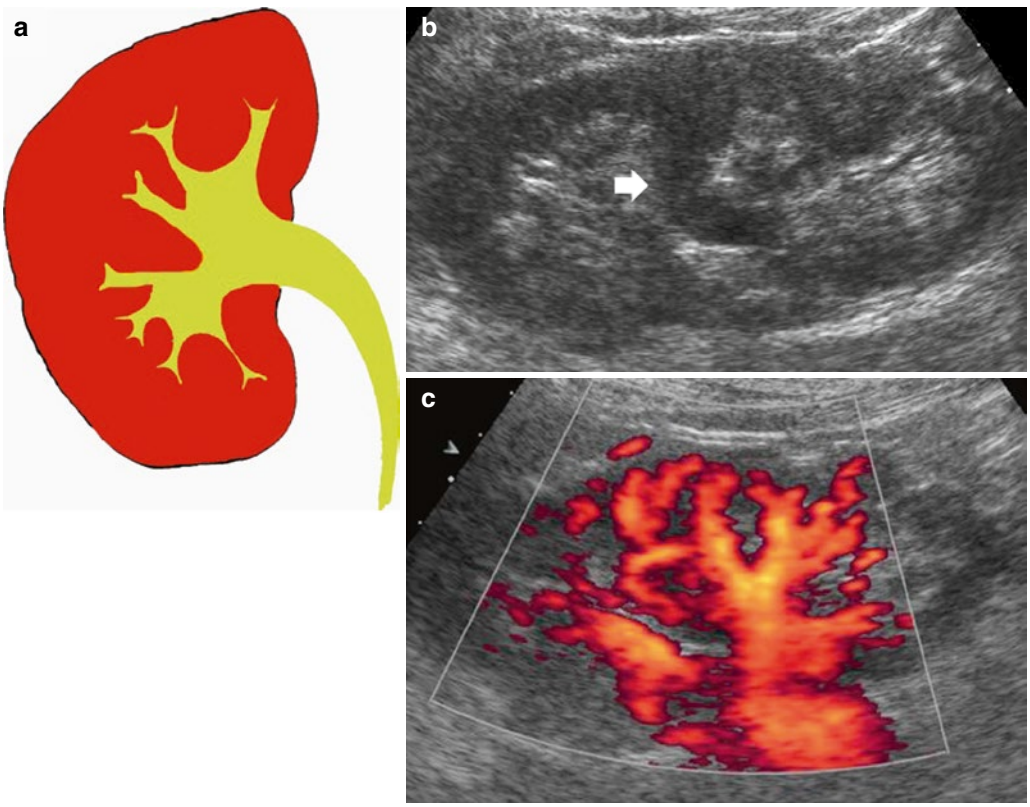

Fig. 18 (**a**–**c**) Column of Bertin. (**a**) Scheme. (**b**) Longitudinal scan. Mesorenal column (*arrow*). (**c**) Power Doppler ultrasound. The mesorenal column presents a regular vascularization

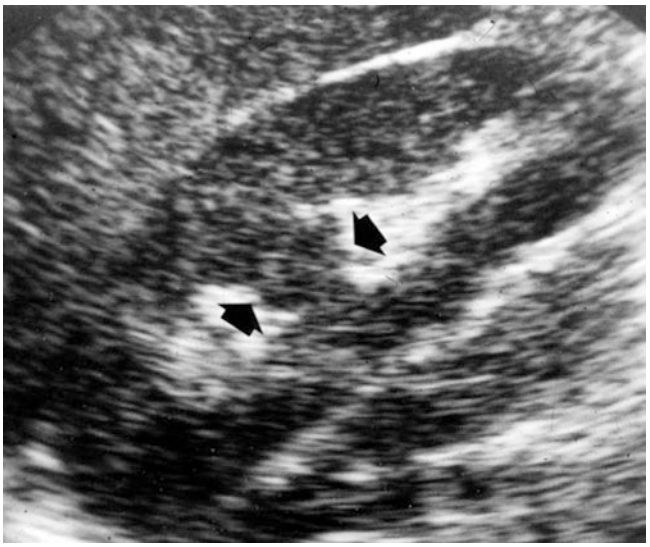

Fig. 19 Duplication of the renal pelvis. Longitudinal scan. A portion of normal renal parenchyma (*arrows*) extends from the renal cortex to divide the renal sinus

membranes, it must induce to investigate about renal excretory system anomalies (Mahony 1994).

- Supernumerary kidneys are very rare and result from the formation of two ureteral buds on one side. Usually, the supernumerary kidney occurs on the left side inferior to the normal kidney and is hypoplastic. Supernumerary kidneys may be drained by a bifid ureter draining the second ipsilateral kidney or by an independent ureter.
- Anomalies of rotation. The fetal kidneys undergo a 90° rotation around the longitudinal axis during their ascent from the pelvis before they reach their final position by the end of the eighth week of fetal life. Malrotation and nonrotation of the kidneys are common anomalies. These anomalies consist in a normal position of the kidney in the flank region, but the long axis is rotated due to the absent 90° rotation of the kidney during proximal migration with the entire process completed by the end of the ninth week (Fig. 26). Malrotation is most commonly associated with an ectopic (Fig. 27) or fused kidney, but may also occur in

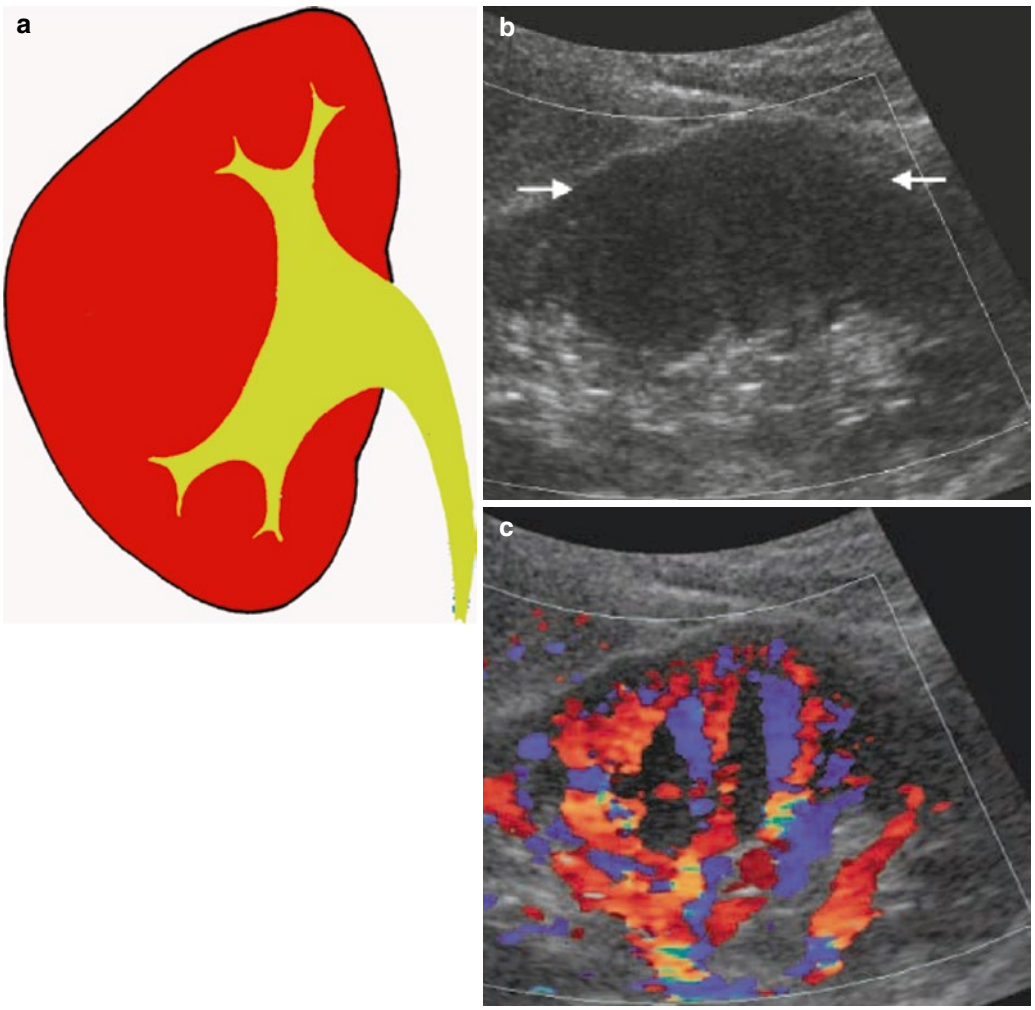

Fig. 20 (**a**) Hypertrophied column of Bertin. (**b**) Grayscale ultrasound. Renal pseudomass (*arrows*) due to hypertrophied column of Bertin; (**c**) color Doppler ultrasound which reveals normal parenchymal vessels in the pseudomass

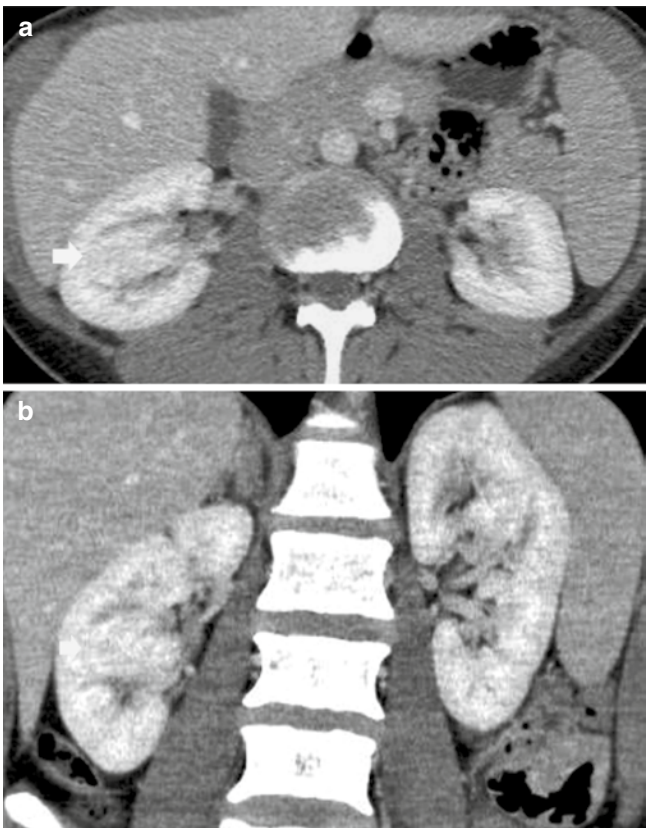

Fig. 21 (**a**, **b**) Renal pseudomass due to hypertrophied column of Bertin. (**a**) Contrast-enhanced *CT*, nephrographic phase. Transverse plane (**a**) and coronal reformation (**b**). Hypertrophied column of Bertin (*arrow*)

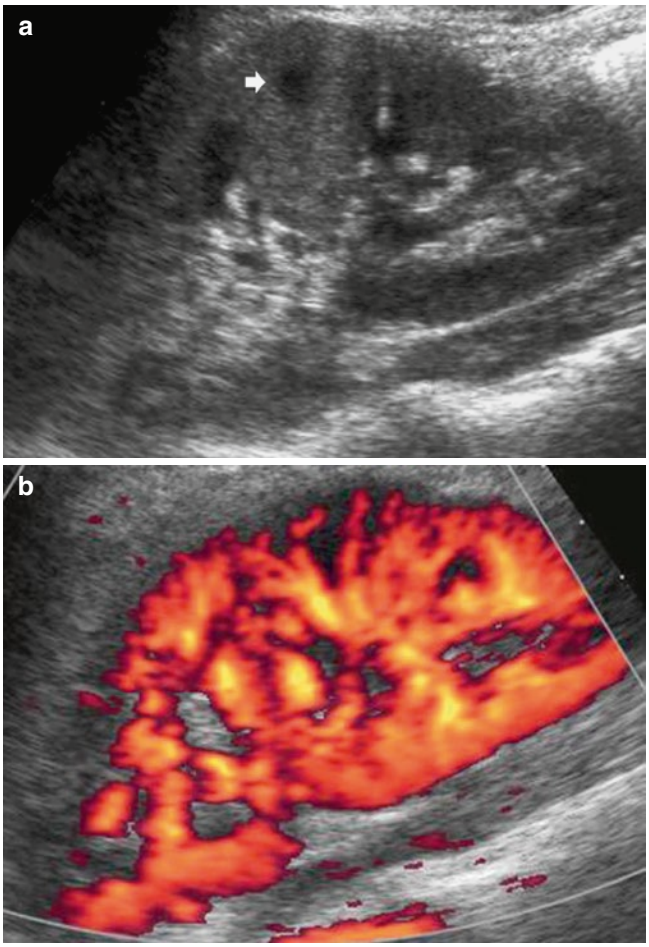

Fig. 22 (**a**, **b**) Lobar dysmorphism. (**a**) Grayscale ultrasound. A well-defined mass arising from the deep renal parenchyma and isoechoic to the renal cortex projects inside the renal sinus with the evidence of a hypoechoic Malpighi's pyramid (*arrow*). (**b**) Power Doppler ultrasound which reveals normal parenchymal vessels in the pseudomass

kidneys that undergo complete ascent and may be unilateral or bilateral. Incomplete rotation or nonrotation represents the most common types of rotation anomalies. In this condition, the renal pelvis is in the anterior position or in an intermediate position between the anterior and the normal medial position. In reversed rotation the renal pelvis rotates laterally, and the renal vessels are twisted anteriorly around the kidney. In the hyperrotation the kidneys rotate more than 180° but less than 360°, the renal pelvis faces laterally, and the renal vessels are carried posteriorly to the kidney. On intravenous excretory urography (Fig. 26) or computed tomography urography (CTU) (Fig. 27), renal malrotation is identified as the renal pelvis, instead of arising from the kidney medially, appears to arise centrally. The renal calyces appear often distorted, even without any association with urinary tract obstruction. Some calyces are located medially to the renal pelvis and seem to arise on either side of the pelvis, a hallmark of rotational anomalies. Anomalies of rotation may produce partial ureteropelvic junction obstruction.

- Renal ectopia. The normal location of kidney is from the first and third lumbar vertebrae. Renal ectopia corresponds to the abnormal location of the kidney due to developmental anomaly due to the arrest or exaggeration of normal caudal-to-cranial ascent. Unilateral is the most common even though it may involve both kidneys or solitary kidneys. The autopsy incidence of renal ectopia is about 5.9 % (Barakat and Drougas 1991). An ectopic kidney undergoes an incomplete rotation around its axis and is malrotated, and the renal pelvis faces anteriorly. Ectopic kidneys vary in size and tend to be dysplastic and are often associated with contralateral renal anomalies including malrotation or ectopia of the contralateral kidney. Anomalous blood supply to the kidney, deriving from adjacent vessels, is always present in renal ectopia. In renal ectopia, the ureter length (Fig. 27) and the renal artery length (Fig. 28) are appropriate for the kidney position. The renal collecting system does not drain as readily as in the normal kidney. This results in urinary stasis and in an increased prevalence of stone formation.

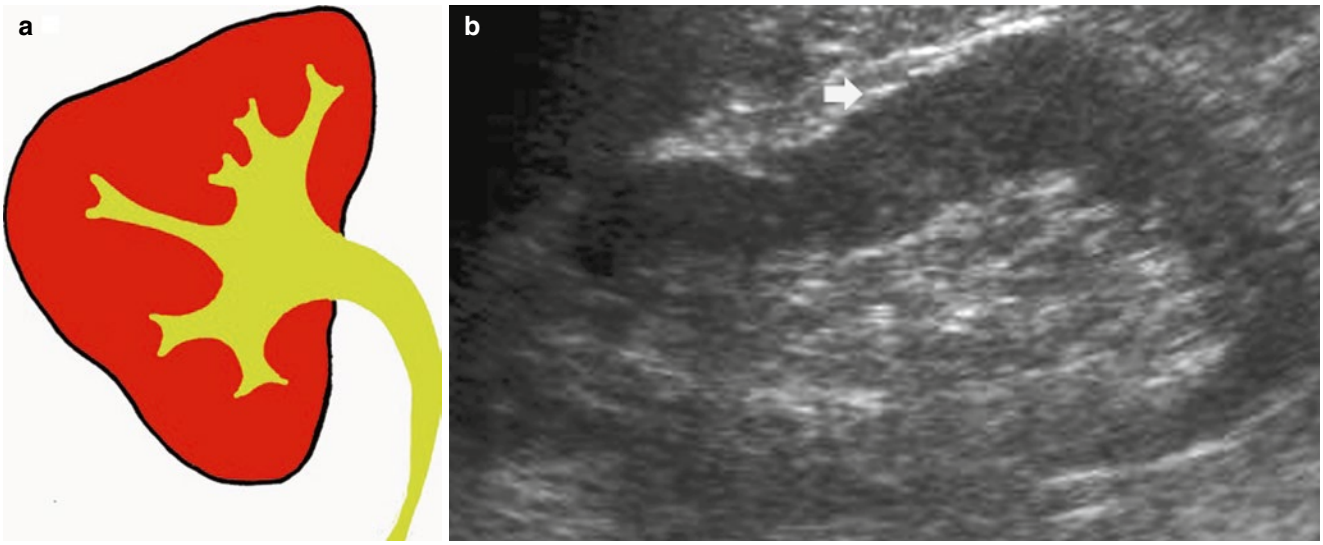

Fig. 23 (**a**, **b**) Dromedary or splenic hump. (**a**) Renal pseudomass due to dromedary hump of the left kidney. (**b**) Grayscale ultrasound. Longitudinal scan. Prominent bulge on the superolateral border of the left kidney (*arrow*)

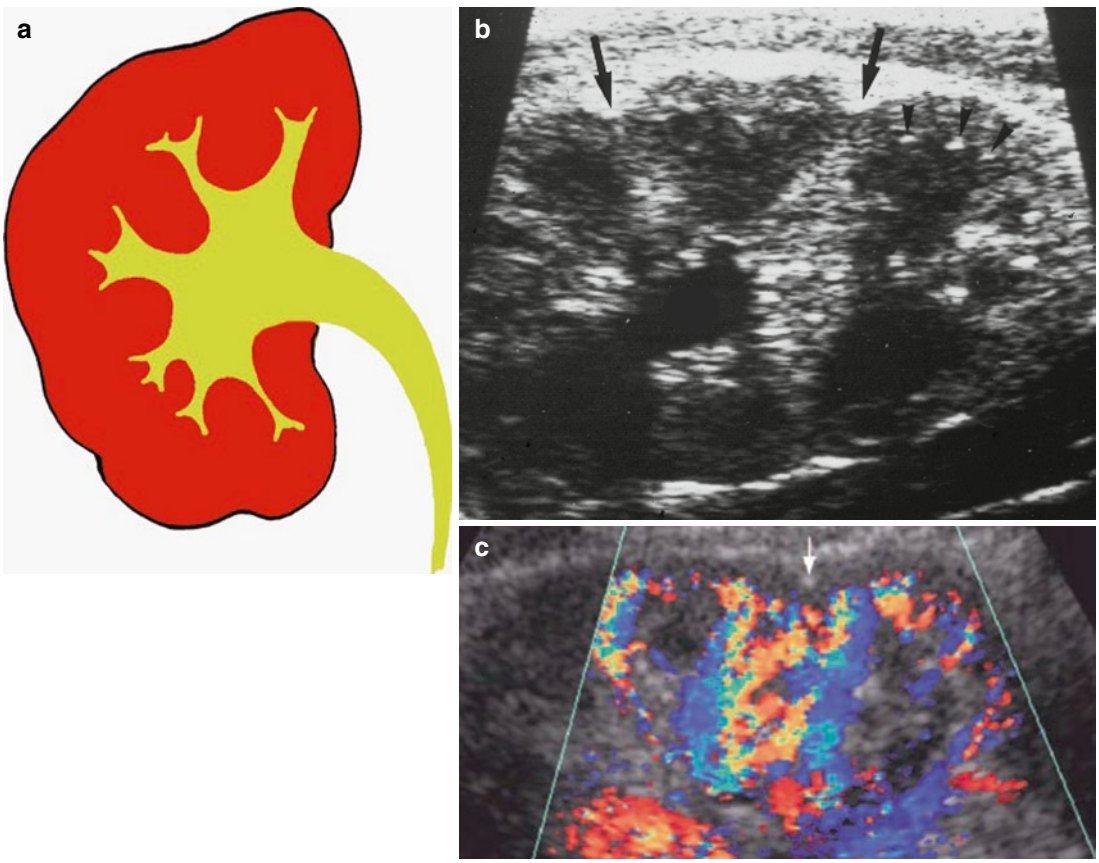

Fig. 24 (**a**) Renal fetal lobations. (**b**) Ultrasound, longitudinal scan. Two notches (*arrows*) on renal profile are visualized, with no reduction of renal cortical thickness with respect to renal medulla (*arrowheads*). (**c**) Normal parenchymal vascularization is visualized by color Doppler in the renal parenchyma between the notch (*arrow*)

Fig. 25 Contrast-enhanced CT. Nephrographic phase. Agenesia of the right kidney, with the right renal region occupied by the bowel loops. The left kidney presents malrotation

Fig. 27 Computed tomography urography (CTU). Color-coded three-dimensional (3D) volume rendering. Malrotation and ectopia of the right kidney which appears malrotated and with a short ureter. The right ureter length appears appropriate considering the kidney position

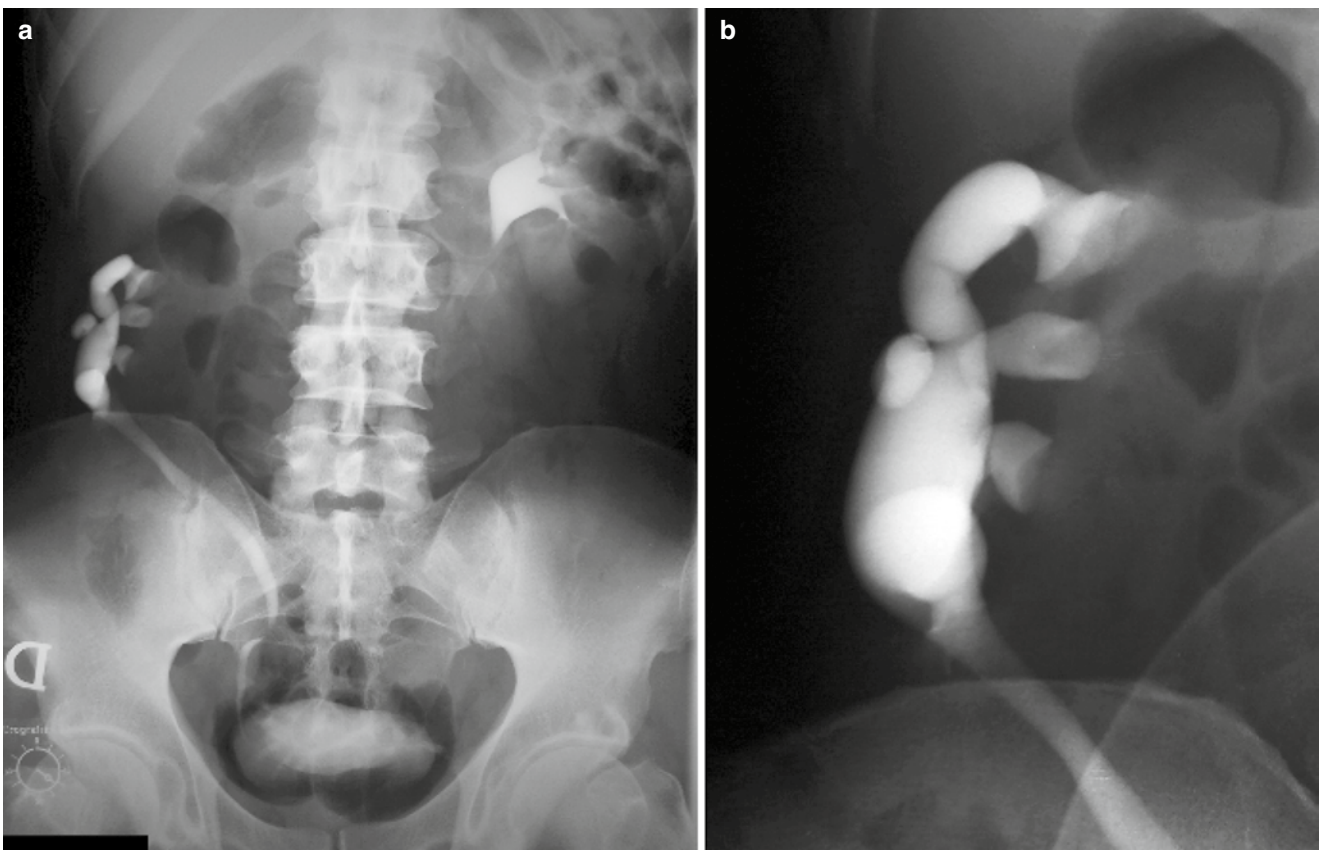

Fig. 26 (**a**, **b**) Intravenous excretory urography. Malrotation of the right kidney. The right renal pelvis appears to arise centrally instead of arising from the kidney medially. Some calyces are located medially to the renal pelvis and seem to arise on either side of the pelvis

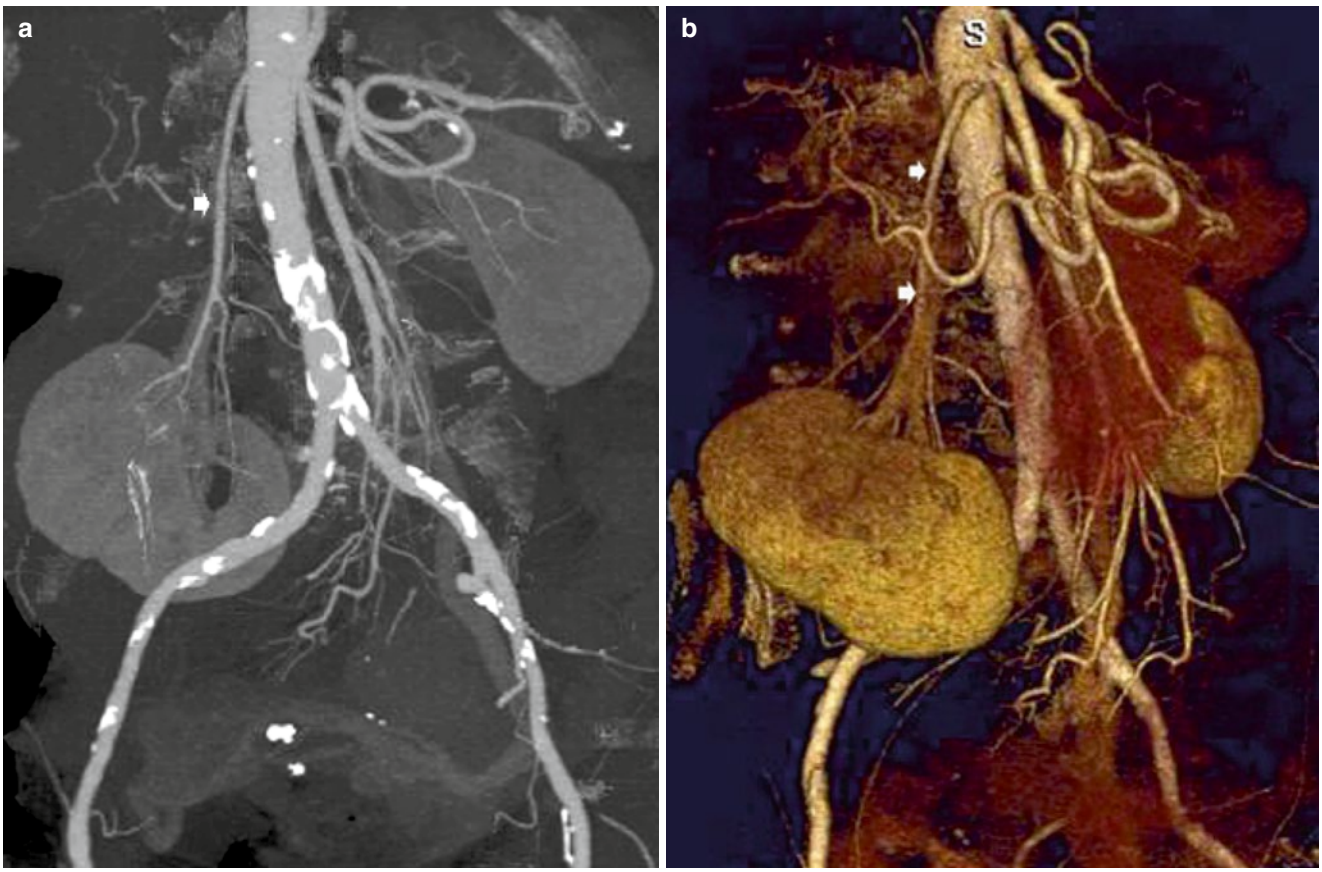

Fig. 28 (**a**, **b**) Pelvic kidney. (**a**) Computed tomography angiography (CTA) with CTU. 3D volume rendering images maximum intensity projection (MIP) reconstruction, and (**b**) color-coded volume rendering. The renal artery (*arrows*) presents a length appropriate for the kidney position

Ipsilateral renal ectopia corresponds to an ectopic kidney on the same side of the body as orifice of its attendant ureter. (*a*) Cranial (superior) renal ectopia corresponds to the ectopic kidney lying above the normal position (intrathoracic kidney or below the eventrated diaphragm). (*b*) Caudal (simple renal ectopia) corresponds to a kidney lying below the normal position (abdominal if lying above the iliac crest, iliac if lying in the iliac fossa, or pelvic kidney if located in the true pelvis).

In the case of ectopic pelvic kidney (1/1,000 live births), the vascular supply, beside from the renal arteries, could come also from branches of the lower abdominal aorta or of the iliac arteries. Pelvic kidneys are usually relatively small and irregular in shape, have a variable degree of rotation, and may fuse to form a discoid or pancake kidney. Pelvic kidneys are associated with an increased incidence of ureteropelvic junction obstruction. In renal ptosis (1/1,000 live births), known also as floating kidney, the kidney descends more than 2 vertebral bodies (or >5 cm) during a position change from supine to upright. The length of the ureter, which appears tortuous, and the length of the renal artery are not appropriate to the position of the kidney, and this represents an important point in the differentiation from renal pelvic ectopia. The principal differential diagnoses are renal allograft (transplanted kidney in iliac fossa), renal autotransplantation (surgical repositioning patient's own kidney), horseshoe kidney, and acquired renal displacement due to large liver, spleen, or any retroperitoneal tumor. Other pelvic kidneys are close to each other and fuse to originate a discoid or pancake kidney. These kidneys receive the blood from internal or external iliac arteries and/or aorta.

Crossed renal ectopia (Fig. 29) corresponds to an ectopic kidney located on the opposite side of midline from its ureteral surface. In this anatomical anomaly, most commonly kidneys may fuse or may maintain a separate position (10–15 % of cases). The kidneys fuse while they are in the pelvis, and when a kidney ascends to its final position, it brings the other one with it. Crossed fused ectopia is an uncommon congenital anomaly in which one kidney crosses the midline and fuses with the opposite kidney. Several variants of crossed fused renal ectopia exist including superior (the kidney crossing the midline lies superiorly to the resident kidney), sigmoid (or S shaped, the crossed kidney lies inferiorly), unilateral (lump kidney when both kidneys completely fused, L shaped when the crossed kidney is inferior and transverse, disc when each kidney is fused to other along the medial

Fig. 29 Crossed renal ectopia. The right kidney is ectopic, and its upper pole is fused with the lower pole of the contralateral kidney

concave border), or inferior (crossed kidney inferior to the resident and with its upper pole fused to lower pole of resident kidney) (Federle et al. 2004).

Crossed fused ectopic kidney is often associated with aberrant ureteral and vascular anatomy with an increased incidence of reflux, obstruction, and stones as well as trauma and iatrogenic injury.

- Horseshoe kidney. The horseshoe kidney represents a congenital anomaly of the kidney where two kidneys are fused by the isthmus at the lower pole. The horseshoe kidney represents the prototype of abnormalities of renal fusion and a male-to-female predominance (2:1) and is the most common renal anatomical anomaly (1/400 live births). Wilms' tumors are two to eight times more frequent in children with horseshoe kidney than in the general population. If Turner syndrome is present, about 7 % of this people have horseshoe kidneys (Behrman et al. 1996). The horseshoe kidney (Fig. 30) develops after a midline connection between the two metanephric mass tissues. The midline connection, or isthmus, may consist of a fibrotic band or functional renal parenchyma. The horseshoe kidney is usually positioned low in the abdomen as a result of the arrest of normal ascent, which is hampered by the origin of the inferior mesenteric artery. The horseshoe kidney is related to an increased incidence of vascular anomalies, ureteropelvic junction obstruction, duplication anomalies, stone formation, and urinary tract infections.

3 Normal Radiological Anatomy of Renal Vessels and Anatomical Variants

Traditionally, the evaluation of renal vascular abnormalities was performed with conventional angiography. Cross-sectional imaging now plays an important and increasing role in evaluating renal vascular abnormalities in both the native and transplant kidneys.

The renal arteries originate directly from the aorta and course posteriorly and laterally to the renal parenchyma. Single renal arteries to each kidney most commonly arise from the abdominal aorta near the L1–L2 level. The right renal artery usually originates from the anterolateral aspect of the aorta, while the left renal artery usually originates from a posterolateral aspect of the aorta. The renal arteries assume a dorsoinferolateral course until they enter the kidney at the renal hilum. Normally, each kidney is supplied by a single renal artery and a single renal vein, arising from the abdominal aorta and the inferior vena cava, respectively. These vessels typically originate off the aorta, at the level of L1–L2, below the takeoff of the superior mesenteric artery (SMA), with the vein anterior to the artery. Both vessels then course anterior to the renal pelvis before entering the medial aspect of the renal hilum. The right renal artery typically demonstrates a long downward course to the relatively inferior right kidney, traversing behind the inferior vena cava. Conversely, the left renal artery, which arises below the right renal artery and has a more horizontal orientation, has a rather direct upward course to the more superiorly positioned left kidney. In addition, both renal arteries course in a slightly posterior direction because of the position of the kidneys. Depiction of the relatively avascular plane between the anterior and posterior arterial divisions of the kidney is of importance to the surgeon, because it allows for a clean incision toward the renal pelvis at the time of surgery. This is usually located one third of the distance between the posterior and anterior surfaces of the kidney. A similar avascular transverse plane exists between the posterior renal segment and the polar renal segments.

The renal venous anatomy parallels the arterial anatomy. The renal cortex is drained sequentially by the interlobular veins, arcuate veins, interlobar veins, and lobar veins. The lobar veins join to form the main renal vein. The renal vein usually lies anterior to the renal artery at the renal hilum. The left renal vein is longer than the right renal vein. The left renal vein averages 6–10 cm in length and will normally course anteriorly between the SMA and the aorta before emptying into the medial aspect of the inferior vena cava. The right renal vein averages 2–4 cm in length and joins the lateral aspect of

Fig. 30 (**a**–**c**) Horseshoe kidney with the two kidneys fused by isthmus at the lower pole. (**a**) CTU; (**b**, **c**) 3D maximum intensity projection with evidence of the horseshoe kidney (*arrow*)

inferior vena cava. Unlike the right renal vein, the left renal vein receives several tributaries before joining the inferior vena cava. It receives the left adrenal vein superiorly, the left gonadal vein inferiorly, and a lumbar vein posteriorly.

3.1 Grayscale and Doppler Ultrasound

The principal renal arteries may be clearly identified at their origin from the abdominal aorta (Fig. 31). Doppler

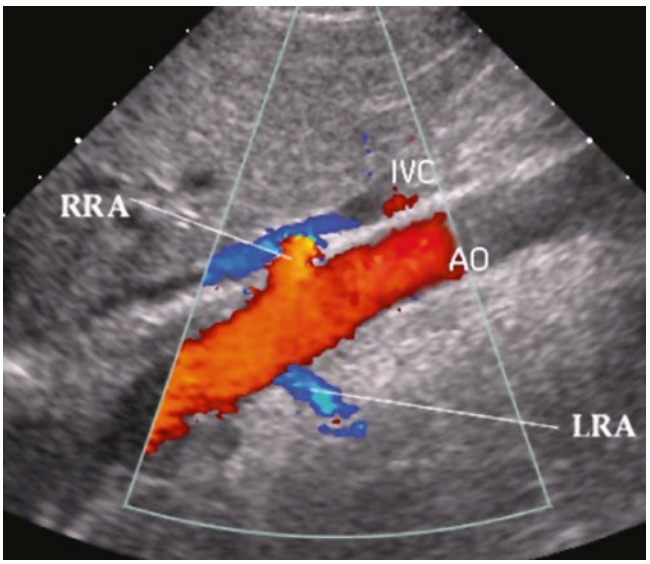

Fig. 31 Color Doppler ultrasound longitudinal scan. Normal anatomy of the main renal arteries at the origin from the aorta (*AO* aorta, *IVC* inferior vena cava, *RRA* right renal artery, *LRA* left renal artery)

US evaluation of the main renal arteries is highly related to operator experience, especially in situations such as patient obesity, intervening bowel gas, or deep renal arteries location. The principal renal artery is often difficult to be detected at baseline color Doppler US for the perpendicular position to the ultrasound beam direction and for the depth position. Since accessory renal arteries occur in up to 25 % of patients and may contain stenoses determining renovascular hypertension (Grant and Melany 2001), the visibility of these vessels is very important for a complete diagnostic work-up of the patient. The velocitometric analysis of Doppler trace derived from renal arteries is of primary importance to identify renal artery stenosis. Direct Doppler criteria have been proposed for the detection of renal arterial stenosis, including an increased peak systolic velocity (>150–180 cm/s) and end-diastolic velocity at the level of the stenosis (Correas et al. 1999; Grant and Melany 2001), poststenotic flow disturbance resulting in spectral broadening and reversed flow (Correas et al. 1999), increased ratio (≥3.5) of peak systolic velocity in renal artery and aorta (renal–aortic ratio), and the presence of turbulence within the renal artery (Desberg et al. 1990; Helenon et al. 1995). Although this technique is easy to perform, its accuracy is questionable because the lack of an early systolic peak has a low sensitivity for moderate stenoses and the waveform is dependent on the maintenance of vessel compliance, which limits its effectiveness in elderly patients and patients with atherosclerosis (Bude et al. 1994; Bude and Rubin 1995).

3.2 CT Angiography

Computed tomography angiography (CTA) is now considered a fundamental technique in the assessment of the renal arteries (Fig. 32). 3D volume-rendered images provides a fast, noninvasive modality for the evaluation of the renal vessels. CTA can reliably and accurately depict the renal arteries and veins as conventional angiography in the assessment of most vascular abnormalities. The number, size, course, and relationship of the renal vasculature are easily appreciated utilizing real-time interactive editing. The CTA protocol requests a double scout view and the following scanning parameters for 64-row CT: beam collimation, 0.5 mm × 64; normalized pitch, 0.828; revolution time, 0.4 s; and bolus tracking. Of the many 3D reconstruction algorithms available for performing CTA, volume rendering has emerged as the rendering technique of choice. With volume rendering, the user can actively interact with the dataset, editing and modifying the position, orientation, opacity, and brightness of the image in real time. For CTA, volume rendering is commonly preformed with a window/level transfer function that results in high-density material (e.g., enhanced vessels or vascular calcifications) to appear bright and opaque, while less-dense structures appear dim and translucent. Overlying structures are easily removed with an interactive clip-plane, and the vessels of interest are easily rotated into the best orientation for depiction of the region of interest. For evaluation of the renal hilum, axial, coronal, and sagittal views are often used in conjunction with optimal evaluation of the number, caliber, and course of the renal arteries and veins. Perspective rendering allows the user to view the dataset from within the vessel, producing angioscopic views which are also helpful for identifying a vascular orifice and stenosis. Volume-rendered CTA can very quickly and accurately determine the location and course of the renal vascular anatomy. Angioscopic views provide additional information on the renal vascular anatomy and compliment conventional volume-rendered images. Typically, arterial branches can be confidently identified to at least the segmental level. Limitation for detection occurs with vessels smaller than 2 mm in size. Sensitivity for the demonstration and location of main renal arteries, however, approaches 100 %. Surgical and CT findings correlate in over 95 % of cases. The renal venous anatomy is also well demonstrated with CTA and is especially important to document for patients undergoing evaluation for laparoscopic donor nephrectomy. The left renal anatomy is especially critical, and this is the preferred side for donation. Tributaries into the left renal vein, especially posterior lumbar branches, are confidently displayed and are of potential surgical importance if noted to be enlarged. MIP represents the other common reconstruction algorithm commonly employed when evaluating the renal vasculature. The MIP technique evaluates each voxel from

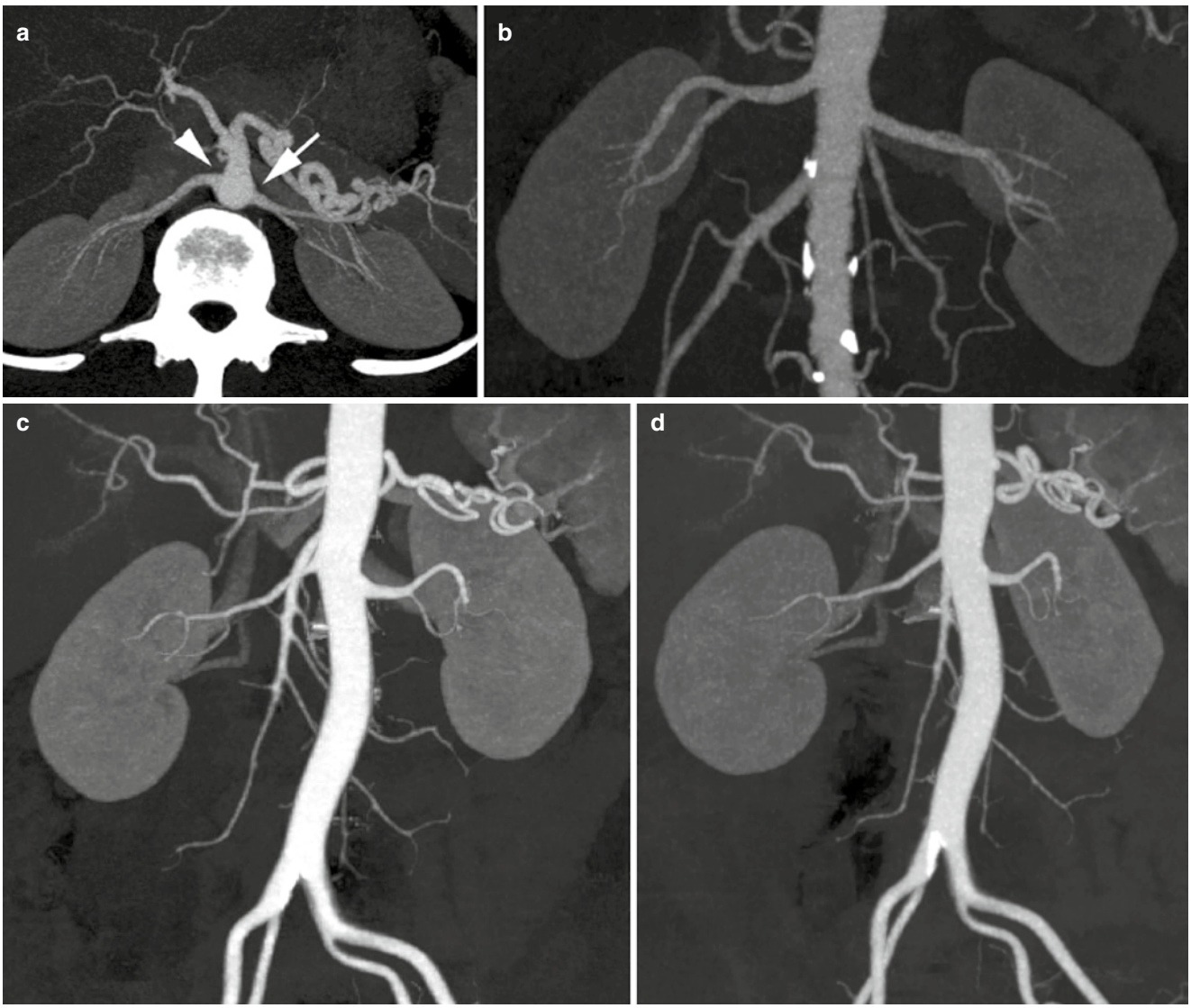

Fig. 32 (**a**–**d**) Normal anatomy of the renal arteries (*arrows*) as seen on contrast-enhanced angio-CT. Maximum intensity projection. (**a**) Transverse plane. Maximum intensity projection reconstruction shows the posterolateral origin of the left renal artery (*arrow*) and anterolateral origin of the right (*arrowhead*) (Courtesy of Dr. Therese M. Weber, Department of Radiology, University of Alabama at Birmingham.) (**b**) Coronal reformation of renal arteries and abdominal aorta. (**c**, **d**) Rotation of the 3D data set allows the accurate assessment of the origin of both renal arteries

the viewers' eye through the dataset and selects the maximal voxel value as the value of the corresponding displayed pixel. The image produced lacks depth orientation, but a 3D effect can be produced with rotational viewing of multiple projections. MIP images can provide useful information regarding atherosclerotic burden, vascular stents, and vascular stenoses and are often reconstructed and interpreted in conjunction with volume-rendered images.

3.3 MR Angiography

Magnetic resonance arteriography (MRA) provides an alternative to intra-arterial digital subtraction angiography in the detection and staging of structural abnormalities of the aorta and its branches. It uses no ionizing radiation and does not require arterial access. A number of imaging techniques have been developed to visualize the circulation using MR imaging, including "black blood" techniques, two-dimensional (2D) and 3D time of flight (TOF) methods, phase-contrast (PC) techniques, and 3D contrast-enhanced methods using gadolinium compounds and other paramagnetic or super paramagnetic agents. The most commonly used are 2D-TOF MRA and 3D contrast-enhanced methods (Grist 2000). For the evaluation of renal artery stenosis, both 2D-TOF MRA and PC methods are generally limited to the assessment of the proximal portion of the renal artery because the long acquisition times preclude breath-hold imaging. 3D

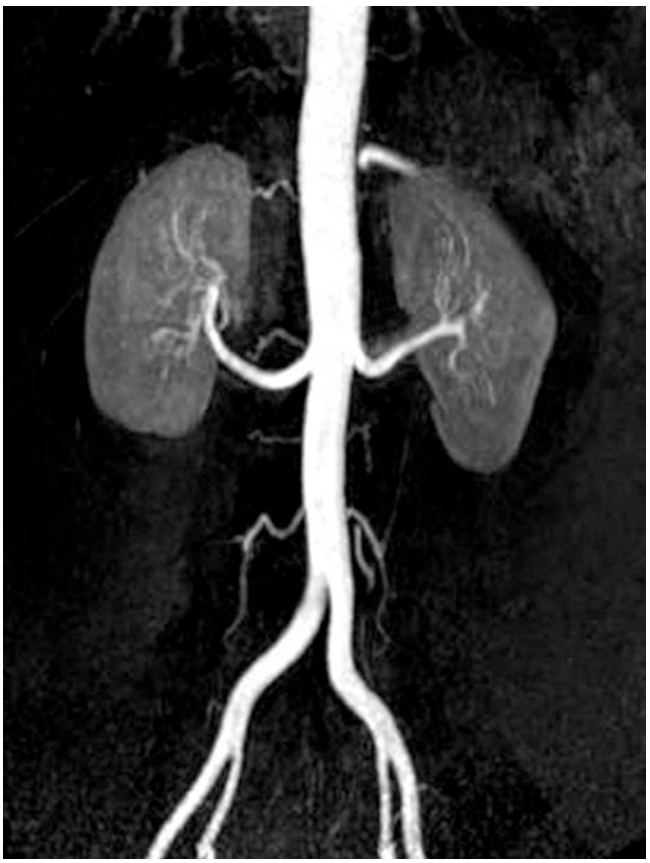

Fig. 33 Normal anatomy of the renal arteries as seen on angio-MR, after Gd-based agent injection

contrast-enhanced methods, which require the intravenous administration of a contrast agent, overcome many of the limitations of 2D-TOF MRA.

Contrast-enhanced 3D MR angiography (Fig. 33) has become the standard technique for renal artery MR angiography due to its speed, high SNR, minimal artifacts, and relatively high spatial resolution. In particular, the use of an MR contrast agent is reported to reduce artifacts in the image and allow images to be acquired more rapidly, both of which should result in an improvement in overall accuracy of the technique. Clinical practice today usually uses a double dose (0.2 mmol/kg) of contrast agent for CE-MRAs. Lowering the dose would result in considerably lower costs and lower risk for nephrogenic systemic fibrosis induction.

3.4 Anatomical Variants of Renal Vessels

Knowledge of the variations in renal vascular anatomy is important for renal transplantation surgery and before laparoscopic donor or partial nephrectomy and vascular reconstruction for renal artery stenosis or abdominal aortic aneurysm. Recently, multidetector CTA has become a principal imaging investigation for the assessment of the renal vasculature and has challenged the role of conventional angiography (Türkvatan et al. 2009). It is an excellent imaging technique because it is a fast and noninvasive tool that provides highly accurate and detailed evaluation of normal renal vascular anatomy and variants. The number, size, and course of the renal arteries and veins are easily identified by CTA. In about one third of the general population, there are variations in number, location, and branching patterns of the renal arteries, with over 30 % of subjects having one or more accessory renal arteries. Familiarity with anatomical variants and their associations contributes to the safety and success of both open and minimally invasive renal surgery.

- Early branching of renal artery. The main renal artery originates at a more or less constant position opposite the renal hilus, from the abdominal aorta, and continues undivided in its straight course to the renal hilum except for small branches including the inferior adrenal, the perirenal, and the ureteral arteries. Frequently, the renal artery presents early branching, and this may have important implications in renal surgery. Prehilar arterial branching is a common variant necessary for the detection of patients undergoing evaluation for donor nephrectomy (Fig. 34). A person with early branching of the renal artery might be considered a poor candidate as a potential living renal donor.
- Hilar and extrahilar accessory renal arteries. An accessory renal artery, other than the main renal artery, is one that arises from the aorta and terminates in the kidney (Satyapal et al. 2001). Accessory renal arteries have also been described as additional, supernumerary, or supplementary. Accessory renal arteries arise from the aorta anywhere from the level of T11 to the level of L4, but may rarely originate from the iliac arteries or superior mesenteric artery. Accessory renal arteries are the sole renal arteries which supply a portion of the renal parenchyma (Fig. 35). They are seen in up to 25–28 % of patients (Satyapal et al. 2001). In healthy adults, the mean maximum diameter of the renal artery lumen is about 5–6 mm. The diameter of accessory renal arteries is highly variable, but it is generally equal to or smaller than the main renal artery. Frequently the accessory artery is visualized coursing into the renal hilum to vascularize the lower renal pole (Fig. 36). Accessory renal arteries may be a contraindication to laparoscopic donor nephrectomy, and injury of a crossing vessel during endopyelotomy for ureteropelvic junction obstruction may result in severe hemorrhage (Yeh et al. 2004). The polar or extrahilar arteries may be ligated or transected unintentionally during renal, aortic, or other retroperitoneal abdominal surgeries. Accessory renal arteries usually arise inferior to the main renal artery, but occasionally will supply the upper pole of the kidney. Renal anomalies such as horseshoe or pelvic

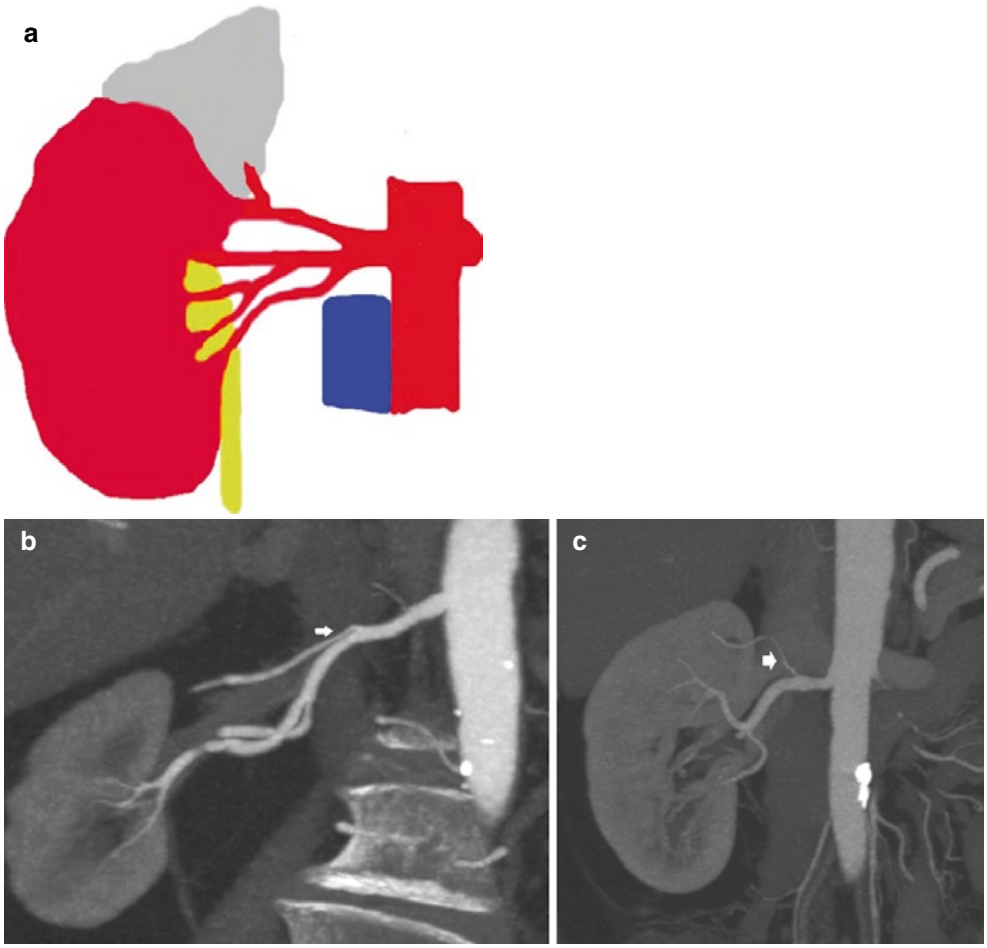

Fig. 34 (**a**–**c**) Early branchings of right renal artery (*arrows*). (**a**) Scheme; (**b**, **c**) CTA, coronal reformations

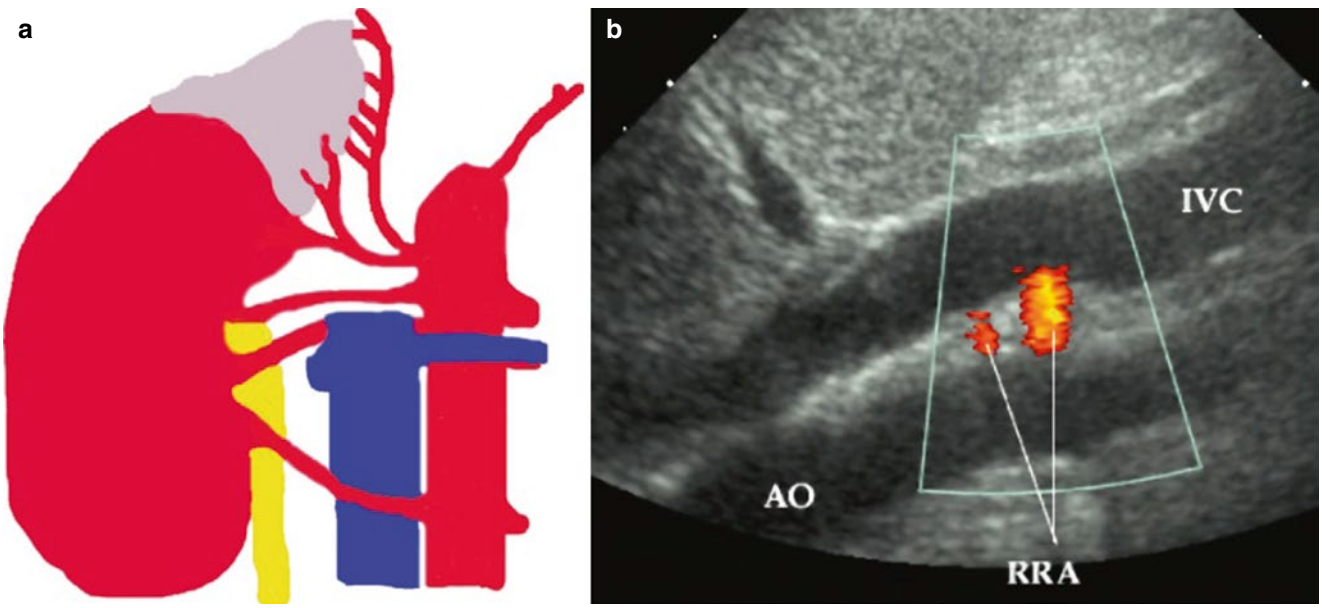

Fig. 35 (**a**) Scheme representing both hilar and extrahilar accessory renal arteries. (**b**) Color Doppler US. The main and accessory renal arteries at their origin from the abdominal aorta. *IVC* Inferior vena cava. *AO* aorta, *RRA* right renal arteries

Fig. 36 (**a**–**d**) Hilar (**a**) Accessory extrahilarrenal arteryperfusing the lower renal pole. (**b**) The extrahilar accessory renal artery that vascularizes the upper renal pole (*white arrow*) originates immediately above the origin of the main renal artery, and it appears hypoplastic in comparison with the main renal artery. (**c**, **d**) The accessory renal artery vascularizing the lower renal pole (*white arrow*) may originate immediately above (**c**) or below (**d**) the origin of the main renal artery (*black arrow*), and it may appear hypoplastic in comparison with the main renal artery (**c**) or with a diameter similar to the main renal artery (**d**). A renal carcinoma is also evident in the lower renal pole on the (**d**) image

kidney almost always have multiple renal arteries that arise from the aorta or iliac arteries. Accessory renal arteries are now routinely seen on CTA or MRA, but are frequently not noted on renal Doppler.

- Right renal artery passing anteriorly to the inferior vena cava. Right renal arteries are traditionally described as passing posterior to the inferior vena cava, although dominant and accessory right renal arteries that pass anteriorly to the inferior vena cava (Fig. 37) have been described in about 5 % of patients, and the anterior rotation of the lower pole of the right kidney should prompt a search for precaval renal arteries (Yeh et al. 2004). A right renal artery that passes anterior to the inferior vena cava is of particular importance for presurgical planning, because it may be injured inadvertently, especially during the retroperitoneal approach when only the right gonadal vein is expected to lie in the precaval area.
- Renal vein anomalies. Anomalies of the renal veins are less common than those of the arteries, but are encountered in clinical practice and may have important implications. All anomalies are variations of the embryological development and represent a persistence of portions of the paired longitudinal channels, the subcardinal and supracardinal veins, which form a ladderlike collar around the aorta. Normally, only the anterior components persist, becoming the renal veins, which course anterior to the aorta. Accessory renal veins are less frequent than accessory renal arteries and are more common on the

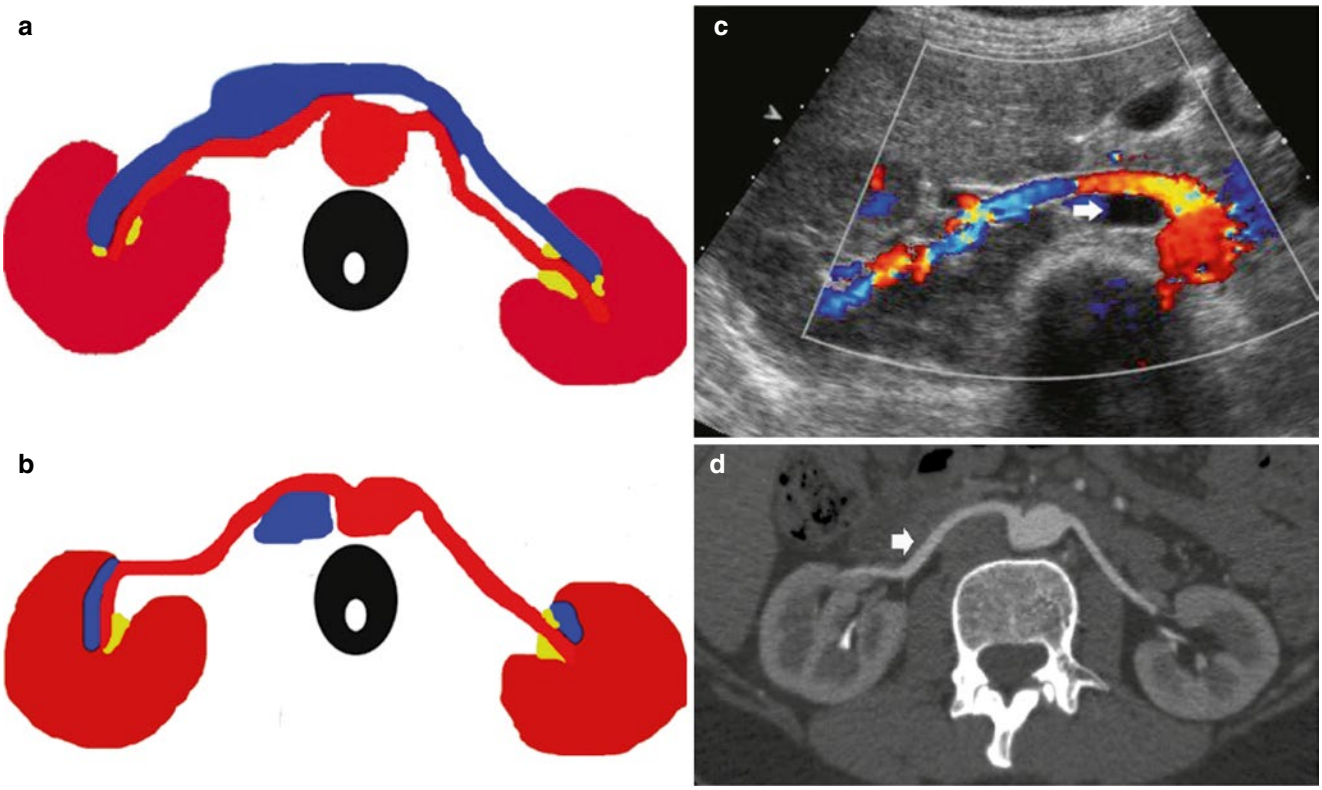

Fig. 37 (**a**) Scheme. Normal anatomy of the renal vessels on the transverse plane. (**b**) Scheme. Precaval right renal artery. (**c**) Color Doppler US. Transverse plane. Precaval right renal artery (*arrow*). (**d**) CTA. Precaval renal artery (*arrow*)

right than the left. Left renal vein variants include the circumaortic and retroaortic renal veins. Knowledge of these anomalies becomes important in surgical planning, inferior vena cava (IVC) filter placement, and collection of renal or adrenal vein samples. The most common anomaly of the left renal venous system is the circumaortic renal vein (Fig. 38). The circumaortic renal vein represents persistence of the posteriorly located left supracardinal vein and a midline supracardinal anastomosis between right and left vessels. This anomaly has been reported in 2–16 % of patients, based on anatomical and angiographic studies. Persistence of the whole collar results in a circumaortic renal vein, which is a more common anomaly than an isolated retroaortic renal vein. In this anomaly, the left renal vein bifurcates into ventral and dorsal limb, which encircles the abdominal aorta. Less common is the retroaortic renal vein (Fig. 39), seen in up to 4 % of patients. Here, the single left renal vein courses posterior to the aorta and drains into the lower lumbar portion of the IVC. In addition, multiple renal veins are seen in approximately 15 % of the patients. Supernumerary renal veins often are retroaortic when present on the left. Reed et al. (1982) reported from a CT series that 1.8 % of patients have a single retroaortic renal vein. In a recent study by Karazincir et al. (2007), the incidence of retroaortic left renal vein was found to be significantly higher in patients with varicocele compared with control patients. The left renal vein receives drainage from the inferior phrenic, capsular, ureteric, adrenal, and gonadal veins. In patients with a left-sided IVC, the left common iliac vein continues cranially as the left IVC and drains into the inferior aspect of the left renal vein. The right renal vein is shorter than the left and courses obliquely into the IVC. The right renal vein receives capsular and ureteric veins; however, the right inferior phrenic and gonadal veins enter directly into the IVC. Valves may be present within the renal veins with marked variation in the reported incidence. Renal vein varices may be secondary to renal vein thrombosis or portal hypertension, or may be idiopathic. Like varicoceles, renal varices are more common on the left than on the right. The "nutcracker" phenomenon results from compression of the left renal vein between the superior mesenteric artery and the aorta and may lead to left renal vein hypertension, hematuria, and varix formation. It is important to remember that a distended left renal vein may be seen in 51–72 % of the normal population by CT, MR, or ultrasound (Buschi et al. 1980). Therefore, measurement of a pressure gradient between the IVC and the left renal vein needs to be done before renal vein compression

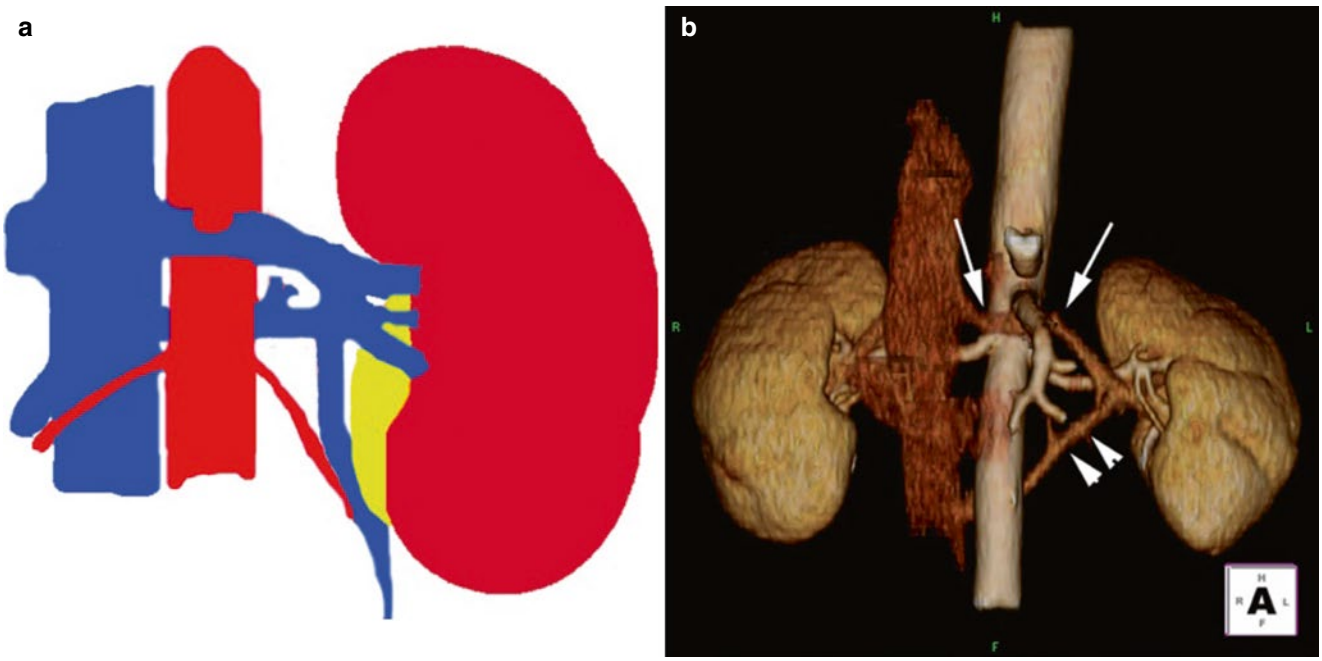

Fig. 38 (**a**, **b**) Anatomical variants of renal veins. (**a**) The left renal vein bifurcates into ventral and dorsal limb which encircle the abdominal aorta. (**b**) Coronal volume reconstructed image of CTA shows the preaortic venous component (*arrows*) at the level of the renal arteries and retroaortic component more caudally located (*arrowheads*) (Courtesy of Dr. Therese M. Weber; Dept of Radiology; University of Alabama at Birmingham)

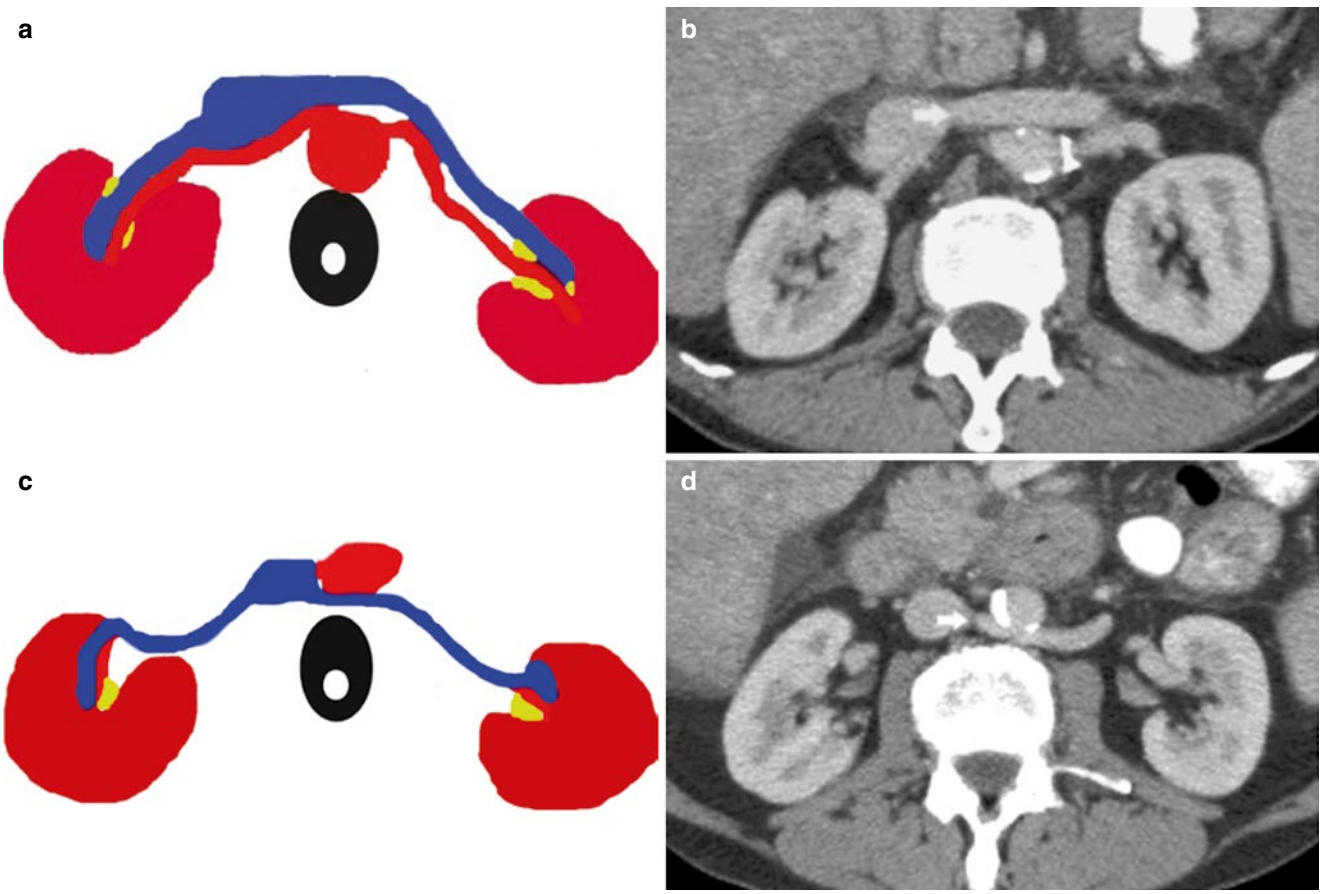

Fig. 39 (**a**) Scheme. Normal anatomy of the renal vessels on the transverse plane. (**b**) Contrast-enhanced CT. Transverse plane. Normal anatomy of the left renal vein (*arrow*) passing anteriorly to the aorta. (**c**) Scheme. Retroaortic left renal vein. (**d**) Retroaortic left renal vein (*arrow*)

diagnosis. Color Doppler may provide noninvasive evidence of renal vein compression when collateral veins are demonstrated. In cases of renal vein thrombosis, collateral pathways through the inferior phrenic, adrenal, gonadal, and ureteric veins may be involved with left renal vein thrombosis, while only the ureteric vein forms collaterals with the right renal vein.

- Venous anomalies may also affect the ureter, such as a circumcaval or retrocaval ureter, which are very rare. A circumcaval ureter occurs more commonly in men than women and is usually an incidental finding. Persistence of the right subcardinal vein traps the ureter behind the IVC. The ureter passes posterior to the IVC, then crosses anteriorly around the medial border of the cava to partially encircle the IVC. On CT, the IVC will have a more lateral location than normally seen, usually lying lateral to the right pedicle of the third lumbar vertebral body, and the course of the opacified ureter can be followed around the IVC.

4 Normal Radiological Anatomy of the Urinary Tract and Anatomical Variants

4.1 Excretory Urography and Anterograde and Retrograde Pyelography

Intravenous urography is the examination traditionally employed to assess the urinary tract pathology (Fig. 40a), and it was used for a large variety of clinical indications. Its utilization decreased when each of these indications was shown not to be clinically valid, and cross-sectional imaging techniques have since proved superior to intravenous urography for most, if not all, remaining indications (Silverman et al. 2009). Even until the late 1990s, intravenous urography, because of its superior spatial resolution, was still considered the examination of choice for evaluating the urothelium (Silverman et al. 2009). When unenhanced CT was shown to reliably detect urolithiasis, intravenous urography was pronounced dead in 1999 with the caveat that there

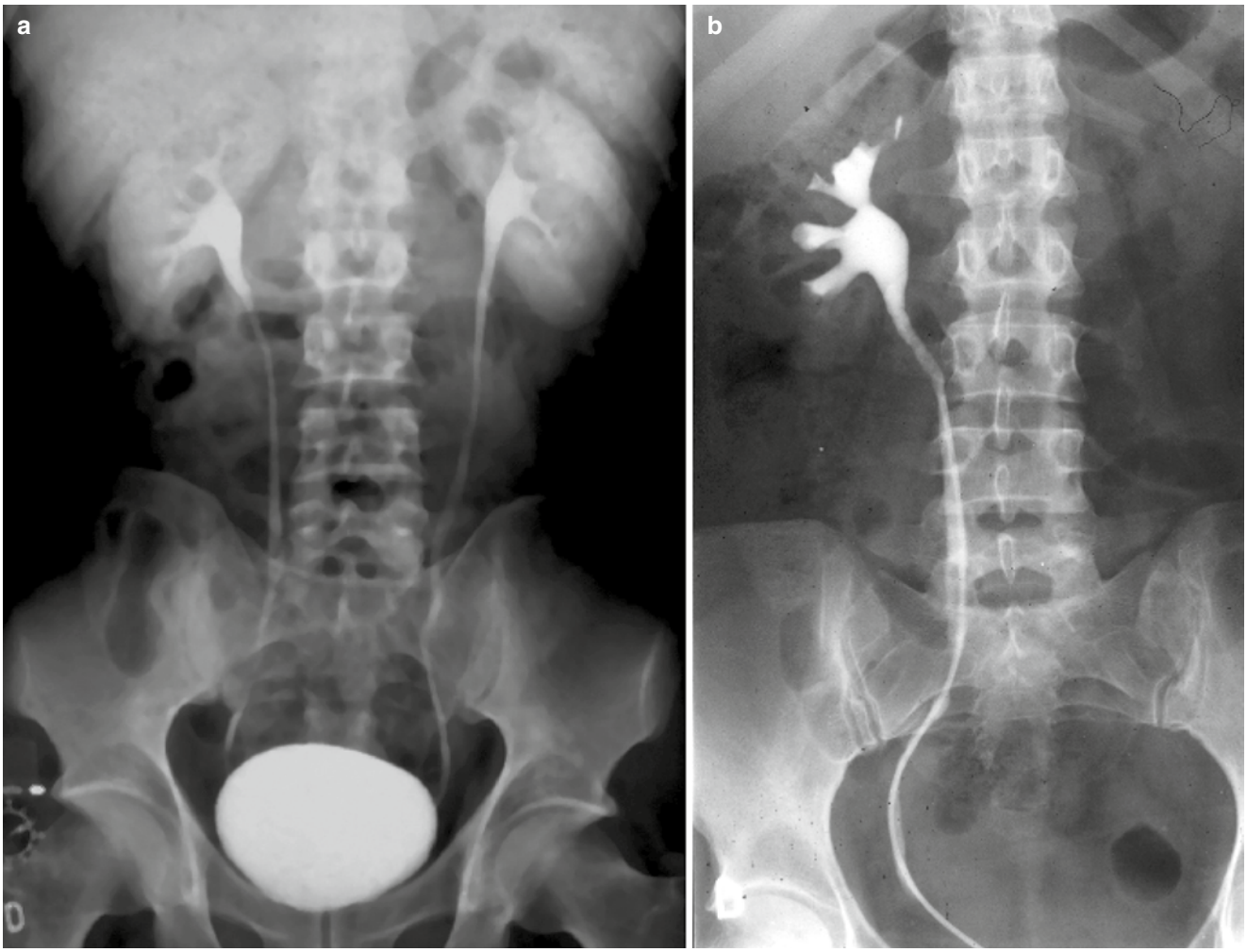

Fig. 40 (**a**, **b**) Normal anatomy of the intrarenal urinary tract. (**a**) Intravenous excretory urography; (**b**) retrograde pyelography

might remain rare instances in which it is an appropriate examination (Amis 1999).

The usual examination protocol employed in the intravenous urography is variable between the different imaging departments. The fundamental examination included a preliminary plain radiograph of the abdomen and nephrotomograms from 60 to 90 s after iodinated contrast agent injection to assess cortical nephrogram representing contrast material within the tubules. Then a radiograph on the renal urinary tract is obtained 5–7 min after contrast injection, and under balloon ureteral compression, while a panoramic radiograph of the whole urinary tract is obtained 15 min after contrast injection after removal of the balloon compression employed to assess the whole urinary tract. Finally, 20–30 min after contract injection, radiographs were performed on the bladder.

When depicted frontally (Fig. 41), a minor calyx appears circular, while when depicted in profile, the minor calyx is concave connected to two well-defined, sharp forniceal angles (Fig. 42). All branches from the pelvis, whether single or multiple, are defined infundibula. The infundibulum is also known as major calyx.

Anterograde pyelography is the evaluation of the urinary tract after the injection of the iodinated contrast agent in the renal pelvis after a nephrostomy procedure. The principal indication is the assessment of hydroureteronephrosis to identify the nature and the level of the obstruction in a functionally excluded kidney (absence of contrast excretion after 24 h from i.v. contrast administration) or to assess the correct position of a nephrostomy drainage. Retrograde pyelography (Fig. 40b) is performed after incannulation of the interior ureteral meatus, and its principal indication is the assessment of opacification defects of the urinary tract. It is invasive and rarely performed.

4.2 CT Urography

Nowadays, the development of CT urography (CTU) (Fig. 43) has completely covered all the clinical indications previously addressed by intravenous urography. The term CTU is often used in clinical practice for a multitude of multidetector computed tomography (MDCT) techniques for the evaluation of the urinary tract. CTU became conceptually possible with the advent of MDCT, the final technologic advance needed to image the urothelium in detail (Silverman et al. 2009). MDCT provides the ability to obtain thin (submillimeter) collimated data of the entire urinary tract during a short, single breath hold (Van Der Molen et al. 2008). The resulting thin section images provided higher spatial resolution relative to that of single-detector CT scans (although not as high as with intravenous urography). Also, isotropic voxels allowed images of equal spatial resolution to be obtained in any plane. The indications for CT were expanded to include hematuria (Joffe et al. 2003). Symptomatic hematuria in patients younger than 40 years should be evaluated by unenhanced CT for the identification of calculi, while asymptomatic hematuria in patients older than 40 years should be evaluated by CTU. Even though urinary tract calculi, bladder tumors, and prostate-related process are the most common causes of hematuria, upper urinary tract urothelial neoplasms must be excluded frequently. Other indications for CTU are the identification of congenital malformations of the intrarenal excretory tract (e.g., in patients in whom a lithotripsy procedure is scheduled), renal infections, renal tuberculosis, suspected papillary necrosis, identification and staging of renal tumors, renal traumas, characterization of complicated (e.g., hemorrhagic cysts) or complex renal masses (e.g., renal tumors with a solid and cystic component), renal colic and acute flank pain, and ureteral pathology.

4.3 Magnetic Resonance Imaging and MR Urography

MR urography has received a relatively lower attention than MDCT urography, being hampered by the low spatial resolution, which is crucial for calyceal evaluation and by the requirement of updated MR units. However, excellent contrast resolution and lack of ionizing radiation make MR urography a useful technique for noninvasively evaluating the entire urinary tract, especially when ionizing radiation is to be avoided, such as in pediatric or pregnant patients. The MR urographic techniques can be divided into two categories: static-fluid MR urography and excretory MR urography.

The static-fluid MR urography (Fig. 44) utilizes unenhanced, heavily T2-weighted pulse sequences to image the urinary tract. On the heavily T2-weighted images, the urinary tract is hyperintense because of its long relaxation time, independent of the excretory renal function. This technique is ideally suited for patients with dilated or obstructed collecting system. In excretory MR urography (Fig. 45), intravenous gadolinium is combined with a T1-weighted 3D gradient echo (GRE) sequence. The practicability of excretory MR urography depends on the ability of the kidneys to excrete the intravenously administered gadolinium agent. The administration of low-dose furosemide can improve the quality of excretory MR urography by enhancing urine flow and therefore providing a uniform distribution of the contrast material inside the entire urinary tract. Excretory MR urography provides high-quality images of both nondilated and obstructed collecting systems.

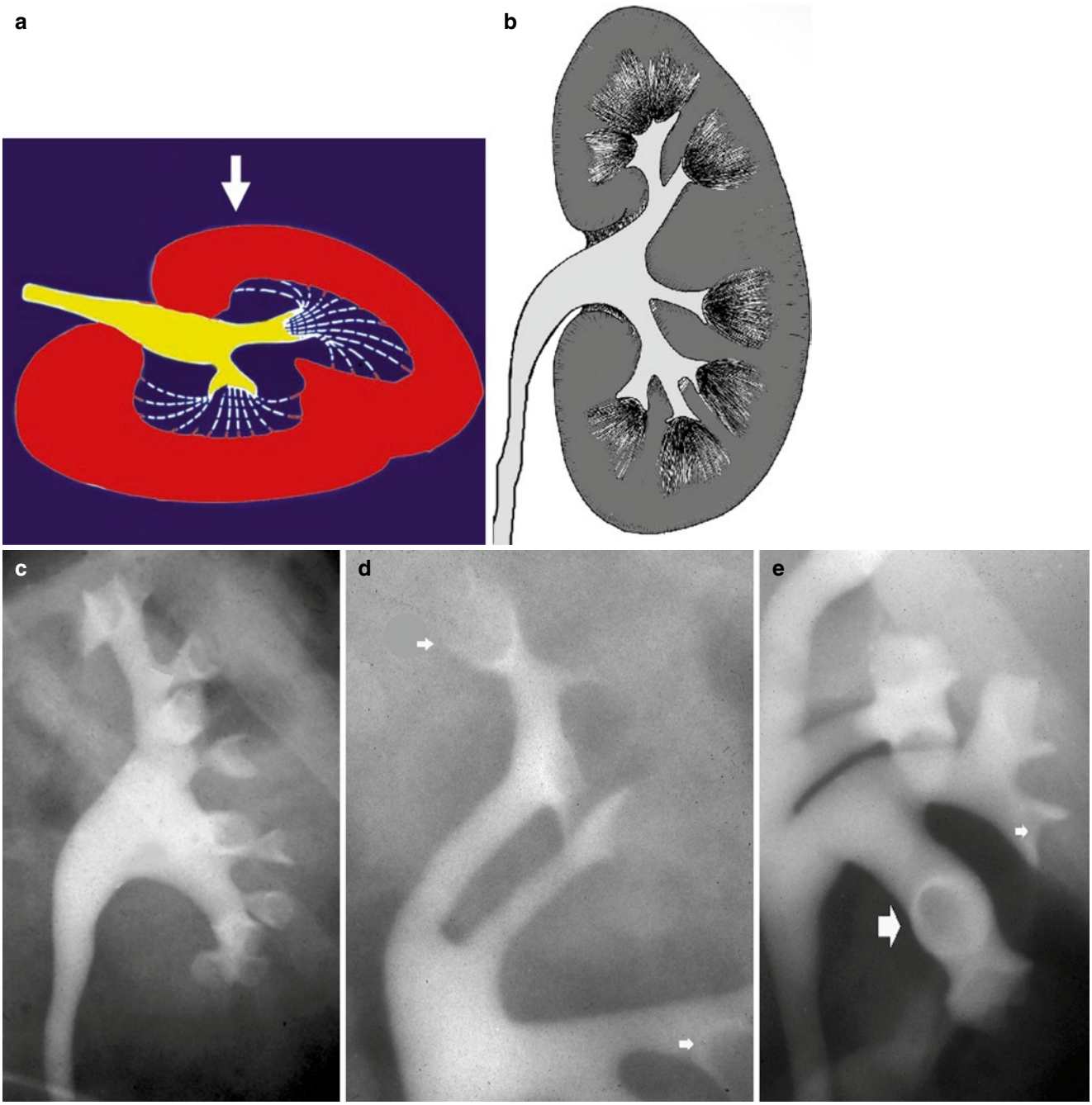

Fig. 41 (**a**–**e**) Normal appearance of the intrarenal urinary tract as seen on intravenous urography according to the X-ray beam incidence (*arrow*). (**a**–**c**) Normal 5-min urogram with orthogonal incidence of the X-ray beam. The renal pelvis branches to form infundibula. (**c**) The calyx is formed by the impression of the papilla, and the fornix is the side of the calyx. The calyx is a concave structure receiving the tip of the papilla of the renal medulla, and the fornices represent the side projections of the calyx surrounding the papilla. (**d**, **e**) When depicted frontally a minor calyx appears circular (*large arrow*), while when depicted in profile (*small arrows*) the minor calyx is concave connected to two well-defined, sharp forniceal angles

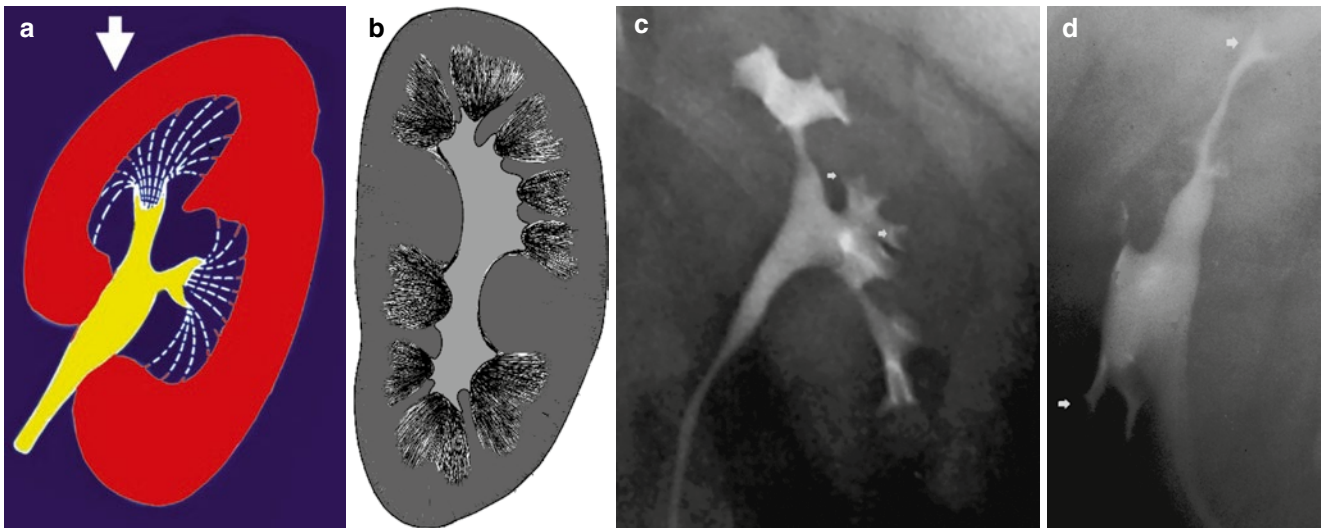

Fig. 42 (**a**–**d**) Normal appearance of the intrarenal urinary tract as seen on intravenous urography according to the X-ray beam incidence (*arrow*). (**a**, **b**) Schemes representing the incidence of the X-ray beam (**a**) and the resulting image (**b**). (**c**, **d**) Normal 5-min excretory urogram with a progressive increasing obliquity of the incidence of the X-ray beam. The minor calyx is concave (*small arrows*) connected to well-defined, sharp forniceal angles

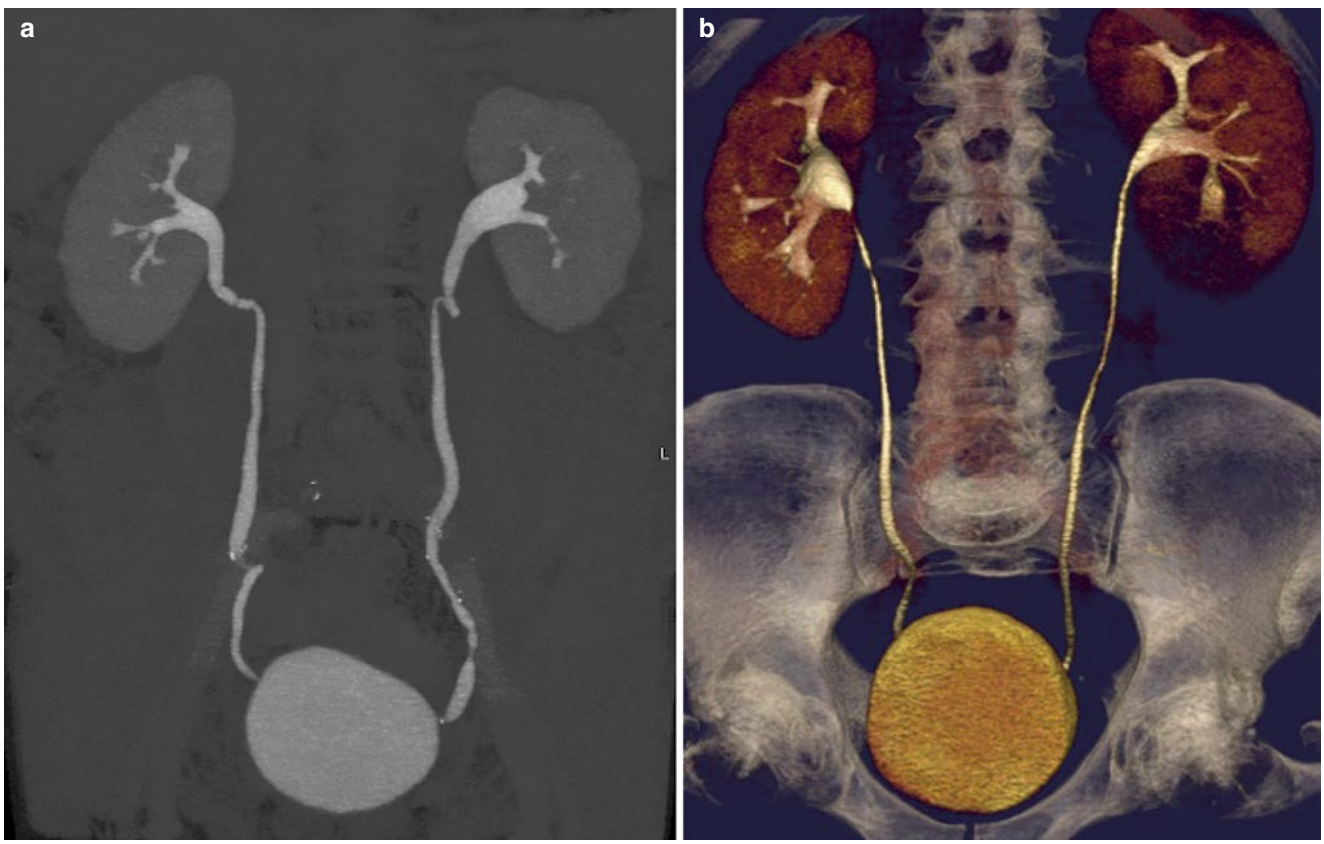

Fig. 43 (**a**, **b**) Normal anatomy and anatomical variants of the renal calices and pelvis as seen on CTU. (**a**) 3D maximum intensity projection; (**b**) 3D color-coded volume rendering

Fig. 44 Normal anatomy of the renal calices and pelvis as seen on static-fluid MR urography

Early practitioners of MR urography used T2-weighted techniques alone, such as rapid acquisition with relaxation enhancement (RARE) and half-Fourier acquisition single-shot turbo spin echo (HASTE), to image the renal collecting systems, ureters, and bladder, essentially treating the urinary tract as a static collection of fluid. T2-weighted MR techniques rely on the intrinsically high signal intensity of urine for image contrast and therefore do not require the administration of intravenous contrast material. Coronal T2-weighted images of the entire urinary tract were particularly attractive since they mimicked the images obtained with intravenous urography. The main appeal of these techniques was that they could be performed quickly and in any image plane. Furthermore, because T2-weighted MR urography techniques could be performed without ionizing radiation or intravenous contrast material, they were considered to have their greatest utility in children, pregnant women, or other patients in whom intravenous contrast material was contraindicated. However, the clinical utility of MR urography performed with T2-weighted imaging alone is limited in patients with nondistended urinary collecting systems. For urinary tracts that are not distended, imaging with a full urinary bladder can improve upper tract visualization, but additional techniques are needed often.

The challenge of MR urography is to obtain diagnostic quality images of the KUB within a reasonable amount of time while limiting the effects of respiratory motion, ureteral peristalsis, and flowing urine. Impediments to addressing this challenge satisfactorily include a finite SNR for a given MR system and the limited breath-holding capacity of patients. Because SNR constrains the maximum interpretable resolution achievable with MR imaging,

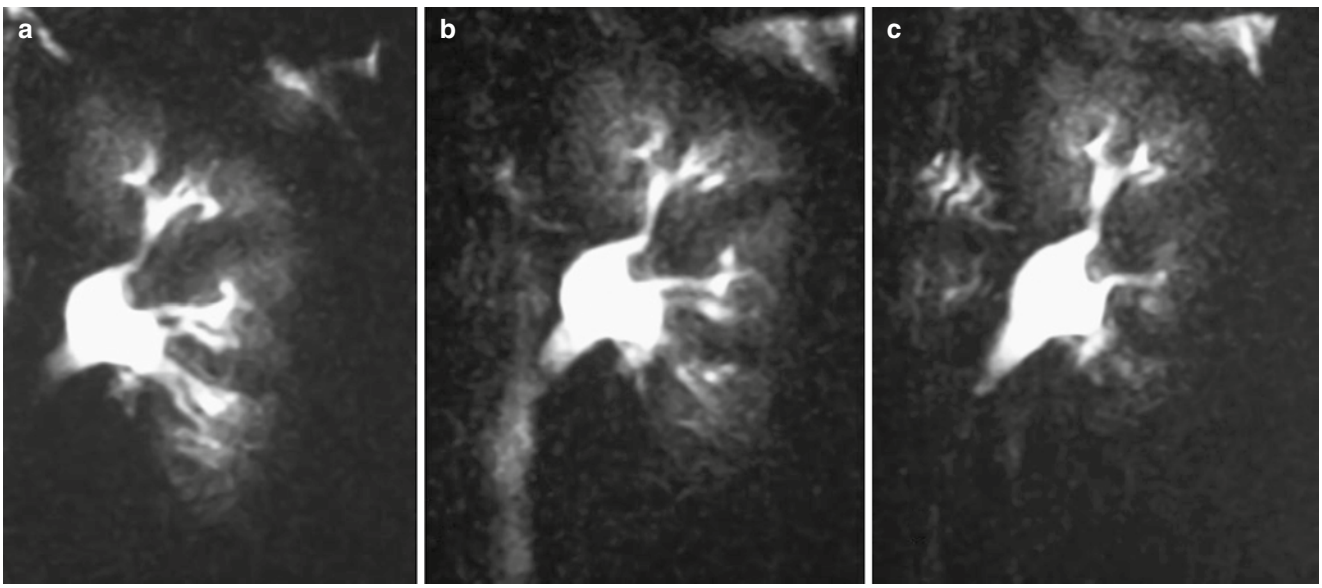

Fig. 45 (**a**–**c**) Normal MR excretory urography after Gd-based contrast agent injection

MR urography is best performed with a phased array surface coil; these coils increase SNR. Exceptions include some gravid patients in the latter stages of pregnancy and large patients whom the imager bore cannot accommodate with a surface coil in place. Depending on the MR imaging system, some surface coils limit the field of view to less than that required to encompass the kidneys and bladder in a single acquisition. In such cases, the urinary tract is imaged in segments, repositioning the surface coil as necessary.

Further increases in SNR can be achieved by imaging patients with higher field strength, 3.0-T MR systems. The SNR gained when moving from 1.5 to 3.0 T can be used to improve spatial or temporal resolution. Theoretically, improvements in spatial resolution could improve detection of small urothelial lesions, although this has not been systematically studied to date. Additionally, there is evidence to suggest that the conspicuity of enhancement related to gadolinium chelates increases at 3.0 T relative to 1.5 T, although the impact of this difference is unknown for MR urography. The potential benefits of 3.0-T MR imaging must be weighed against the limitations inherent to higher field strength imaging, such as increased specific absorption rate, prolonged T1 relaxation times, and worsening of some artifacts.

The principal indications for the MR urography are the evaluation of urothelial tumors, anomalies of the urinary tract, and the assessment of urinary tract dilatation and obstructive disease.

4.4 Anatomical Variants of the Urinary Tract

Intravenous urography and CTU provide a reliable depiction of the intrarenal urinary tract, which presents an extremely variable morphology (Figs. 46, 47 and 48). Congenital variants of the pelvocalyceal system are common and may be observed in about 4 % of the general population. The renal pelvis may present a progressively increasing separation between the upper and lower group renal calyces (Fig. 48), and it may be completely intrarenal, completely extrarenal, or a combination of both (Fig. 49) (Friedenberg and Dunbar 1990).

The renal calyx is a concave structure receiving the tip of the papilla of the renal medulla, and the fornices represent the side projections of the calyx surrounding the papilla (Fig. 41). Frequently, multiple single calyces fail to completely divide and form a larger compound calyx, which is normally seen in the upper and lower poles of the kidney (Figs. 50 and 51). Compound calyces present a distorted shape, and the circular shape of the minor calyx is frequently not present. Multiple papillae (two or more) draining into a single calyx are defined as a compound calyx. The average number of calyces is seven to nine per kidney, even though it may be as low as four or five, or as high as 18 or 19, or more (polycalycosis). Many fetal urinary apparatus modifications can be identified during pregnancy by US.

- Complex renal calyces and megacalycosis. Megacalycosis (Fig. 52a, b) represents a nonobstructive asymptomatic congenital disorder manifesting as dilatation of some or all renal calyces and normal renal pelvis and ureter. It may be associated with megaureter. Renal calyces present a blunted morphology as in renal papillary necrosis. Typically, megacalycosis involves all of the calyces uniformly, and there is a greater number of calyces than normal (i.e., >15). Papillary necrosis tends to be dissimilar from calyx to calyx, and the number of calyces is not increased.
- Calyceal diverticula. Calyceal diverticula represent a focal extrinsic dilatation of a renal calyx (Fig. 52c). Typically, calyceal diverticula connect to the calyceal fornix and project into the renal cortex (including a column of interlobar cortex) and not into the medulla.
- Duplication anomalies. Duplications in the renal collecting system can be depicted by CT or MR during the excretory phase. Multiplanar reconstructions may be useful for this task. Duplication anomalies include bifid renal pelvis (Fig. 48c) and complete or incomplete ureteral duplication, which develop when two or more ureteral buds form from the mesonephric duct. Ureteropelvic duplication (duplex collecting system) consists in the presence of two separate pyelocalyceal collecting system in one kidney extending from a bifid pelvis to a bifid ureter. Two draining ureters may join above the bladder (partial duplication) (Fig. 53) or insert into the bladder separately (complete duplication) (Fig. 54). Duplication anomalies result from the development of a second ureteric bud (complete duplication) or redundant duplication of the single ureteric bud. Complete ureteral duplication (Fig. 54), with a common or ectopic entry of the upper pole moiety, is less common than incomplete duplication. The ureter draining the upper segment of the kidney prevalently inserts in the bladder inferior and medial to the ureter draining the lower segment of the kidney (Weigert–Meyer rule) representing the truly ectopic ureter in a complete duplication which is prone to ureteroceles (Fig. 55) and extravesical insertion or vesicoureteral reflux. The lower moiety of the completely duplicated system is generally normal. Ureteral duplication may also be bilateral (Fig. 56). Triple moiety may also be observed (Fig. 57).
- The anatomical variants of the renal urinary tract must be differentiated from the morphological changes visible on renal calyces, infundibula, and renal pelvis on intravenous excretory urography, CTU, or MR urography due to specific renal pathologies (see Appendix).

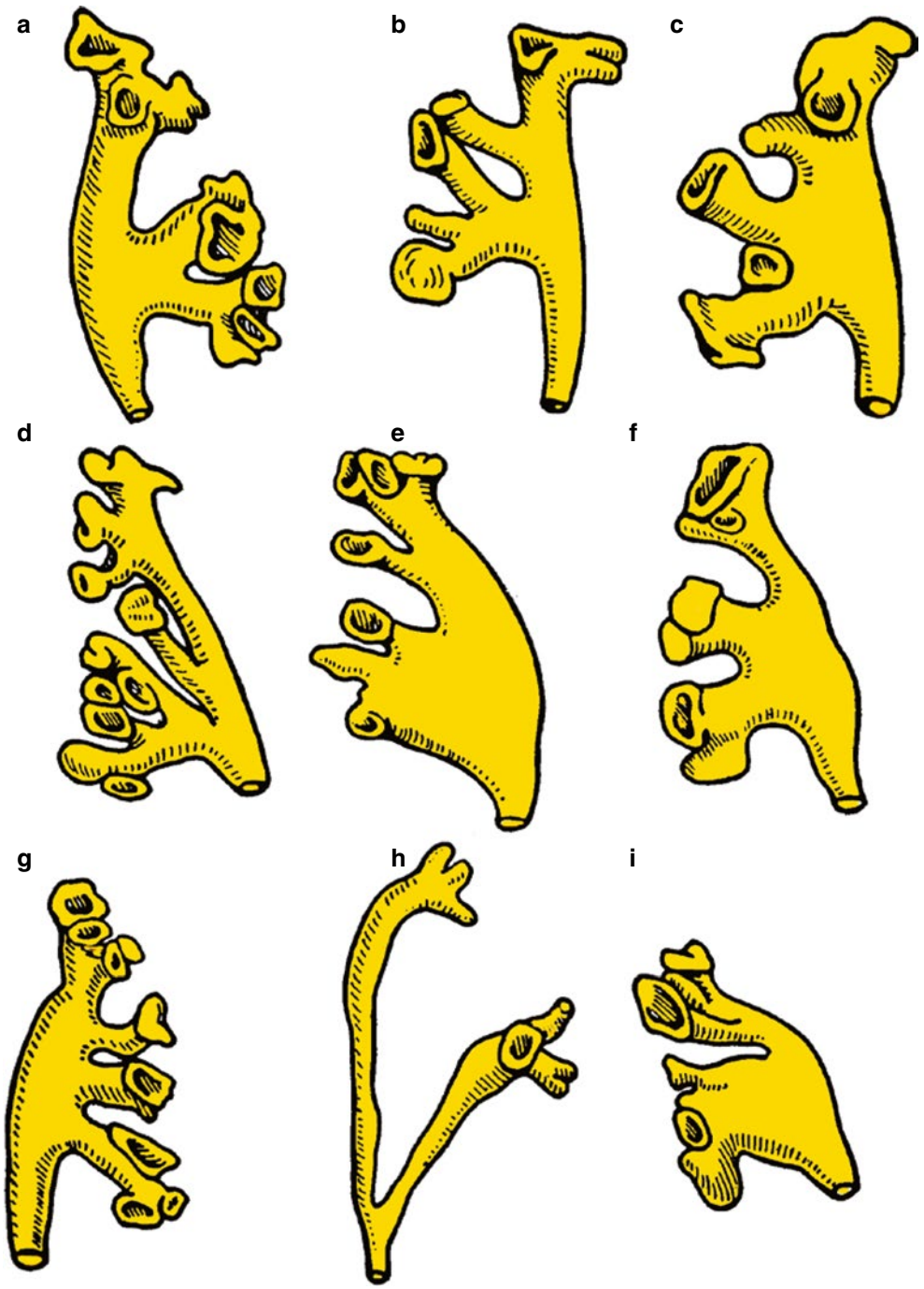

Fig. 46 (**a**–**i**) Scheme. Different morphologies of the upper urinary tract including the calyces, infundibula, and pelvis which can be identified on intravenous excretory urography or CT urography

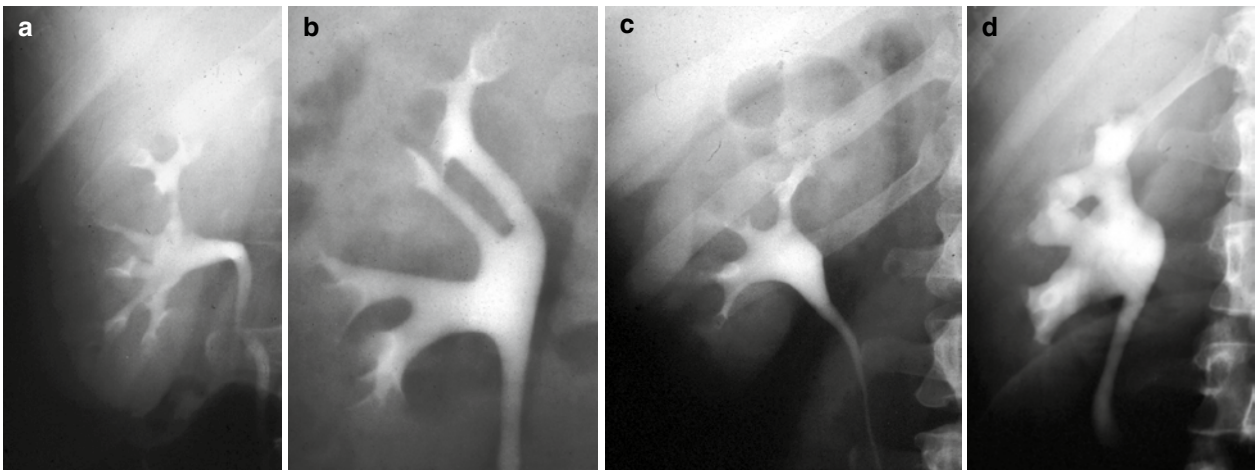

Fig. 47 (**a**–**d**) Intravenous excretory urography. Different morphologies of the upper urinary tract

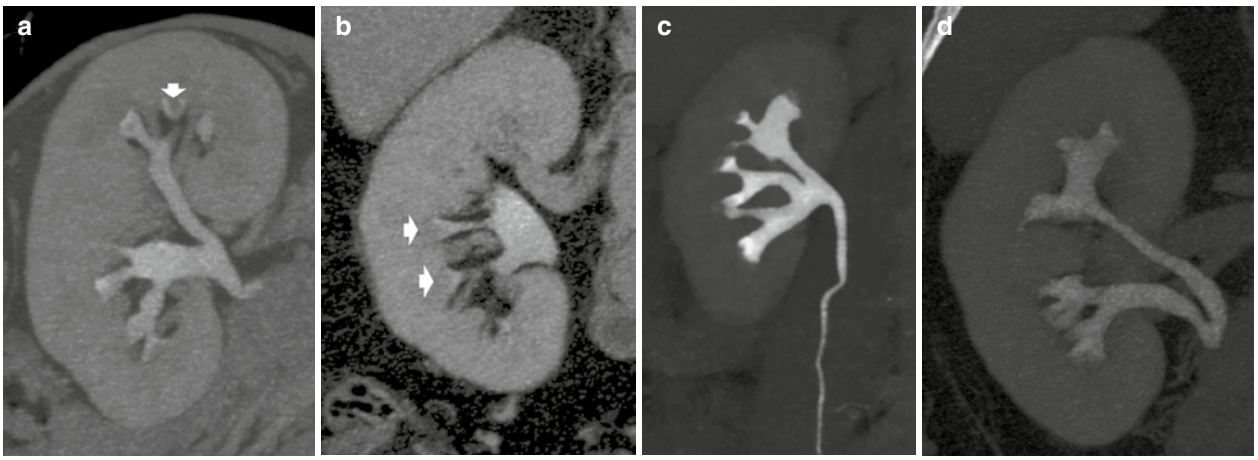

Fig. 48 (**a**–**d**) CT urography. Different morphologies of the upper urinary tract. (**a**, **b**) Usual morphology of the renal calyces and renal pelvis with a progressive more clear division between the upper and lower group calyces also with evidence of renal papillae (*arrows*); (**c**, **d**) bifid renal pelvis

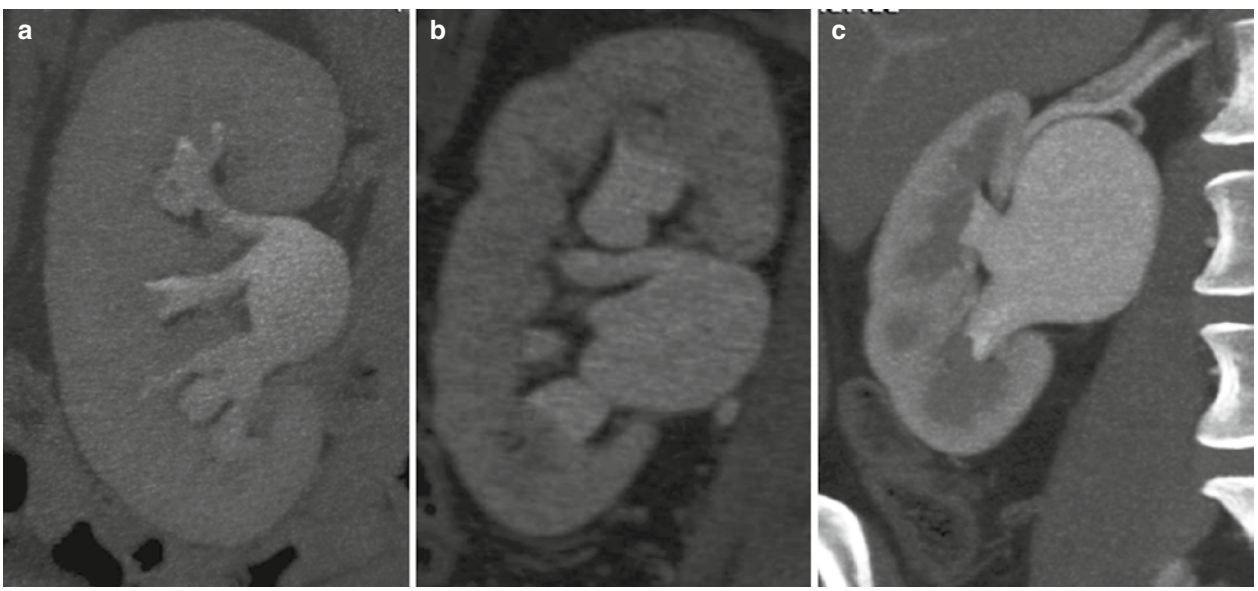

Fig. 49 (**a**–**c**) CTU. Normal appearance of renal pelvis and renal calyces, and anatomical variants. (**a**) Distended pelvis; intrarenal (**b**) and extrarenal (**c**) ampullary pelvis in which calyces open in a common dilated pelvis

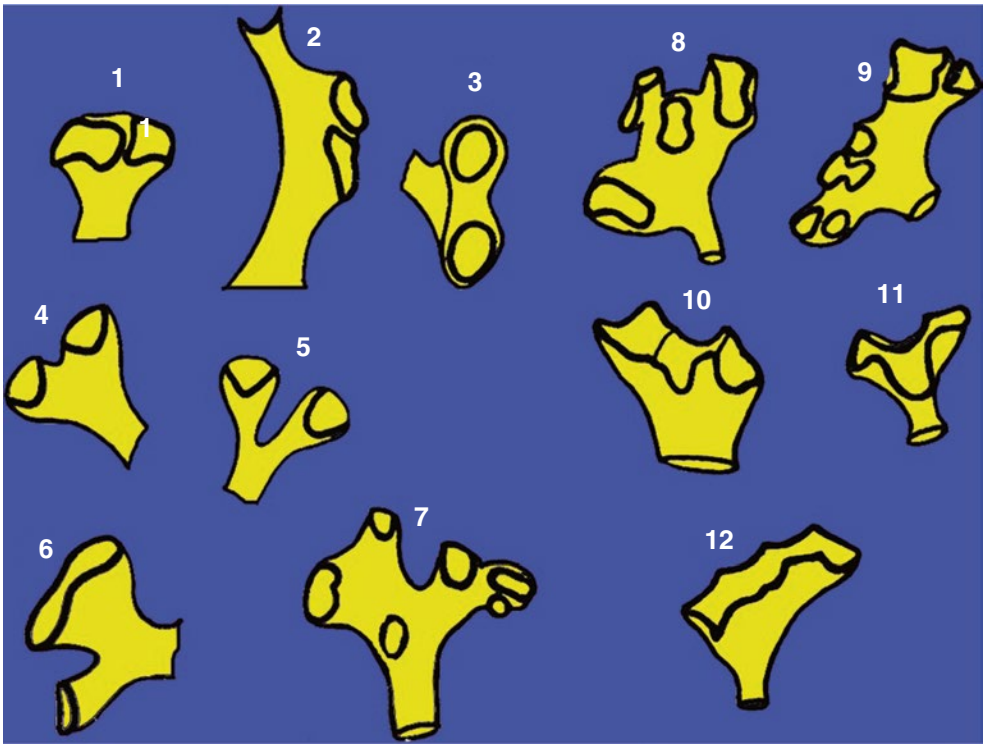

Fig. 50 Scheme. Normal morphology of the kidney and upper urinary tract. Different morphologies of renal papillae. (*1*) Two duplex papillae with a single calyx; (*2*) Two duplex papillae draining into an upper pole calicine system; (*3–4*) Two separated papillae with a single calyx; (*5*) Separated papillae with separate calyces; (*6*) One separate and one duplex papilla; (*7–9*) Multiple separate single or duplex papillae draining into one complex calyx; (*10–12*) Multiple fused papillae draining into one calyx

5 Appendix: Basic Morphological Changes of the Intrarenal Urinary Tract Visible on Intravenous Excretory Urography and Multidetector CT Urography

The anatomical variants of the normal renal urinary tract (see Fig. 58) must be differentiated from the pathologic morphological changes visible on renal calyces, infundibula, and renal pelvis on intravenous excretory urography, multidetector computed tomography urography (CTU), or MR urography due to specific renal pathologies.

Essentially, two fundamental pathologic morphological changes of the renal calices may be identified by intravenous excretory urography or multidetector CTU corresponding to plus (contrast agent projecting outside the renal calyx profile) and minus (contrast filling defects within the renal calyx or pelvis profile) images. To identify the fundamental alterations of the renal urinary tract, and particularly of the renal calyces, it is useful to consider an ideal interpapillary line connecting the apex of the renal papillae (Hodson's line). Plus images include calyceal deformities and cavitations (Fig. 59), calyceal deformities due to parenchymal scarring (Fig. 60), urinary tract dilatation (Fig. 61), and calyceal deformities due to papillary atrophy (Fig. 62).

Minus images include calyceal defects or amputations (Fig. 63), changes of the infundibulum or calyceal profile (Fig. 64), or renal pelvis or calyceal displacement (Fig. 65).

Fig. 51 (**a**–**c**) Intravenous excretory urography. (**d**) Multidetector CTU. Various appearance of compound calyx (*arrow* in **d**)

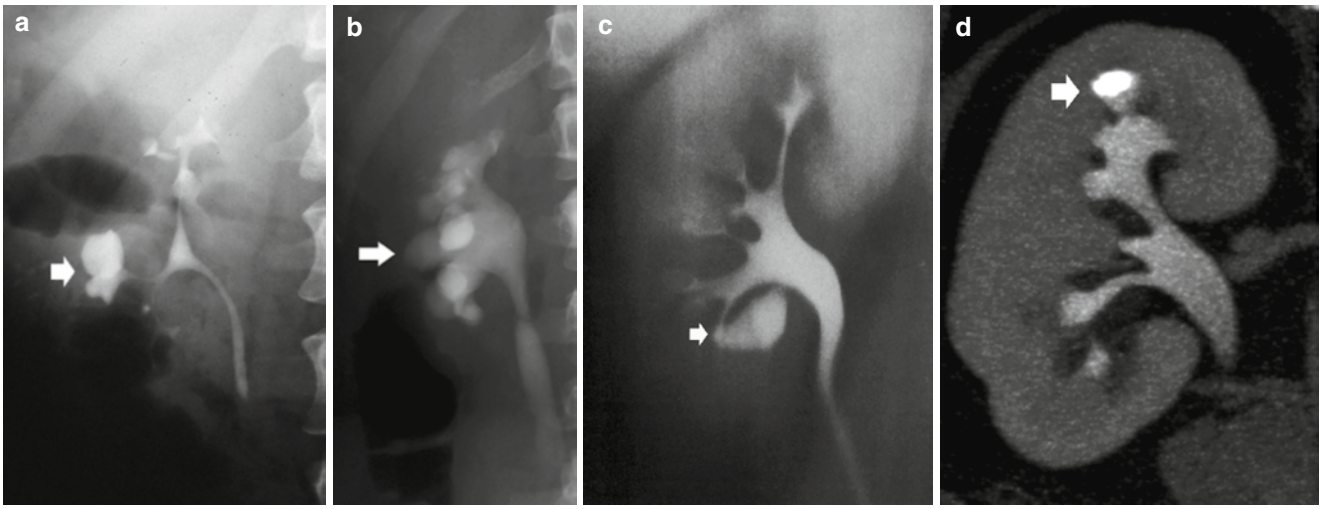

Fig. 52 (**a**, **b**) Intravenous excretory urography. Megacalycosis (*arrow*) involving one (**a**) or multiple renal calyces (**b**). (**c**) Intravenous excretory urography. Calyceal diverticulum (*arrow*). (**d**) CTU. Calyceal diverticulum with a renal stone (*arrow*)

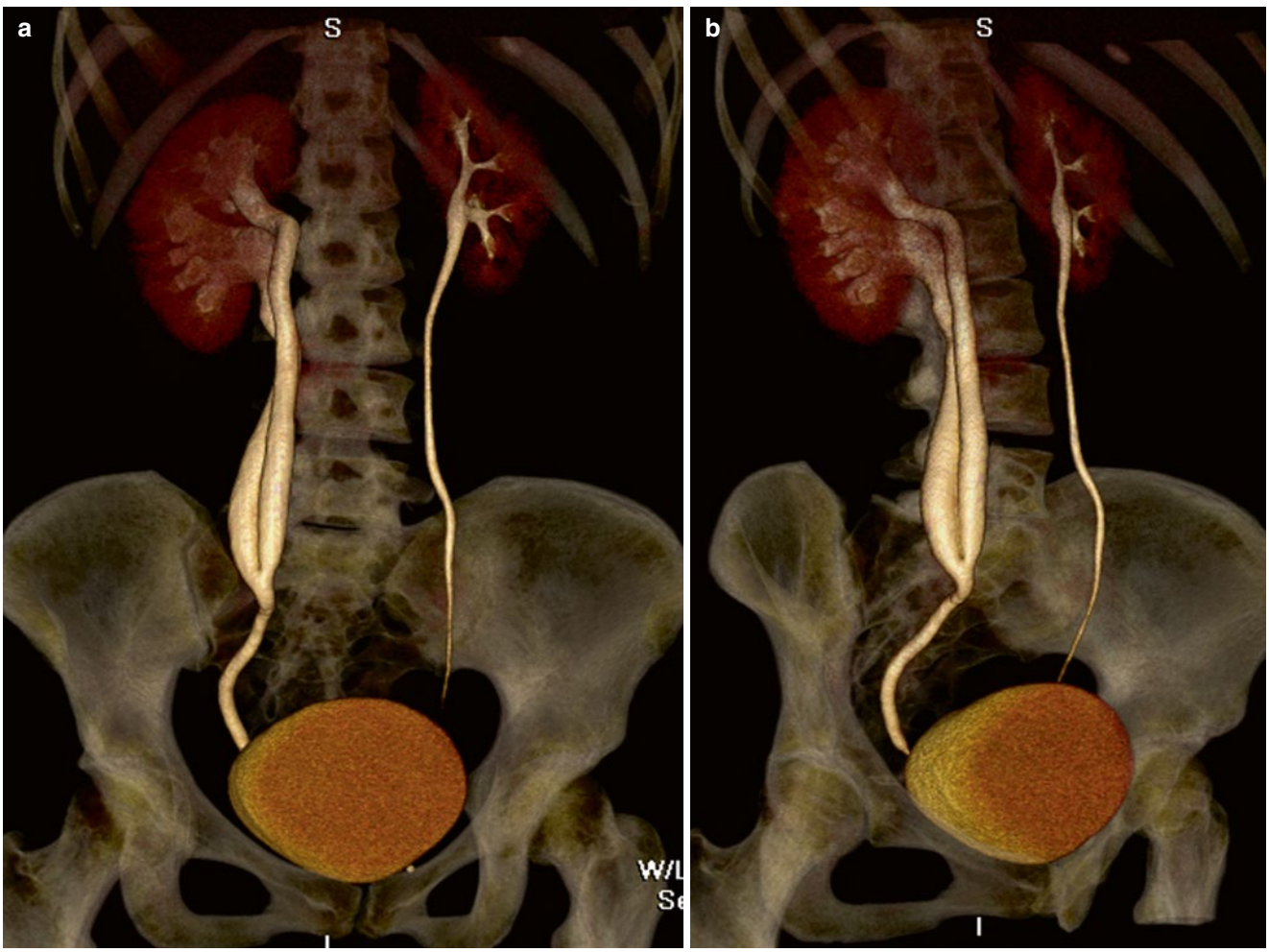

Fig. 53 (**a**, **b**) CT urography. 3D volume-rendered color-coded images. Incomplete urinary tract duplication on the right side

Fig. 54 CT urography. 3D volume-rendered color-coded images. Complete urinary tract duplication on the left side

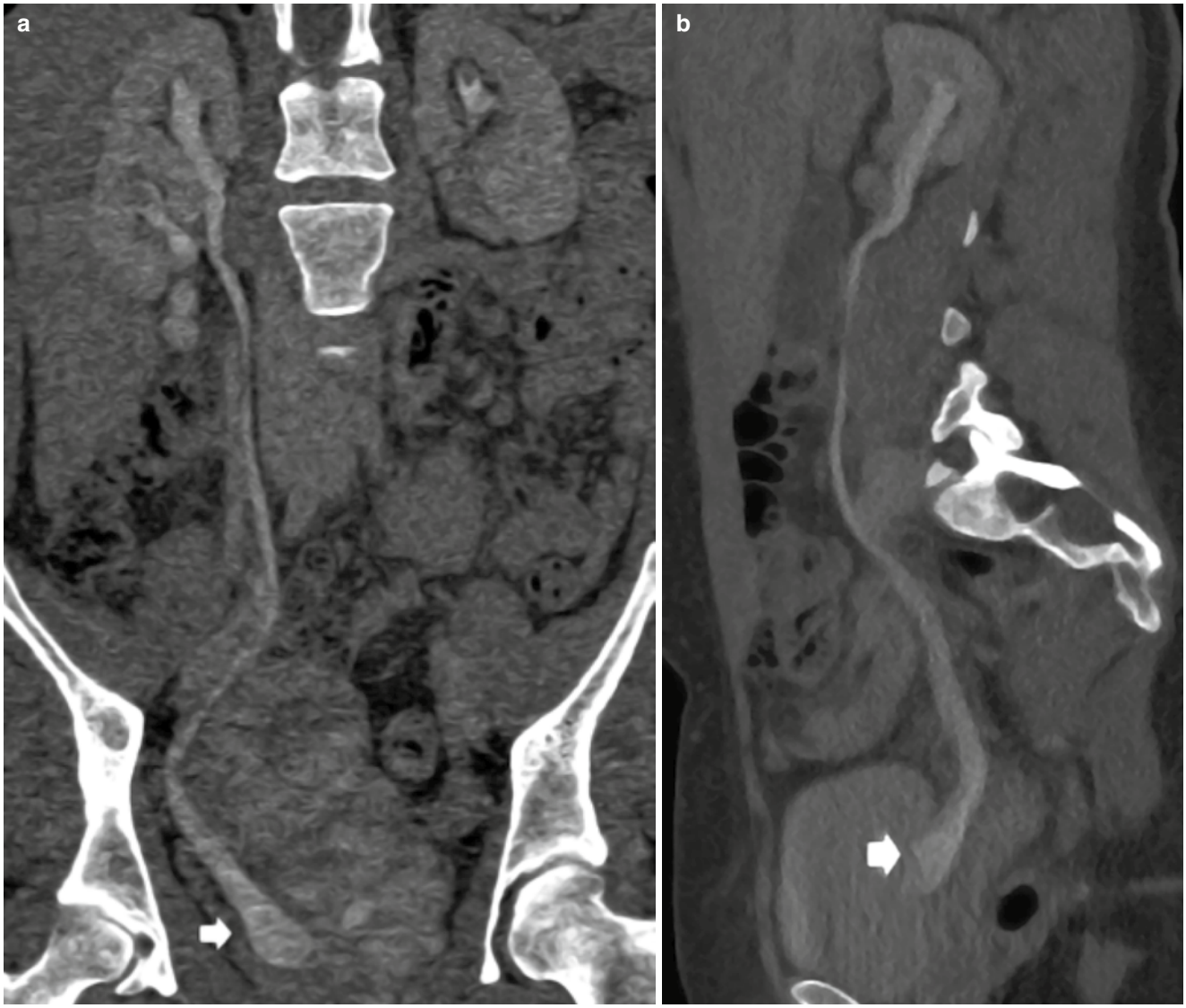

Fig. 55 (**a**, **b**) CT urography. (**a**) Coronal and (**b**) curvilinear reformation. Urinary tract duplication with ureterocele (*arrow*)

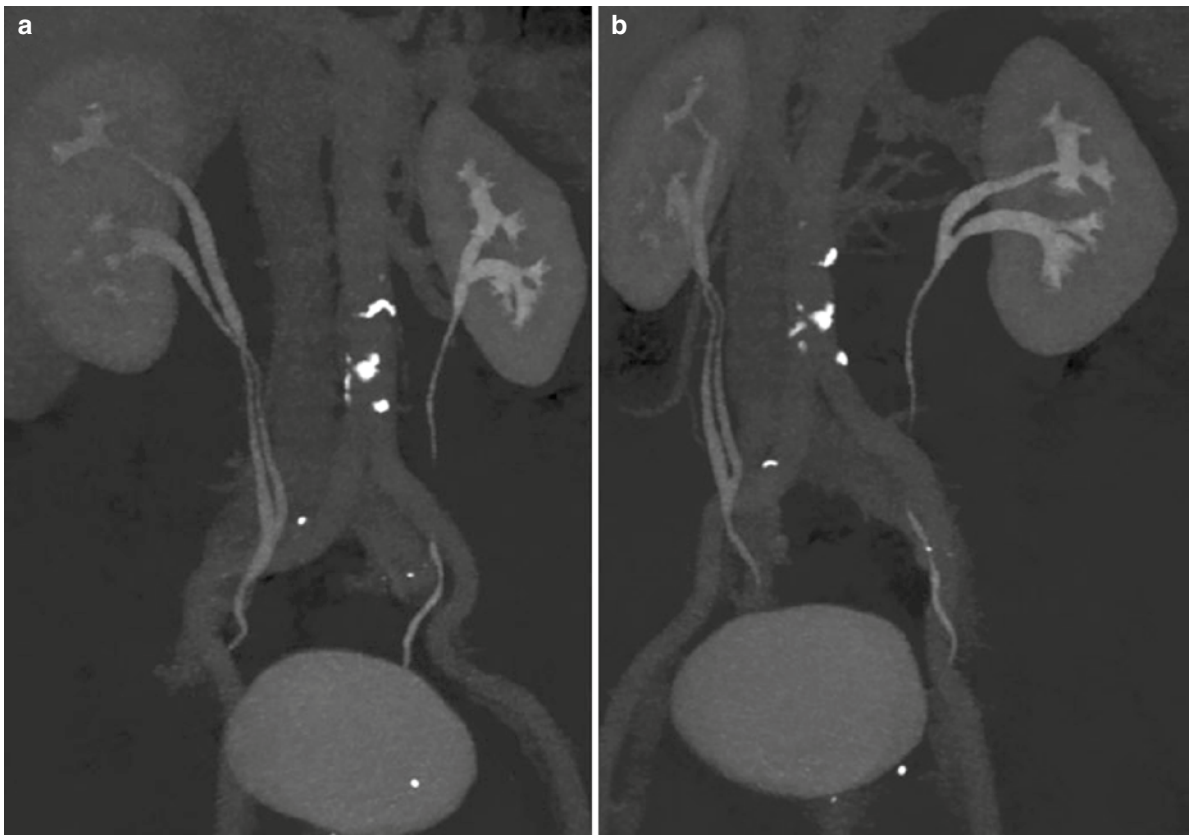

Fig. 56 (**a**, **b**) Bilateral urinary tract duplication. CTU. The duplication involved incompletely the ureter on the right side and exclusively the renal pelvis on the left side

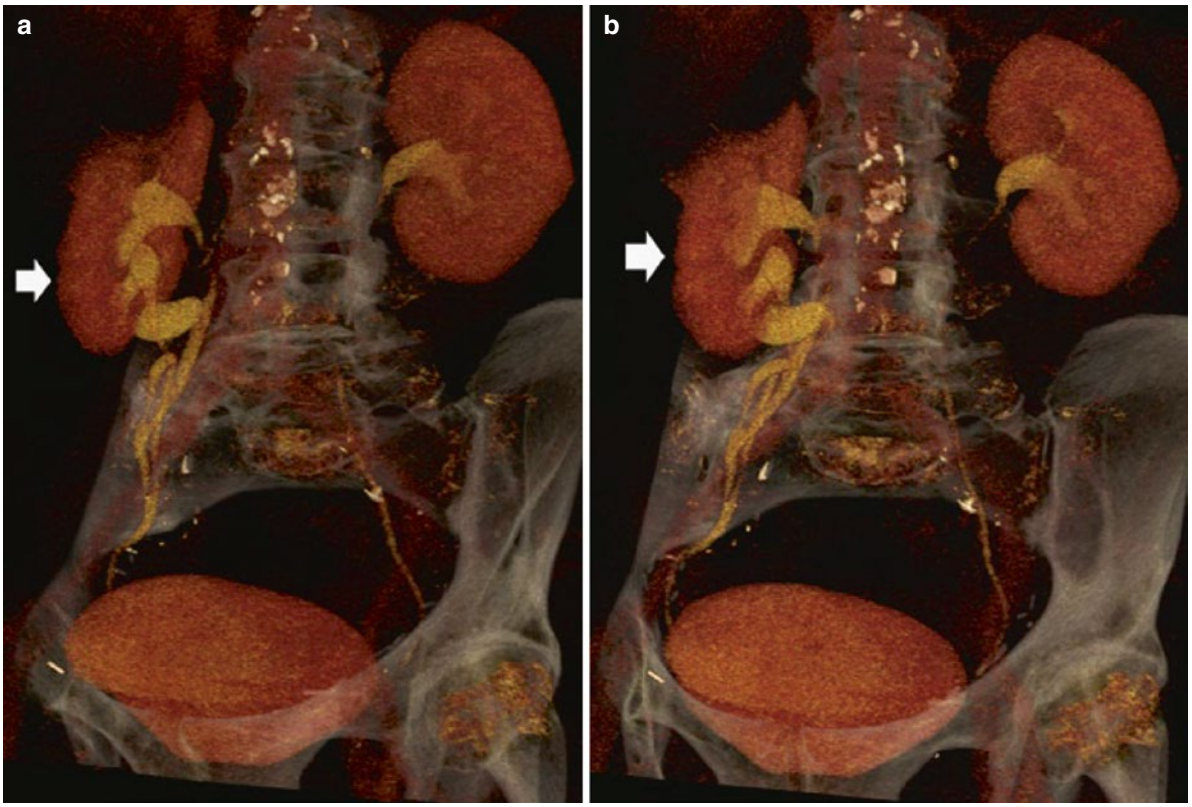

Fig. 57 (**a**, **b**) Color-coded CT urography. Triple division of the urinary tract on the right kidney (*arrow*)

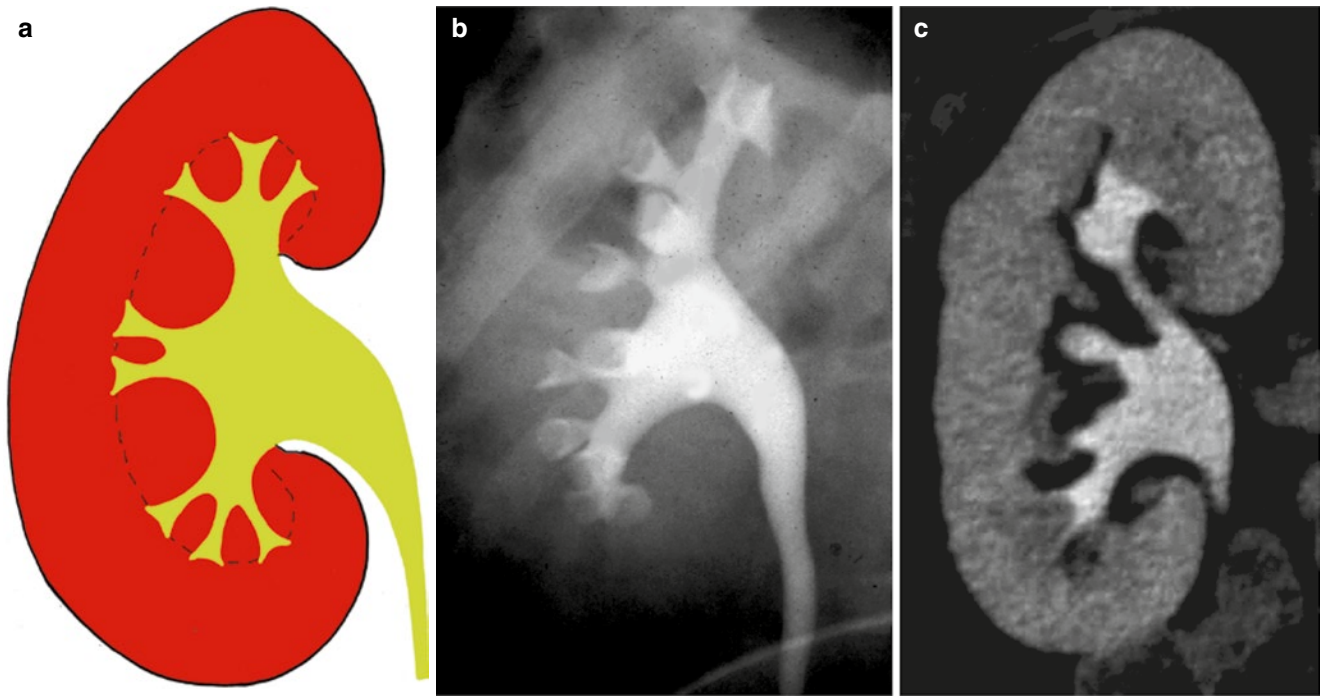

Fig. 58 (**a**–**c**) Normal intrarenal urinary tract. (**a**) Scheme with the evidence of the ideal line (Hodson's line) connecting the apex of the renal papillae; (**b**) intravenous excretory urography; (**c**) multidetector computed tomography urography (*CTU*)

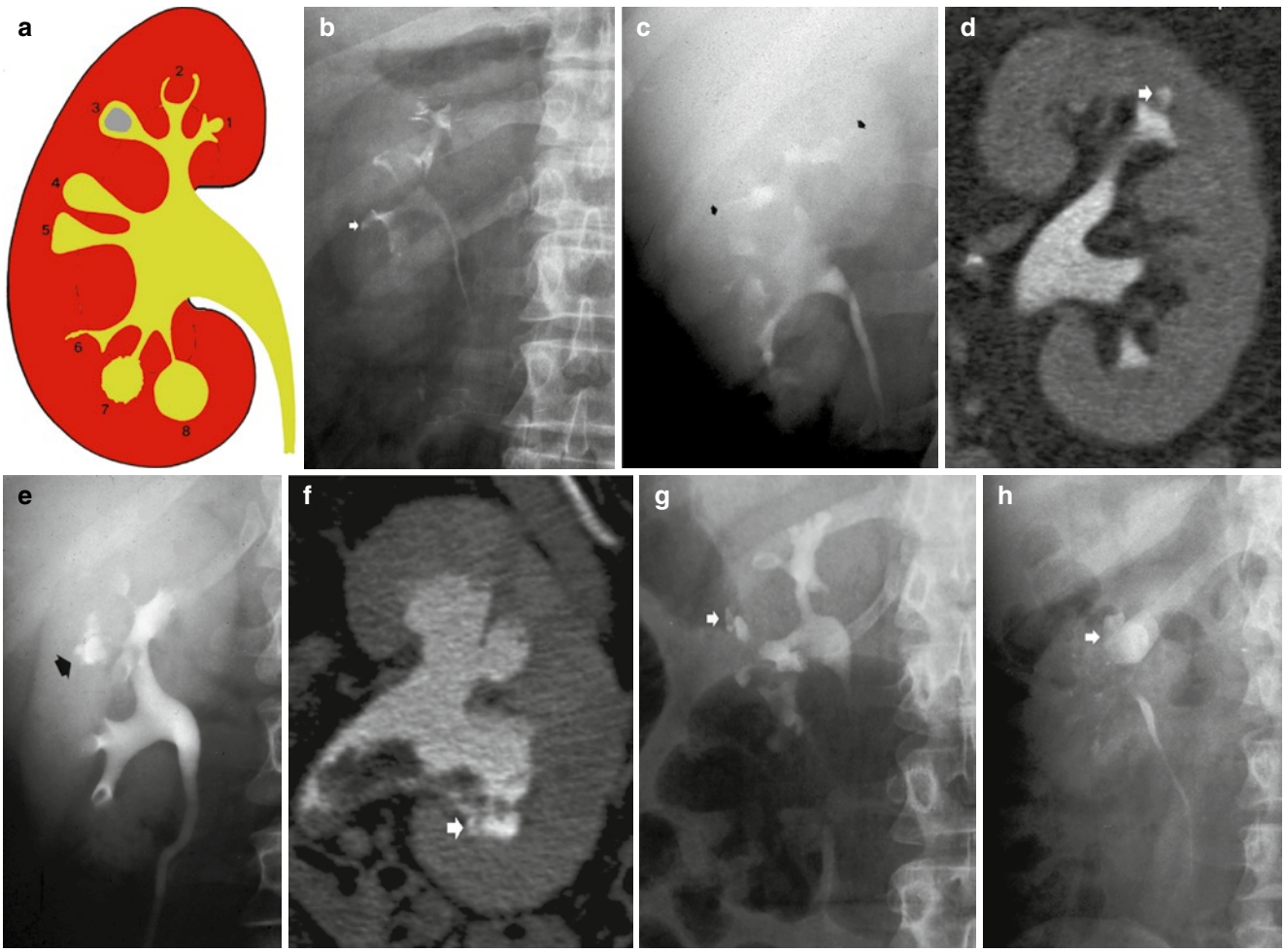

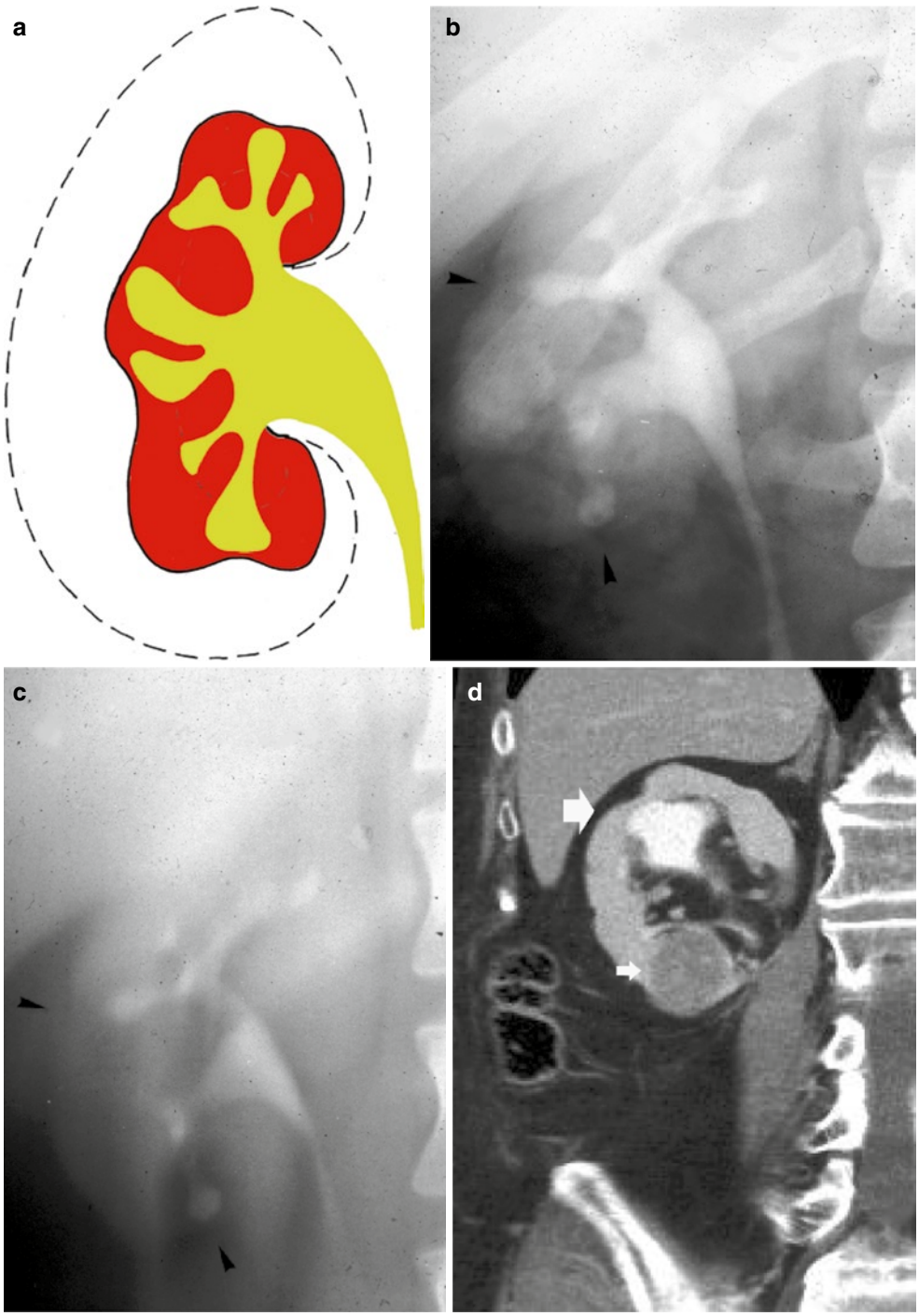

Fig. 60 (**a**–**d**) Appearances of plus images manifesting as pelvis, or calyceal deformities. (**a**) Scheme with the evidence of the ideal line representing the normal renal profile. Calyceal deformities due to reflux nephropathy with cortical loss over dilated deformed calyx with a calviform shape. (**b**, **c**) Intravenous excretory urography. Reflux nephropathy with typical calyceal deformities (*arrowheads*) and alteration of the renal profile. (**d**) CT urography. Reflux nephropathy with clubbing deformation of the renal calyces and parenchymal scarring with alteration of the renal profile (*large arrow*). A solid renal tumor (*small arrow*) is also identified on the lower renal pole

Fig. 59 (**a**–**h**) Appearances of plus images of the renal calyces manifesting as calyceal deformities or cavitations. (**a**) Scheme with the evidence of the ideal line connecting the apex of the renal papillae – Hodson's line: (*1*) renal medullary necrosis; (*2–3*) renal papillary necrosis from initial detachment of necrotic papillae to the triangular filling defect due to the sloughing of the necrotic papilla; (*4*) calyceal deformity and clubbing due to parenchymal scarring in chronic renal infection; (*5*) calyceal deformity with convexity of the calyceal profile in initial renal hydronephrosis; (*6*) calyceal ulceration; (*7*) cavitation; (*8*) hydrocalyx. (**b**) Intravenous excretory urography. Calyceal diverticulum (*arrow*) connects to the calyceal fornix and projecting into the renal cortex. (**c**, **d**) Intravenous excretory urography (**c**) and CT urography (**d**). Renal medullary necrosis at the tip of the papilla appearing as microcavities (*arrows*) surrounded by the papilla fornices. (**e**, **f**) Intravenous excretory urography (**e**) and CT urography (**f**). Renal papillary necrosis (*arrow*) with blunted calyx and preservation of the renal profile. On image (**f**) there is also evidence of hypodense blood coagula at the level of the pyeloureteral junction. (**g**) Intravenous excretory urography. Ulcerations (*arrows*) of the upper renal calyces due to renal tuberculosis. (**h**) Intravenous excretory urography. Hydrocalycosis (*arrow*) due to tubercular infundibular stenosis

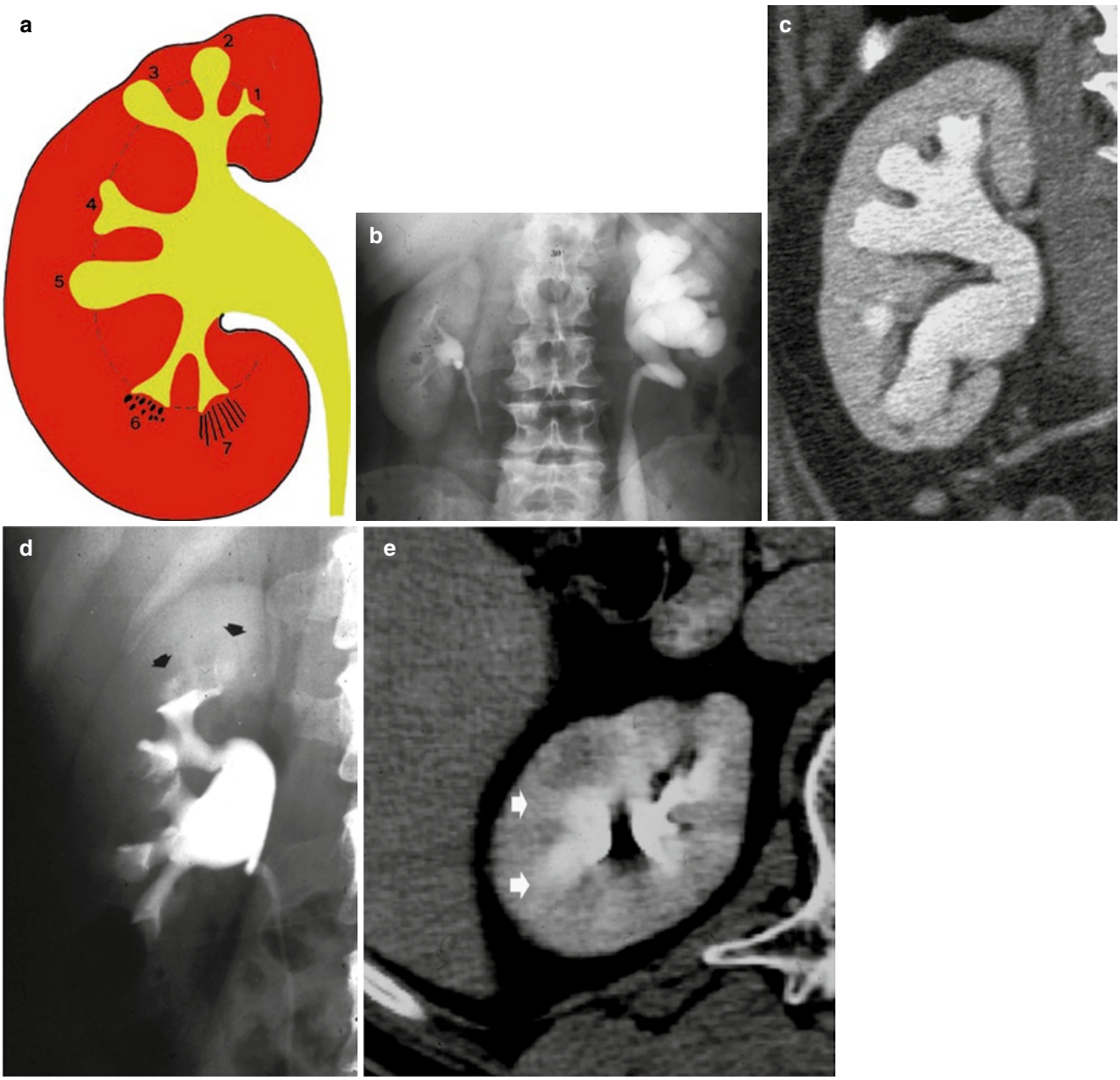

Fig. 61 (**a**–**e**) Appearances of plus images due to dilatation of the urinary tract. (**a**) Scheme with the evidence of the ideal line connecting the external renal calyx profiles: (*1*) normal calyx; (*2–3*) reflux nephropathy; (*4–5*) hydronephrosis; (*6–7*) sponge kidney with linear striations (*6*) and small round contrast collections (*7*). (**b**) Intravenous excretory urography. Hydronephrosis of the left urinary tract. (**c**) CTU. Hydronephrosis of the right urinary tract. (**d**) Intravenous excretory urography. Medullary sponge kidney with the evidence of linear striations and small round contrast collections (*arrows*). (**e**) CT urography. Medullary sponge kidney. Linear striations at the level of renal papillae (*arrows*)

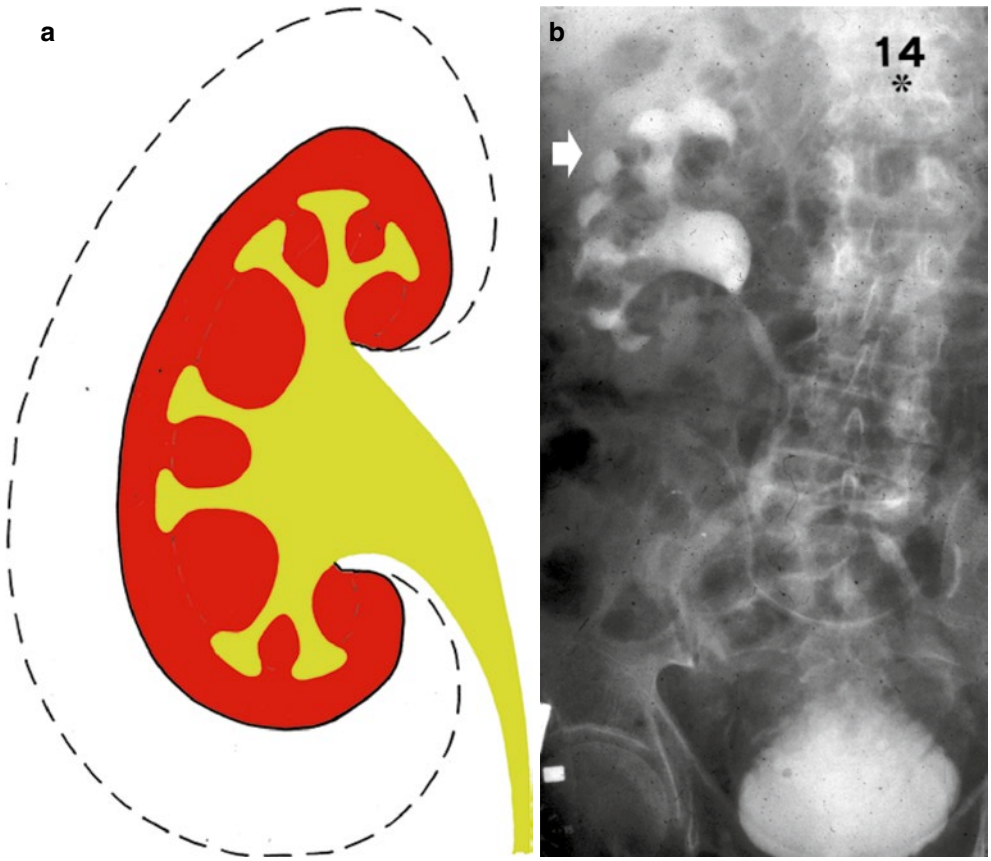

Fig. 62 (**a**, **b**) Appearances of plus images manifesting as calyceal deformities due to papillary atrophy. (**a**) Scheme with the evidence of the ideal line representing the normal renal parenchyma profile; (**b**) intravenous excretory urography. Papillary atrophy with the absence of the normal concave calyceal profile and the evidence of convex calyceal profile (*arrow*) due to benign prostatic hypertrophy

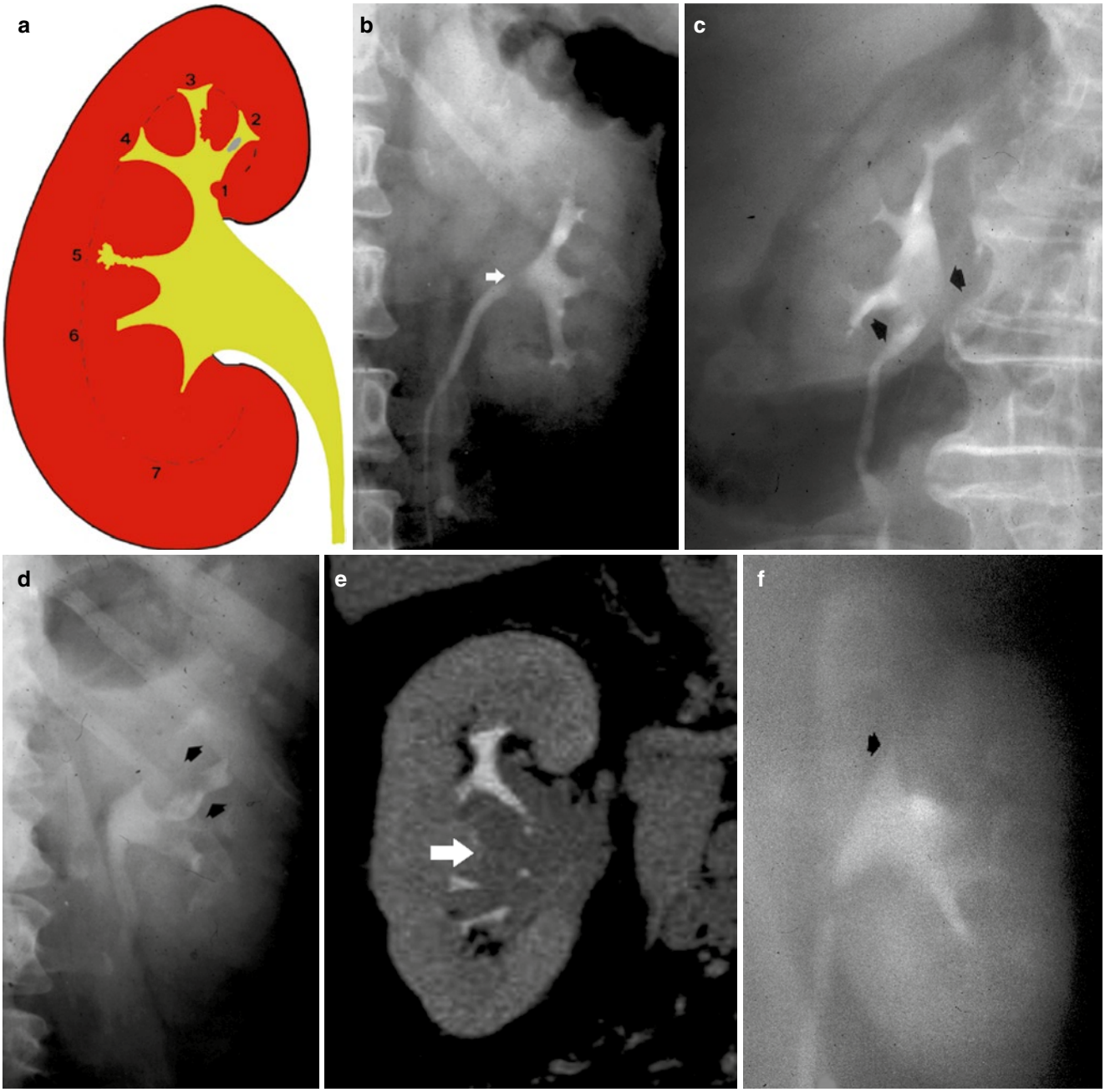

Fig. 63 (**a**–**e**) Appearances of minus images corresponding to renal pelvis or calyceal defects or amputations. (**a**) Scheme with the evidence of the ideal line connecting the external renal calyx profiles: (*1*) vascular notching; (*2*) filling defect due to a tumor, stone, or clot; (*3*) calyceal erosion due to tumor; (*4*) normal calyx; (*5*) calyceal deformity due to tumor; (*6*) calyceal amputation due to tumor; (*7*) calyceal amputation due to tuberculosis; (**b**) intravenous excretory urography. Notching at the level of the left pyeloureteral junction (*arrow*) due to a peripheral vessel. Vascular notches may determine minus images also at the level of renal calyces. (**c**, **d**) Filling defects (*arrows*) of the renal pelvis or renal calyces due to urothelial carcinoma. (**e**) Multidetector CTU. Coronal reformation. Filling defect on the renal pelvis with infundibula amputation due to renal lymphoma (*arrow*). (**f**) intravenous excretory urography–nephrotomography. Upper calyceal amputation (*arrow*) due to renal fibrosclerosing tuberculosis

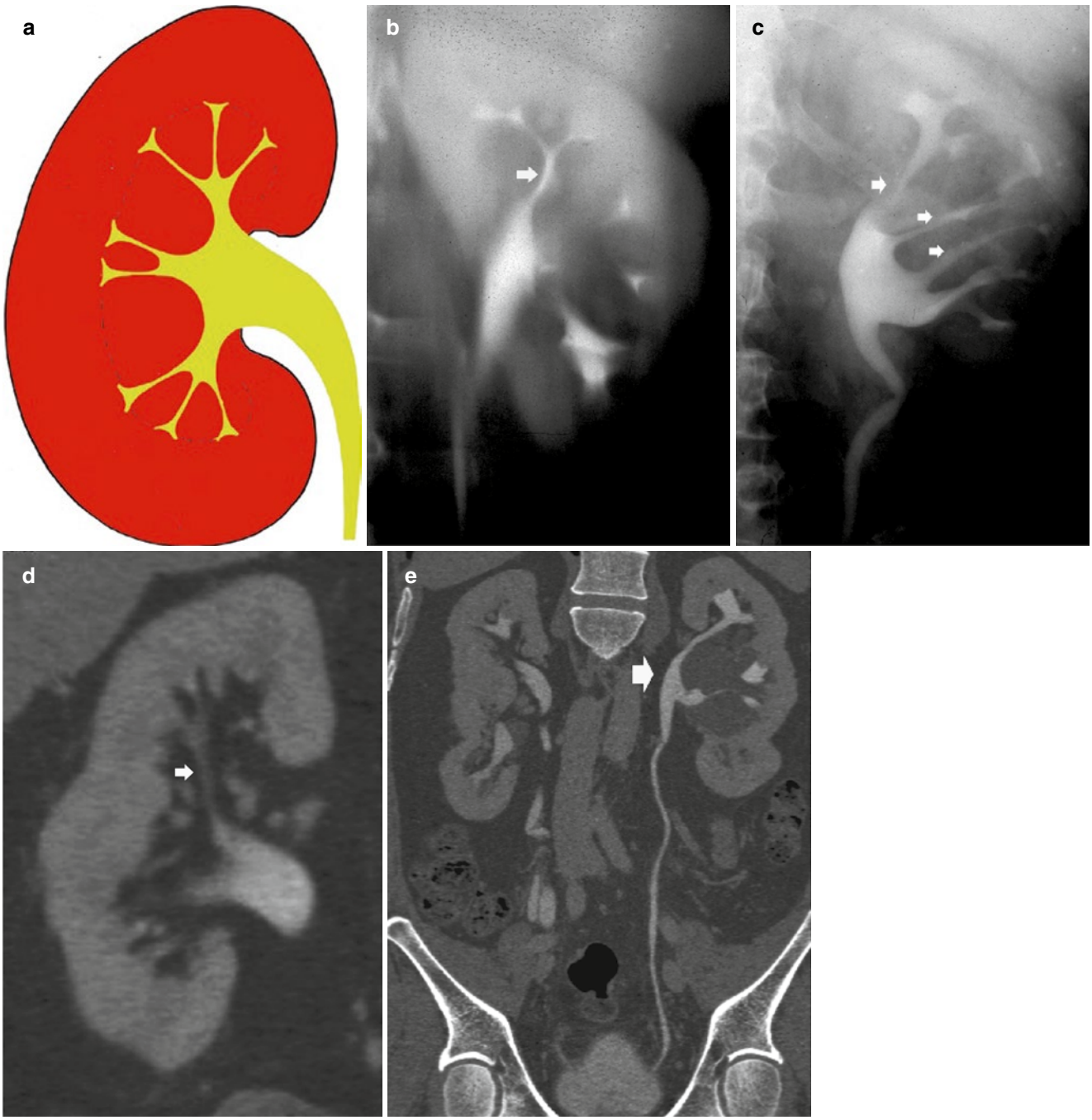

Fig. 64 (**a**, **b**) Appearances of minus images corresponding to changes of the infundibulum or calyceal profile. (**a**) Scheme with evidence of the ideal line connecting the external renal calyx profiles; (**b**, **c**) intravenous excretory urography. Urography–nephrotomography (**b**) and intravenous urography (**c**). Narrowing of the renal calyces (*arrow* in **b**, and *arrows* in **d**) due to renal sinus lipomatosis. (**d**) CT urography. Narrowing of the renal upper calyx (*arrow*) due to renal sinus lipomatosis in a 65-year-old man. Renal sinus lipomatosis may determine also minus images with the alteration of the calyx morphology with the elongation of the infundibulum profile. (**e**) CT urography. Narrowing of the renal upper and middle calyces and of the pyeloureteral junction (*arrow*) due to parapyelic cysts

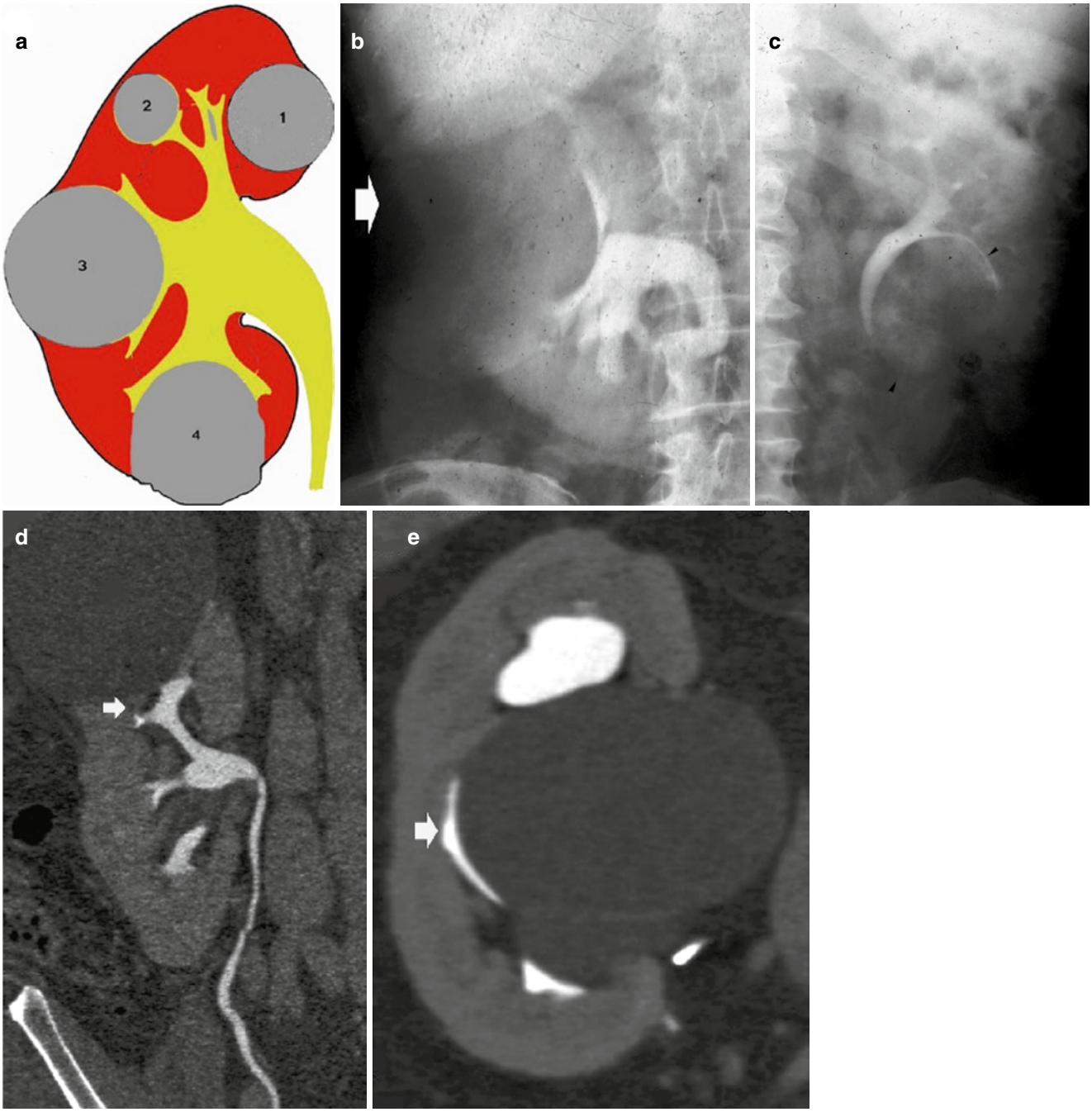

Fig. 65 (**a**) Appearances of minus images corresponding to renal pelvis or calyceal displacement due to renal cyst or solid mass of different size and location determining renal pelvis or calyceal displacement (numbered from 1 to 4). (**a**) Scheme with the evidence of the ideal line connecting the external renal calyx profiles; (**b**) intravenous excretory urography. Calyceal displacement (*arrow*) due to renal cysts; (**c**) intravenous excretory urography. Calyceal displacement (*arrowheads*) due to a solid renal mass; (**d**, **e**) multidetector CTU. Calyceal displacement (*arrow*) due to renal cysts

References

Amis ES Jr (1999) Epitaph for the urogram. Radiology 213:639–640

Andreoli TE (1992) Approach to the patient with renal disease. In: Wyngaarden JB, Smith LH, Bennett JC (eds) Cecil textbook of medicine. Saunders, Philadelphia, pp 477–482

Barakat AJ, Drougas JG (1991) Occurrence of congenital abnormalities of kidney and urinary tract in 13775 autopsies. Urology 38:347–350

Baxter JD (1992) Regulation of adrenal steroid production. In: Wyngaarden JB, Smith LH, Bennett JC (eds) Cecil textbook of medicine. Saunders, Philadelphia, pp 1275–1277

Behrman RE, Kliegman RM, Arvin AM (1996) Nelson textbook of pediatrics, 15th edn. WB Saunders, Philadelphia

Bude RO, Rubin JM (1995) Detection of renal artery stenosis with Doppler sonography: it is more complicated than originally thought (editorial). Radiology 196:612–613

Bude RO, Rubin JM, Adler RS (1994) Power versus conventional color Doppler sonography: comparison in the depiction of normal intrarenal vasculature. Radiology 192(3):777–780

Buschi AJ, Harrison RB, Norman A et al (1980) Distended left renal vein: CT/sonographic normal variant. AJR Am J Roentgenol 135:339–342

Chiara A, Chirico G, Comelli L et al (1990) Increased renal echogenicity in the neonate. Early Hum Dev 22:29–37

Cockcroft DW, Gault MH (1976) Prediction of creatinine clearance from serum creatinine. Nephron 16(1):31–41

Cohen AJ (1991) Use of diuretics in the intensive care units. In: Rippe JM, Irwin RS et al (eds) Intensive care medicine. Little, Brown and Company, Boston, pp 733–742

Correas JM, Helenon O, Moreau JF (1999) Contrast enhanced ultrasonography of native and transplant kidney diseases. Eur Radiol 9(suppl 3):394–400

Cuttino JT Jr, Clark RL, Jennette JC (1989) Microradiographic demonstration of human intrarenal microlymphatic pathways. Urol Radiol 11:83–87

Dagher PR, Herget-Rosenthal S, Ruehm SG et al (2003) Newly developed techniques to study and diagnose acute renal failure. J Am Soc Nephrol 14:2188–2198

Davidson C, Stacul F, McCullough PA et al (2006) Contrast medium use. Am J Cardiol 98(suppl):42K–58K

Desberg AL, Paushter DM, Lammert GK et al (1990) Renal artery stenosis: evaluation with color Doppler flow imaging. Radiology 177:749–753

Fanney DR, Casillas J, Murphy BJ (1990) CT in the diagnosis of renal trauma. Radiographics 10:29–40

Federle MP, Guliani-Chabra S, Venkata SA (2004) Renal ectopia. In: Federle MP (ed) Diagnostic imaging abdomen. Amirys, Salt Lake City, pp 6–7

Federle MP et al (2006) Embryology of the abdomen. In: Federle MP, Rosado-de-Christenson ML, Woodward PJ (eds) Diagnostic and surgical imaging anatomy. Chest, abdomen, pelvis. Amirsys, Altona, pp 446–483

Friedenberg RM, Dunbar JS (1990) Excretory urography. In: Pollack HM (ed) Clinical urography. Saunders, Philadelphia, pp 101–243

Gourtsoyiannis N, Prassopoulos P, Cavouras D, Pantelidis N (1990) The thickness of the renal parenchyma decreases with age: a CT study of 360 patients. AJR Am J Roentgenol 155:541–544

Grant EG, Melany ML (2001) Ultrasound contrast agents in the evaluation of the renal arteries. In: Goldberg BB, Raichlen JS, Forsberg F (eds) Ultrasound contrast agents. Basic principles and clinical applications, 2nd edn. Martin Dunitz, London, pp 289–295

Grist TM (2000) MRA of the abdominal aorta and lower extremities. J Magn Reson Imaging 11:32–43

Helenon O, Rody EL, Correas JM et al (1995) Color Doppler US of renovascular disease in native kidneys. Radiographics 15:833–854

Hogg CM, Reid O, Scothorne RJ (1982) Studies on hemolymph nodes. III. Renal lymph as a major source of erythrocytes in the renal hemolymph node of the rat. J Anat 135:291–299

Hricak H, Slovis TL, Callen CW et al (1983) Neonatal kidneys: sonographic anatomic correlation. Radiology 147:699

Ischikawa Y, Akasaka Y, Kiguchi H et al (2006) The human renal lymphatics under normal and pathological conditions. Histopathology 49(3):265–273

Joffe SA, Servaes S, Okon S et al (2003) Multi-detector row CT urography in the evaluation of hematuria. Radiographics 23: 1441–1455

Karazincir S, Balci A, Gorur S et al (2007) Incidence of the retroaortic left renal vein in patients with varicocele. J Ultrasound Med 26:601–604

Kasap B, Soylu A, Türkmen M et al (2006) Relationship of increased renal cortical echogenicity with clinical and laboratory findings in pediatric renal disease. J Clin Ultrasound 34:339–342

Klahr S (1992) Structure and function of the kidneys. In: Wyngaarden JB, Smith LH, Bennett JC (eds) Cecil textbook of medicine. Saunders, Philadelphia, pp 482–492

Laiken ND, Fanestil DD (1985) Anatomy of the kidneys. In: West JB (ed) Best and Taylor's physiology basis of medical practice. Williams & Wilkins, Baltimore, pp 451–460

Lameire N, Adam A, Becker CR et al (2006) Baseline renal function screening. Am J Cardiol 98(suppl):21K–26K

Lane BR, Poggio ED, Herts BR et al (2009) Renal function assessment in the era of chronic kidney disease: renewed emphasis on renal function centered patient care. J Urol 182(2):435–443

Levey AS, Bosch JP, Lewis JB et al (1999) A more accurate method to estimate glomerular filtration rate from serum creatinine: a new prediction equation. Modification of diet in Renal Disease Study Group. Ann Intern Med 130(6):461–470

Levey AS, Stevens LA, Schmid CH et al (2009) A new equation to estimate glomerular filtration rate. Ann Intern Med 150(9): 604–612

Mahony BS, Filly RA, Callen PW, Hricak H, Golbus MS, Harrison MR (1984) Fetal renal dysplasia: sonographic evaluation. Radiology; 152(1):143–146

National Kidney Foundation (2002) K/DOQI clinical practice guidelines for chronic kidney disease: evaluation, classification, and stratification. Am J Kidney Dis 39(suppl 1):S1–S266

Nino-Murcia M, de Vries PA, Friedland GW (2000) Congenital anomalies of the kidney. In: Pollack HM, Mc Clennan BL (eds) Clinical urography. Saunders, Philadelphia, pp 690–763

Olbricht C, Mason J, Takabatake T et al (1977) The early phase of experimental acute renal failure II. Tubular leakage and the reliability of glomerular markers. Pflugers Arch 372:251–258

Peipert JF, Donnenfeld AE (1991) Oligohydramnios: a review. Obstet Gynecol Surv 46(6):325–339

Reed MD, Friedman AC, Nealey P (1982) Anomalies of the left renal vein: analysis of 433 CT scans. J Comput Assist Tomogr 6: 1124–1126

Rule AD, Larson TS, Bergstralh EJ et al (2004) Using serum creatinine to estimate glomerular filtration rate: accuracy in good health and in chronic kidney disease. Ann Intern Med 141:929–937

Satyapal KS, Haffejee AA, Singh B et al (2001) Additional renal arteries: incidence and morphometry. Surg Radiol Anat 23(1):33–38

Schedl A (2007) Renal abnormalities and their developmental origin. Nat Rev Genet 8(10):791–802

Schwartz GJ, Feld LG, Langford DJ (1984) A simple estimate of glomerular filtration rate in full-term infants during the first year of life. J Pediatr 104(6):849–854

Silverman SG, Leyendecker JR, Amis SE (2009) What is the current role of CT urography and MR urography in the evaluation of the urinary tract. Radiology 250:309–323

Stevens LA, Levey AS (2005) Chronic kidney disease in the elderly – how to assess risk. N Engl J Med 352:2122–2124

Stevens LA, Coresh J, Greene T et al (2006) Assessing kidney function – measured and estimated glomerular filtration rate. N Engl J Med 354:2473–2483

Türkvatan A, Özdemir M, Cumhur T et al (2009) Multidetector CT angiography of renal vasculature: normal anatomy and variants. Eur Radiol 19(1):236–244. doi:10.1007/s00330-008-1126-3

Twining P (1994) Genitourinary malformations. In: Nyberg AD, McGahan JP, Pretorius DH, Pilu G (eds) Diagnostic imaging of fetal anomalies. Lippincott Williams and Wilkins, Philadelphia, pp 603–659

Van Der Molen AJ, Cowan NJ, Mueller-Lisse UG etal (2008) CT urography: definition, indications and techniques. A guideline for clinical practice. Eur Radiol 18:4–17

Yeh HS, Halton KP, Shapiro RS et al (1992) Junctional parenchyma: revised definition of the hypertrophic column of Bertin. Radiology 185:725–732

Yeh BM, Coakley FV, Meng MV et al (2004) Precaval right renal arteries: prevalence and morphologic associations at spiral CT. Radiology 230:429–433